POLITECNICO DI TORINO, VON KARMAN INSTITUTE FOR FLUID DYNAMICS

Master's Degree in Aerospace Engineering

Master's Degree Thesis / Project Review

Determination of the Inertia of a High-Speed Low-Pressure Turbine Rotor Assembly

Supervisor:
Professor: Roberto Marsilio

VKI Supervisors:
Professor: Sergio Lavagnoli
PhD Candidate: Lorenzo Da Valle
Research Engineer: Filippo Merli

Candidate:
Angelo Graziani s301875

A.Y. 2024/2025

Abstract

This master's degree thesis is the project's report of the internship completed by the candidate at the Von Karman Institute for Fluid Dynamics in Rhode-Saint-Genèse, Belgium, between May 2024 and November 2024.
During the internship a prototype of a high-speed, low-pressure turbine stage for a geared turbofan engine was mounted on the CT3 facility; this stage, designed by Safran Aircraft Engines, had previously been tested on the same facility of the Von Karman Institute (VKI) within the Clean Sky 2 project SPLEEN [14].

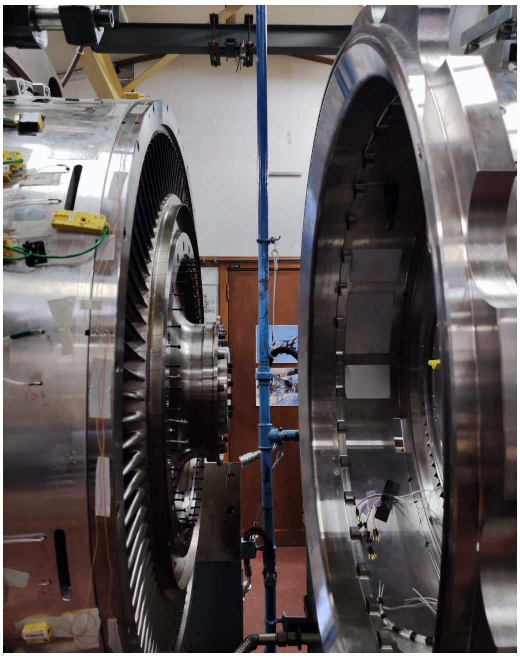

Figure 1: Image of the rotor (on the left) mounted on the "CT3" facility at the beginning of the internship.

The primary objective of this project is to accurately determine the rotor's actual inertia to validate the results of the SPLEEN project, aiming for a result that closely matches the value obtained from the CAD model, as well as aiming to a target uncertainty on every measurements around or less than 0.5%.
Achieving such precision is critical, as the inertia value plays a key role in assessing the turbine stage's efficiency η: an error on 1% on the inertia evaluation propagates as an error of 1% on the efficiency value.

The candidate has to develop a stable experimental setup for the encoder connection to the disk of the rotor[1] as well as the rotor-mass connection: this is obtained by connecting a mass falling from the ceiling to a steel wire connected to the rotor.
In parallel of the experimental setup design, then selection, purchasing and manufacturing of all of the necessary components the candidate has to create a coding routine in order to post-process the experimental data gathered from the tests.
The candidate has to run several tests with slightly different setups[2] in order to obtain an accurate estimation of the rotor's inertia and its uncertainty in different conditions.

[1]Looking at the figure [1] : on the left it is shown the rotor, on the right there is the statoric case as well as the stator itself inside of it. The encoder needs to be connected to the center part of the rotor using a stable structure fixated on the statoric case; the encoder and the rotor will share the same axis in order to detect the angular displacement during each test.

[2]For example the mass can be increased, in order to work with a different angular velocity range can be selected during the post processing routine.

Acknowledgments

Thanks to my thesis supervisor Roberto Marsilio at Politecnico di Torino, who guided and followed me in every step of this final project's journey for an entire year.
I want to thank my project supervisors at the Von Karman Institute, Lorenzo Da Valle, Sergio Lavagnoli and Filippo Merli for the guidance and continuous feedback during my whole internship in Belgium, thanks to their knowledge and advice I learnt much more than I could ever imagine before the beginning of this experience.
A special acknowledgment to my parents Loredana and Giuliano for the undivided love and support they always gave me for all these years, I owe them everything for the man I am today, I love you.
Another acknowledgment coming directly from my heart to Tatiana, for always being there for me and believing in me, especially during the darkest and hardest times. It meant everything to me.
Thanks to my grandparents, Olga, Guido, and Ida for setting an example for me and sharing with me their invaluable experiences and, most importantly, teaching me the truly important values in life.
Thanks to my friends Matteo C., Matteo M., Luca, Mario, Lorenzo M., Francesco, Lorenzo C., Lorenzo A. for sharing moments with them I will never forget.
Thanks to my university friends, Gianmarco, Giulia, Paolo, Giovanni for the support and hilarious moments shared in and out of the classes.
Thanks to all the people I met at the Von Karman Institute from all the parts of Europe, they made even the most difficult weeks at work less stressful: a special acknowledgment to my colleagues in the office Giuseppe C., Giuseppe B., Samuele, Giacomo, Brian, Tom, Francesco L., Francesco P., Annamaria, Thomas, Ewann, Luise and to Alessio, Fernando, Louis for all the madness experienced in the Turbomachinery's laboratory.

Last but not least, thanks to the 16 years old me for making the most difficult choice of his life: to chase his dream instead of staying in the comfort zone, and then obsessively working towards it against all the odds. Without that first step I don't know where I would be at this exact moment.

Contents

List of Figures

List of Tables

Chapter 1

Literature Review and General Overview of the "CT3" Facility

This chapter provides an overview of previous experiments related to the project's topics and presents the main theoretical reference papers; it includes detailed discussions of the relevant physical and mathematical methods used in the new 2024 campaign.
Also a brief overview of the "CT3 facility" has been added to this chapter, providing more context about the equipment the candidate had to work with during the internship.

1.1 Introduction to the Yasa's mechanical method for the rotor inertia's accurate measurements

For an accurate calculation of the power of a rotating component, it is necessary to calculate its inertia; in this case, the efficiency of the turbine stage must be calculated by evaluating the inertia using an experimental methodology.
The mechanical torque of the turbine is measured by calculating the angular acceleration; torque is calculated as:

$$\tau = I\alpha[Nm = (kgm^2)(\frac{rad}{s^2})]$$

Where I represents the moment of inertia and α the angular acceleration of the rotor.
The moment of inertia describes a rotating mechanical device's resistance to change its rotation.
To determine the inertia value there are four main methodologies in use (for complex rotating assembles):

1. Pendolum Techniques (bi-filar, tri-filer, multicable)
2. Simplified Torsion Mechanism
3. Vibration test Facilities
4. **Forced Acceleration followed by Free Deceleration**: this setup has a mass attached to the rotor rim by a wire collected around a specific cylinder. It is the option chosen for the current project.

The percentage error in calculating inertia propagates proportionally to the final calculation of the turbine's efficiency, this is why this evaluation plays an important role.
There are two ways to experimentally measure the inertia of a rotor as cited in the article [8], published in 2007 by the authors G. Paniagua and T. Yasa: this is one of the two main sources of information for this project as the experimental setup and methodologies published are the basics for the candidate's project design and post processing method.

1. *Trifiler Suspension Technique*
   Accuracy of [1 - 2%] but the practical realization is extremely complex because the rotor should disassembled (it would be an issue for the lubrification system).
2. *Inertia's measurement with known constant torque and angular acceleration evaluation*

$$\tau = I\alpha + \tau_F$$

   Included in the calculation are the effects of rotor's bearing friction, which are not negligible at low rotational speeds (in this case $\omega_{max} \approx 3\frac{rad}{s}$).

The tests were carried out in the 'VKI Compression Tube CT3' in 2006, a facility where the Mach and Reynolds can be manipulated independently; the turbine rotor simulates approximately the design speed of the real case ($6500rpm \approx 680.8\frac{rad}{s}$) for a short period of time, approximately 0.4 seconds.
A piston simulates an almost isoentropic compression, after opening a valve the pressurized and hot flow enters the turbine; a variable section throat controls the sonic conditions and moves a rotor that converts almost all the power into acceleration.
The rotor comprises the blades, the shaft with the electronics, the inertia disk (*inertia wheel*) and the data transmission shaft as well as the turbine starter.
For this project the inertia's measurements were conducted with the "CT3" facility opened, so without using the compression tube and by only working on the rotor; more information about the facility and more context is provided in section [1.3].

Friction Losses Measurement

There are three factors to be considered when studying the friction losses:

1. **Bearings losses**. These are the most significant losses and can be modelled with an exponential law:
$$\tau_{F_{bearings}} = \rho C_{bearings} \omega^{n_{bearings}} \tag{1.1}$$
2. Resistance losses (**Windage losses**) Losses due to flow resistance on the rotor disc, follow an exponential law as a function of angular velocity and are density dependent:
$$\tau_{F_{windage}} = \rho C_{windage} \omega^{n_{windage}} \tag{1.2}$$
   These losses at low speeds are also negligible (order of $\approx 10^-5$)
3. **Ventilation losses** These are losses due to flow deviation in the vicinity of the rotor blades, mainly due to viscous forces. At low speeds this effect is negligible.

To have comparable data over several tests, the speed ranges of the tests must be the same; in the already cited paper [8] the coefficient of friction is considered as a constant and it is defined as the friction torque divided by the product of the mass supported by the bearings and the radius of the bearings:
$$\mu(\omega) = \frac{\tau_{F_{bearings}}(\omega)}{mR_{bearings}} \tag{1.3}$$
By doing the integral between the friction torque and the angular position, the energy dissipated by friction is calculated following this law:
$$\Delta E_F = \int_1^2 \tau_f \cdot d\theta \approx \tau_F \Delta\theta \tag{1.4}$$
Where $\Delta\theta$ is the total angular displacement detected during the test.

First Method: Free Deceleration Test

The friction torque (friction losses) is calculated by applying an impulse to the rotor and the deceleration due to friction of the entire system connected to the rotor is measured.
Two tests are performed;

- No calibrated disk

$$0 = I_{rotor}\alpha + \tau_F$$

- Calibrated steel disk $m_{disk} = 47.6[kg]$ and it's inertia is $I_{disk} \approx 2[kgm^2]$

$$0 = (I_{rotore} + I_{disk})\alpha_{disk} + \tau_{F_{disk}}$$

$$I_{rotore} = I_{disk}\frac{\alpha_{disk}}{(\alpha - \alpha_{disk})}$$

The test measured the angular velocity by using an encoder with a resolution of 1024 pulses per revolution, then sampled at 80 MHz to reduce the noise coming from the raw measurements. The angular velocity was measured ensuring the same speed ranges with the same friction coefficient μ where taken for every testing session: without the inertia disk, the angular position trend was described by this parabolic trend:

$$\theta(t) = b_2t^2 + b_1t + b_0$$

with an angular acceleration $\alpha = 2b_2$.
With the calibrated disk the formula changed in

$$\theta_{disk}(t) = b_{2_{disk}}t^2 + b_{1_{disk}}t + b_{0_{disk}}$$

The resulting value of inertia turns out to be $I = 27[kgm^2]$ but this is not correct as the friction torque should not be considered constant but variable during the test: if the disk is added the friction coefficient varies and this is one of the reasons why five years, in 2012, later from the publishing of this paper a new methodology was presented in the paper [9] where friction was considered varying linearly with angular velocity; for this reference the method will be reported in detail in section [1.2]. With the addition of the disk, the inertia increases by 12 % but this method is highly inaccurate, a far better accuracy can be achieved with the second method shown in the following section.

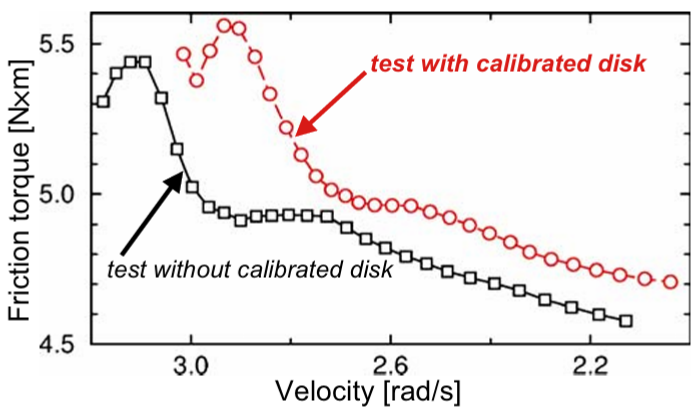

Figure 1.1: Friction Torque considering the presence or absence of a calibrated disk in the free deceleration test.

Acceleration-Deceleration Test

The second method consists of accelerating and decelerating the rotor knowing the torque: the rotor is connected with a mass hanging and free to move by means of a wire and a pulley connection; this was the method also recreated with the new experimantal setup design by the candidate.
In the study conducted in 2006 [8], a ‘digital encoder’ is used to measure angular position (1024 pulses per revolution) and than sampled at 80 MHz to reduce the "noise" of the raw data measurements as shown in the figure [1.2]

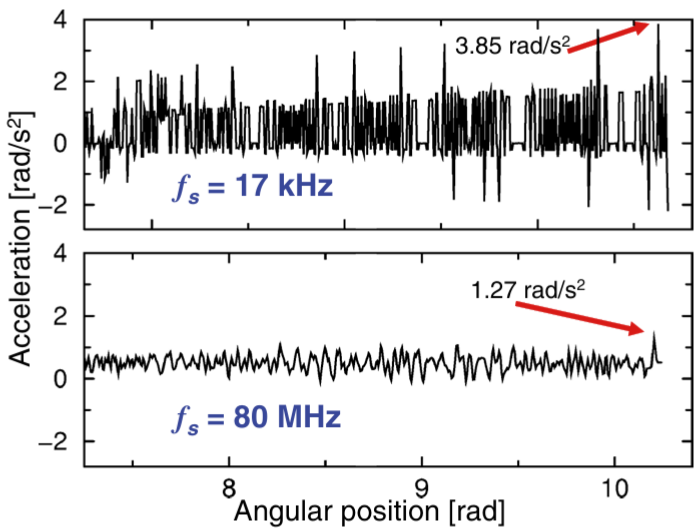

Figure 1.2: Angular velocity fluctuations, data taken at 17kHz or 80 MHz, with the second option resulting in more accurate and clean data.

The wire connected to the mass is initially wound around a cylinder integrated with the rotor, when the mass is released the rotor is accelerated by gravity acting on the mass and the test is now divided in two phases:

1. **Acceleration Phase**
   From time t_a to time t_b the falling mass accelerates the rotor; in this phase the variation of the angular position follows an almost perfectly parabolic law.
   The variation of potential energy is equal to the variation of kinetic energy and friction losses, which than results in the following equation:

$$\Delta E_p = \Delta E_k + \Delta E_f$$

$$mRg(\theta_b - \theta_a) = (I_{disk} + I_{rotor} + mR^2 + I_p \frac{R^2}{r^2}) \frac{(\omega_b^2 - \omega_a^2)}{2} + \tau_F(\theta_b - \theta_a) \quad (1.5)$$

   where I_p is the inertia of the pulley, R is the radius of the rotor around which the wire is tied, r is the radius of the pulley.

2. **Deceleration Phase**
   From time t_c to time t_d the mass ceases to be accelerated and the deceleration phase due to the friction exerted by the bearings begins; the equation used to describe this phase is still the conservation of energy:

$$0 = \Delta E_k + \Delta E_f \quad (1.6)$$

$$0 = (I_{disk} + I_{rotor})\frac{(\omega_c^2 - \omega_d^2)}{2} + \tau_F(\theta_c - \theta_d) \tag{1.7}$$

by selecting equal speed ranges for both phases, the inertia torque should be similar after the experiments.

By putting in the same system both of the equations used for the acceleration and the deceleration phases, the inertia of the rotor can be calculated with the following equation, we will later refer to this formulation as "Yasa method equation".

$$I_{rotor} = \frac{mR(2g - (R + I_p\frac{R}{mr^2})(\frac{\omega_b^2-\omega_a^2}{\theta_b-\theta_a})}{(\frac{\omega_b^2-\omega_a^2}{\theta_b-\theta_a}) - (\frac{\omega_d^2-\omega_c^2}{\theta_d-\theta_c})} \tag{1.8}$$

By simplifying the angular velocity model with the centred finite difference method (up to fourth order), the simplified angular velocity was derived, thereby reducing the fluctuations present in the 17 kHz measurements by a factor of 3 with more accurate representations at 80 MHz as shown in figure [1.2] This also simplifies the rotor inertia equation by making the following observations and simplifications:

- Quadratic trend of angular position variation

$$\begin{cases} \theta_{acceleration(t)} = a_2t^2 + a_1t + a_0 \\ \theta_{deleration(t)} = b_2t^2 + b_1t + b_0 \end{cases} \tag{1.9}$$

- The equation is further simplified as a function of acceleration ($2a_2$ e $2b_2$)):

$$\begin{cases} (\frac{\omega_b^2-\omega_a^2}{\theta_b-\theta_a}) = 4a_2 \\ (\frac{\omega_d^2-\omega_c^2}{\theta_d-\theta_c}) = 4b_2 \end{cases} \tag{1.10}$$

This results in the final equation for calculating the rotor's inertia:

$$I_{rotor} = \frac{mR(g - 2a_2R - \frac{2I_pRa_2}{mr^2})}{2(a_2 - b_2)} \tag{1.11}$$

Once the inertia is calculated, the friction loss is estimated (assuming the same constant friction torque is applied to both the acceleration and deceleration phases)

Results and Analysis

First you want to consider angles such that the speed ranges are the same for both phases (acceleration and deceleration).

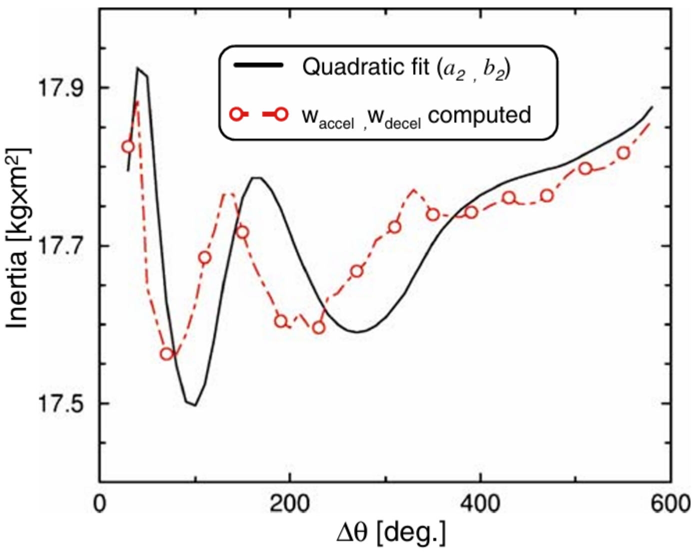

Figure 1.3: Trend of inertia during the acceleration phase as the angular position changes: according to the data, the trend is almost quadratic.

by changing the masses (and thus the accelerations), for higher values, greater accuracy is noted in the application of this methodology.
The results after 10 tests both with and without the calbrated disk show the following results:

		$\bar{x}$	$\sigma(\%)$	$\Delta x/x(\%)$
no DISK (10 tests)	a_2	0.253	0.516	0.369
	b_2	−0.138	0.418	0.299
	I_{rotor}	17.739	0.255	0.182
with DISK (11 tests)	a_2	0.223	0.230	0.155
	b_2	−0.126	0.188	0.126
	I_{rotor}	17.598	0.144	0.097

Figure 1.4: Main results using the 5 kg mass and angles limited to variations of 360^0 (accelerations and moment of inertia of the rotor, as well as percentage results on the accuracy of the method).
By using the inertia's disk a higher accuracy is obtained.

The final result after the uncertainty analysis is:

$$I_{rotor} = 17.671 \pm 0.27\%[kgm^2] \approx 18.12[kgm^2] \tag{1.12}$$

Conclusions

Accuracy in the measurement of inertia is necessary to minimize systematic errors in power calculations of rotating organs; the aim of this experiment was to verify greater accuracy using the methodology of a free-falling mass (thus moving the rotor) than the 'torsional pendulum', and indeed this is the case.
With this method, it is possible to accurately calculate friction losses at low rotational speeds.

1.2 Variable Friction Method for Acceleration-Deceleration Test

The article [9], written by the authors Thomas Povey and Guillermo Paniagua and published in 2012, shows another method to determine rotating organs inertia with superior measurement precision, focus is on accurate evaluations of friction and inertia to have a more precise result. The experiment and data used is the same treated in the article [8] written by Tolga Yasa and Guillermo Paniagua; it is the same study of the rotor accelerated by an external mass in the acceleration phase, then detached and the free spinning down rotor deceleration phase but with the new hypothesis of variable friction considered.
This model studies frictional torque τ_F as a linear function depending from speed and provides a new numerical solution, differing from the Yasa's paper [8] formulation (solving a linear system of two equations in two variables [1.8]).
The difference between this experiment and the previous one described in the section [1.1] is mainly considering frictional torque due to the bearing friction as a **non-constant value**: friction in this case is in fact a linear function depending on the rotating speed ω; the new procedure requires the fitting of the experimental data to a system of two non linear equations with three variables: inertia I and 2 friction parameters, c_1 and c_2.[1]

1.2.1 Mathematical Model

In this section a brief overview of the logic and the equations used in this method is provided.

Acceleration Phase

During the acceleration phase the rotor is attached to a free falling mass, increasing the rotational speed of the system from a starting point of $\omega = 0\frac{rad}{s}$.
The conservation of energy if friction losses are considered constant is:

$$mgR - I\alpha(t) - c_1 = (I + mR^2)\alpha(t) \tag{1.13}$$

which is basically the same as [1.5] in the Yasa's method 1.1.

$$\omega_b = \omega_a + (t_b - t_a)\frac{mgR - c_1}{I + mR^2} \tag{1.14}$$

In the new Povey's method [9] the frictional model torque now considered as $T_F = c_1 + c_2\omega$, so its trend is proportional to the variable angular speed ω.
The acceleration phase, starting from t_a and ending in t_b is described by this law:

$$mgR - c_1 - c_2\omega(t) = (I + mR^2)\alpha(t) \tag{1.15}$$

The velocity at t_b is ω_b, in this case this would be the maximum velocity at the end of the acceleration phase.[2]

[1] To give more context and aticipate the hypothesis of this experiment the linear dependance between friction and angular velocity is described by this law:
$T_F = c_1 + c_2\omega$
the parameters c_1 and c_2 are two constants obtained after an optimization process as well as the value of the Inertia.

[2] As it will be later described with accurate detail, in the new 2024 experimental setup the candidate does not select the maximum speed as the ω_b reference, instead it is chosen a given value within the interval of minimum and maximum angular velocity during the deceleration phase to increase the accuracy of the measurements and take always the same range of speed for each test.

$$\omega_b = \frac{mgR - c_1}{c_2} - [(\frac{mgR - c_1}{c_2} - \omega_a)e^{\frac{-c_2(t_b - t_a)}{I + mr^2}}] \tag{1.16}$$

It is also possible to evaluate the angular position by integrating the previous law

$$\theta_b - \theta_a = \frac{I + mR^2}{c_2}(\omega_a - \omega_b) - \frac{(mgR - c_1)(I + mR^2}{c_2^2} \ln \frac{mgR - c_1 - c_2\omega_b}{mgR - c_1 - c_2\omega_a} \tag{1.17}$$

Deceleration Phase

When the mass reaches the ground the deceleration phase begins and the rotor starts to decrease its rotational speed, mainly due to the friction of the bearings mounted on the rotor's assembly.
The main equation[3] describing this phase is now:

$$-c_1 - c_2\omega(t) = I\alpha(t) \tag{1.18}$$

Similar equations to the previous ones [1.16, 1.17] can be used to find ω_d and the total angular displacement $\theta_d - \theta_c$.

$$\omega_d = \frac{-c_1}{c_2} - [(\frac{c_1}{c_2}\omega_c)e^{\frac{-c_2(t_d - t_c)}{I}}] \tag{1.19}$$

$$\theta_d - \theta_c = \frac{I}{c_2}(\omega_c - \omega_d) - \frac{c_1 I}{c_2^2} \ln \frac{c_1 + c_2\omega_d}{c_1 + c_2\omega_c} \tag{1.20}$$

Frictional Torque Exponential Law

An alternative would be considering frictional torque as an exponential law

$$T_F = a\omega^b$$

it's not an effective way as the angular velocity is expressed in a variable of time are complex functions numerically, so it's not a valid option in this case.
During the 2024 experimental campaign the candidate, under the technical guide of his supervisor, PhD Candidate Lorenzo Da Valle, implemented this complex method for the first time. L. Da Valle solved the complex system of equations considering the frictional torque as exponential function of the angular velocity and found out a new numerical solution to describe the evolution of the variables $\theta(t)$ & $\omega(t)$.

$$\theta(t) = ae^{-bt} + cte^{-bt} + k_1 t + k_2 \tag{1.21}$$

$$\omega(t) = -bae^{-bt} + ce^{-bt} - bcte^{-bt} + k_1 \tag{1.22}$$

More details in the appendix [A.3].

1.2.2 Output of Povey's Paper Analysis

There are two limit cases regarding these two variables c_1&c_2: taking as reference the numerical and visual data of the paper [9]:

- Constant friction condition: $c_2 = 0$ $T_F = 4.49$

[3]As a reminder $\alpha(t)$ is the instant rotational acceleration value, while $\omega(t)$ is the instant angular velocity value

- Zero friction at zero speed $c_1 = 0$ $T_F = 1.591\omega$

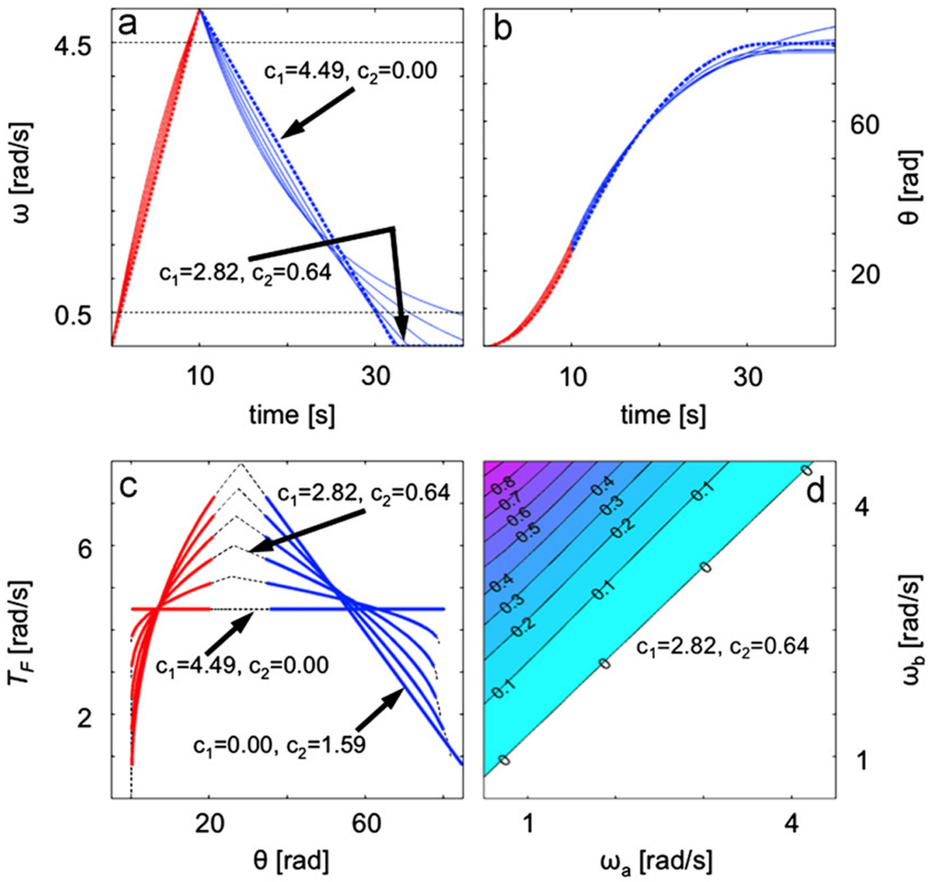

Figure 1.5: In the figures (a) and (b) there are shown variations of angular velocity and position; the dotted lines are the limit case $c_2 = 0$, the other lines proceed to the condition limit $c_1 = 0$. In red there is the acceleration phase, in blue the deceleration phase

Two first observations can be made from the first graphs:

- In the acceleration region the gradient of $\omega(t)$ decreases with increasing ω, this is due to a reduction with speed caused by the increasing T_F.
- In the decelerating phase it's the exact contrary: while ω decreases the gradient of $\omega(t)$ increases when the angular velocity ω has higher values.
  In the case limit of $c_1 = 0$ the gradient comes asintotically to zero.

In this experiment it was an implicit assumption considering the angular velocity following the reference condition with constant friction.
The angular velocity span for this testing campaign was considered between $0.5 \leq \omega \leq 4.5[\frac{rad}{s}]$ and both acceleration and deceleration ranges were considered: this created the condition to consider the work done against friction assuming the mean frictional toque was the same for both the phases.
During both parts of each test T_F trends were monotonic but $T_F(\theta)$ was different as frictional torque is not linear if considered variable in θ.
As a result, due to this trend the integrals regarding frictional work were different, and they generate an error witch was maximum 1% for the range $0.5 \leq \omega \leq 4.5[\frac{rad}{s}]$; to reduce the uncertainty in these cases the best common solution was taking a larger angular range for each test.

The base equation from where the error is evaluated is considering the following hypothesys:[4]

- $c_2 = 0$ Constant friction condition.
- $T_F^{ab} = T_F^{cd}$ Friction torque is equal in the accelerating and decelerating phases.
- The equation for inertia in this case is:

$$I = mr\{2g - r(\frac{\omega_b^2 - \omega_a^2}{\theta_b - \theta_a})\}/(\frac{\omega_b^2 - \omega_a^2}{\theta_b - \theta_a}) - (\frac{\omega_d^2 - \omega_c^2}{\theta_d - \theta_c})$$

Experimental Approach Overview and Plot of the results

In this experiment the rotor is supported by two oil lubricated bearings; rotor is attached to a 5kg mass to a cylinder whom radius is $R = 0.2869$m; the angular displacement is measured by an encoder that delivers 1024 pulses per revolution.

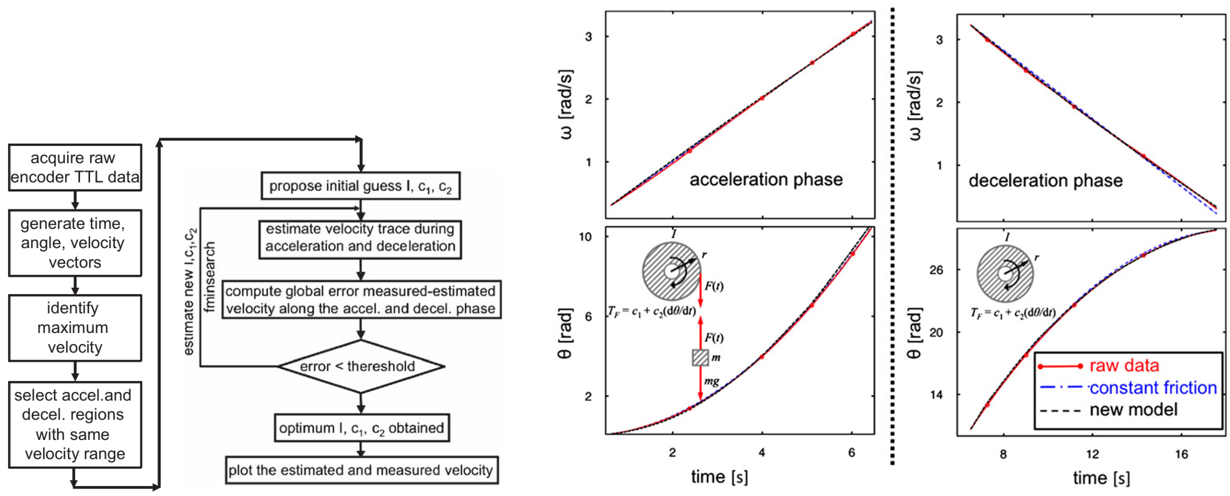

(a) *Data processing algorithm.*

(b) *Velocity and angular displacement for the acceleration and deceleration phase.*

Figure 1.6: Data processing algorithm in (a), then results comparison between the raw data from the experimental evaluations (in red), the old evaluation with constant friction model (in blue) and the new theoretical model with friction calculated in a non linear base (in black).

The encoder data was first transformed into angle using the raw instantaneous output; the velocity was evaluated using central differences up to the 4th order.
The angular velocity reduction is calculated so the difference $\Delta\omega$ in $\omega_b - \omega_a = \omega_d - \omega_c$; using Matlab the optimization of the error between the experimental velocity and the non linear equations model was possible using the algorithm shown in image [1.6(a)] [5].

[4]These hypothesys are exactly the same reported in section [1.1] when describing the Yasa's method [8], there is only a simplyfied version of the equation used to calculate the inertia's value.

[5]For the candidate's project it a whole algorithm from zero has been generated. To get the results for the new experimental setup instead of using the function "fminsearch" in Matlab to optimize the solution of two non linear equations [1.16] and [1.19] in the three variables $[c_1; c_2; I]$ it was used the "fsolve" method. More detailed information in Appendix 1, section [A.2] about the coding logic behind the new experimental setup post processing data procedure.

1.2.3 Results and Conclusions

As figure [1.7] shows, three experiments were carried out:

1. Rotor alone
2. Rotor + $0.001[kg/m^2]$
3. Rotor + calibrated disk $2.006[kg/m^2]$

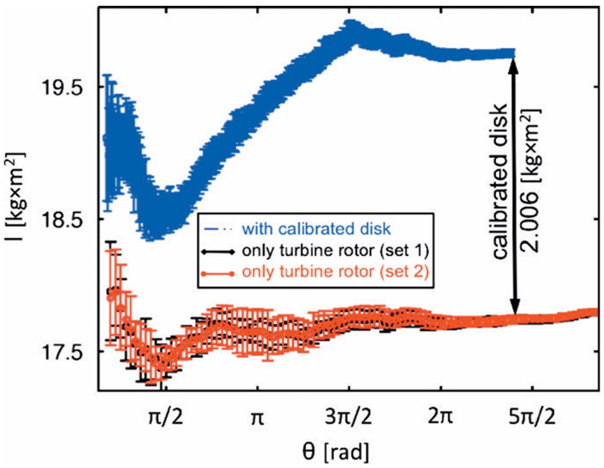

(a) *Inertia trend depending from the angular displacement. The solid red line represents the raw data, the dotted blue one represents the constant friction model. The dotted blue line represents the new model and shows a significant similarity with the raw data.*

RESULTS at 2.3×π		$\bar{x}$	*1.96*σ* [%]
New method	*I*	17.7322	*0.099*
Rotor only	*c1*	3.1583	*2.24*
(11 tests)	*c2*	0.6642	*4.38*
New method	*I*	17.7352	*0.089*
Rotor & 0.001 kg.m^2	*c1*	3.1148	*2.16*
(11 tests)	*c2*	0.6772	*4.22*
New method	*I*	19.7468	*0.076*
Rotor & 2.006 kg.m^2	*c1*	3.1110	*2.84*
(11 tests)	*c2*	0.7801	*5.01*
Constant friction Rotor only	I_{rotor}	17.739	0.500
Constant friction Rotor & 2.006 kg×m^2	I_{rotor}	19.604	0.282

(b) *Table of resuts*

Figure 1.7: The results table shows the results with different tests and conditions.

Better results were achieved when including the calibrated disk; the non linear model reduces the uncertainty with a factor equal to 5 referring to the previous study [8].
To conclude the overview on the Povey method, these results showed how a new technique to measure accurately the moment of inertia in turbomachinery rotors.
The accuracy mismatch is due to the non-linear friction model assumptions and thanks to data optimization tools the non linear equations could be solved.
This method as well as the Yasa's one were carried out and adapted to the new experimental setup for the 2024 Inertia Measurements; as it is described in the chapter [3] and appendix [A.2] the new input data were put into the new code to obtain the final measured Inertia's value and its uncertainty on the new rotor mounted on the "CT3" facility.

1.3 General Overview of the CT3 facility at the Von Karman Institute

In this section an overview of the Compression Tube facility "CT3" at the Von Karman Institute for Fluid Dynamics is shared with the readers; an accurate description of the whole setup and some information about how a complete test is conducted in this facility are shown to the reader to give more context and clear any missing information or some doubts coming from the previous sections [1.1 & 1.2].
The information shared in this section are based on the paper [4] written by the authors R. Dénos, G. Paniagua, T. Yasa and E. Fortugno, providing a complete description of the facility as well as a case-study of how it works during actual tests with the facility closed and fully operative[6].

Introduction

The transonic turbine stage efficiency can be tested in a compression tube facility: considering already losses and other secondary flows (coolant, leakage etc.).
The methodology proposed is a test made within 0.5 seconds of testing time: results are shown in this paper as

- Power
- Overall mass flow
- Mass-averaged inlet quantities
- Pressure

The turbine efficiency is defined by the ratio between the power effectively extracted from the fluid and the power obtained form an isentropic expansion[7]:

$$\eta = \frac{P_{effective}}{P_{isoentropic}} \tag{1.23}$$

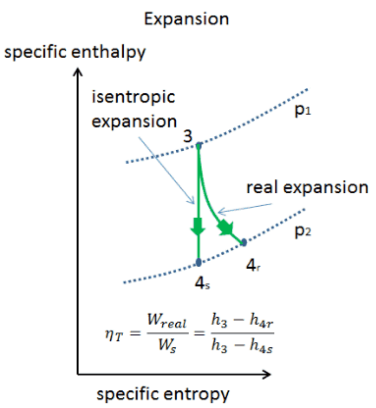

Figure 1.8: Example of an isentropic and and effective expansion in a turbine.

To effectively test this efficiency the testing conditions would require to create an adiabatic environment, but as it's known for large pressure ratios large temperature gradients manifests in the turbine, leading to heat transfer along the airfoils and the walls. Usually efficiency is measured in continuously running facilities, in which the flow is allowed to stabilize itself; there are usually two ways of measuring the efficiency in these cases:

- Thermodynamic method:
  More complex way of measurements: requires accurate measurements of upstream and downstream temperature and pressure along the span.
- Mechanical method:
  Provides an integral value of the efficiency based on the measurements of the rotor's torque; this was the methodolgy used for the new experimental setup.

The other requirement of this measurement is the uncertainty of the value of the efficiency: it has to be under 1% to be considered

[6] Keep in mind the new experimental setup project (2024) the candidate worked on was supposed to have the "CT3" facility opened, this means that the actual compression tube was not in function or even considered during the testing campaign and all the measurements were conducted on solely the rotor assembly.

[7] An isentropic transformation is an adiabatic and reversible transformation, as shown in the image 1.8

valid.

Short Duration Facilities

Since the 1970's these facilities have taken place and their use contributed largely on the actual knowledge of unsteady flows and heat transfer phenomena in turbines[8].
In these facilities the testing time is under one second, so it is challenging to actually measure accurately all the required parameters in such a short time span: for temperature measurements these facilities are not optimal due to the heat loss problem and the high temperature gradient, so the thermodynamic method of measurement for the efficiency is inaccurate.
For this reasons the preferred method is the mechanical measurement based on torque calculations.
In the article [4] (based on 2006 updates) the VKI compression tube CT3 facility was capable of measuring the turbine efficiency following these calculations steps:

1. Turbine torque
2. Mainstream mass flow
3. Coolant and leakage mass flow
4. Mechanical losses

Total pressure ratio during the experiment was constant and so was the speed line [same intervals of speed considered in the acceleration and deceleration phases].

Experimental Test Facility — VKI Compression Tube CT3

In the VKI[9] the turbine stage is tested in a compression tube facility that emulates the real engine operating conditions.
Thanks to a shutter valve (see figure [1.9]) the exit flow is controlled and the pressure is set at approximately 20 mbar and the rotor design speed is set to $6500rpm$.
Then, cold high-pressure air is admitted in the back of the piston that starts travelling forward; downstream of the piston, the air is compressed quasi isentropically.
The pressure in the tube was initially set to a value such that the target levels of temperature and pressure are reached during the compression:

$$\frac{T0_{tube-final}}{T0_{tube-initial}} = (\frac{p0_{tube-final}}{p0_{tube-initial}})^{\frac{\gamma-1}{\gamma}}$$

When these levels are reached, the fast opening shutter valve is actuated and hot pressurized air is released on the cold turbine allowing heat transfer similarity.
The mass flow is controlled by a sonic throat placed between the turbine exit and the dump tank.
The test ends when the piston has reached the end plate or when the pressure in the dump tank is too high to have choked conditions in the sonic throat.
After a short transient nearly constant flow conditions are maintained for 300 ms, then all the net power of the turbine is converted into kinetic energy[10]; the usual window favorable for the tests are the 40 ms prior to the end of the test itself.

[8]Short Duration Facilities enable testing at the actual engine levels of Reynolds number, Mach number, gas to wall and gas to coolant temperature ratios.

[9]To clarify, "VKI" is the short variation of "Von Karman Institue for Fluid Dynamics".

[10]I.e. the rotor is being accelerated by the hot pressurised air flowing into the testing section

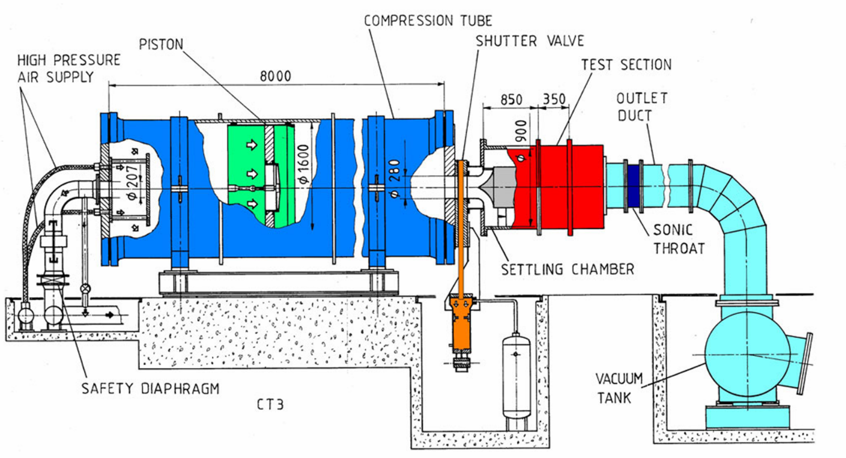

Figure 1.9: Compression tube facility "CT3" lateral schematic view: in the left in blue the large compression tube (diameter x and length y), in orange the shutter valve used to control the mass flow in the testing section (in red) where are positioned the stator and the rotor; note both these last two parts can be substituted after each project's testing period is over.
On the right in ligh blue there is the outlet tube where the mass flow is directed to the vacuum.

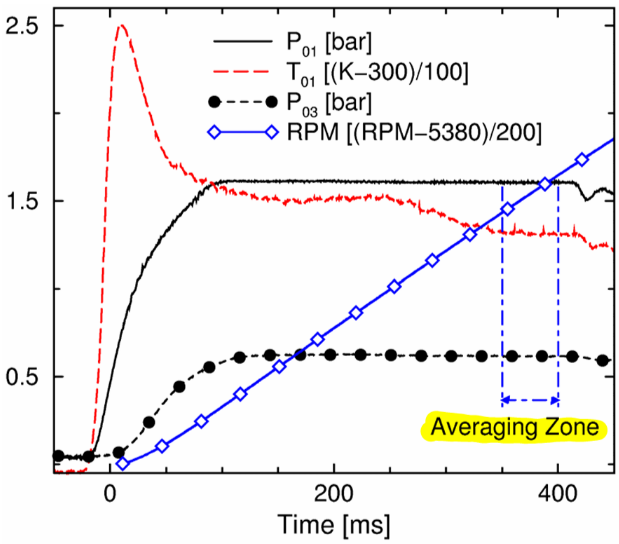

Figure 1.10: Pressure and temperature values during the entire time of the test, data taken from the inlet section, in this figure it evidenced the usual time zone where data are collected at the end of the test (when the total pressures are fairly stable over time).

Nominal Operating Conditions

In the following table there are the main values of interest for the nominal operating conditions in the transonic tube:

	Symbol	Value
N° Rotor Blades		64
N° Stator Blades		43
Pressure Ratio	$\frac{P_01}{s3}$	3
Loading Coefficient	$\Delta H/U^2$	1.7
Reynolds Number	$Re_{2_{Cs}}$	10^6
Mass flow	m_f	10.5 kg/s
Coolant Mass Flow	$m_coolant$	3% mass flow
Mach Numbers	$M_2 - M_3, r$	1.03 - 0.89
Temperature Ratio	$\frac{T_{01}}{T_wall}; \frac{T_{01}}{T_{coolant}}$	1.5

Table 1.1: Nominal condition values

Due to the difficulties in centering the rotor and stator axis with extreme precision $\pm 0.1mm$ this leads to a final value of clearance of $0.6mm$ which is 1.2% of the total blade height at inlet.

Efficiency Formulation

Definition of aerodynamic isentropc efficiency:

$$\eta = \frac{P_{real,adiabatic}}{P_{isentropc}} = \frac{\dot{m}(H_{01-H_{03}})}{\dot{m}(H_{01} - H_{03_{iso}})} = \frac{\dot{m}C_P(T_{01} - T_{03})}{\dot{m}C_P T_{01}(1 - (\frac{P_{03}}{P_{01}})^{(\frac{\gamma-1}{\gamma}}))} \tag{1.24}$$

The temperature drops across the turbine in this test is only $\approx 100K$ so the pressure coefficient was evaluated as constant considering the mean value between T_{01} and $T_{03_{is}}$; same for the γ parameter.
To obtain a good result both parameters γ and C_P have to be determined with decent accuracy. Due to the presence of heat transfer an ideal reversible evolution, including the cooling system, would exceed the maximum efficiency ≥ 1 thanks to a deacrese of entropy, which in the real case is phisically impossible [11].
We have to consider also the aerodynamic losses in the stage, heat transfer has an overall effect of a $\approx 3K$ decrease on the total 100 K temperature drop, so the aerodynamic losses are not affected by this value.
The efficiency of the expansion process, heat transfer included, will be considered the same as the adiabatic transformation and it is assumed that the heat transfer and the aerodynamic process both have the same efficiency.

$$\eta = \frac{\Delta T_{adiab} + \Delta T_{HT}}{\Delta T_{is} + \Delta T_{HT,is}} \tag{1.25}$$

So the effective enthalpy drop with the presence of heat transfer is assumed equal to the one measured in an adiabatic turbine.

$$\eta = \frac{\Delta T_{adiab}}{\Delta T_{is}} \tag{1.26}$$

The mechanical method used for this test is by measuring the shaft power:

$$P_{real} = P_{shaft} + P_{loss} = I\omega\frac{\delta\omega}{\delta t} + P_{loss} \tag{1.27}$$

[11] The second law of thermodynamics states that the total entropy of an isolated system either increases or remains constant in any spontaneous process; it never decreases.
If a process is reversible it means the enthropy will remain constant due to absence of losses (this is usally an ideal case); in all other real cases losses will be present and the entrophy of the system will increase.

Losses are considering the bearing friction and the ventilation caused by the airfoils exposed to the flow; also control volume has to be considered (for example mixing losses and poor diffusion in the exit duct may effect the efficiency measurement for a long control volume).
It has to be considered that leaks can take place at the upstream and downstream interfaces with the rotor platform: downstream of the rotor, the cavity is filled quickly and the pressure is equal to the free stream pressure at hub during the run time but this is not the case of the upstream cavity, that is larger.
Despite that all these leaks are quite small, just 0.5% of the total mass flow, so pressure and temperature at the inlet and the outlet of the control volume can be considered the same:

$$\begin{cases} P_{01} \approx P_{02} \\ T_{01} \approx T_{02} \end{cases} \tag{1.28}$$

Considering now for the power equation [1.27] also the coolant losses and the leakage losses the equations changes in:

$$P_{is} = (\dot{m}_{in} - \dot{m}_{leak})C_P T_{01}[1 - (\frac{P_{03}}{P_{01}})^{\frac{\gamma-1}{\gamma}}] + \dot{m}_c C_{pc} T_{0c}[1 - (\frac{P_{03}}{P_{0c}})^{\frac{\gamma-1}{\gamma}}] \tag{1.29}$$

This equation is correct only if the coolant and the leakage flows are considered constant, so basically only if the flow at the inlet and the outlet of the control volume is uniform; in the real case pressure and temperature vary along both the radius or the pitch. The [1.29] equations will be described by surfaces integral on both terms.

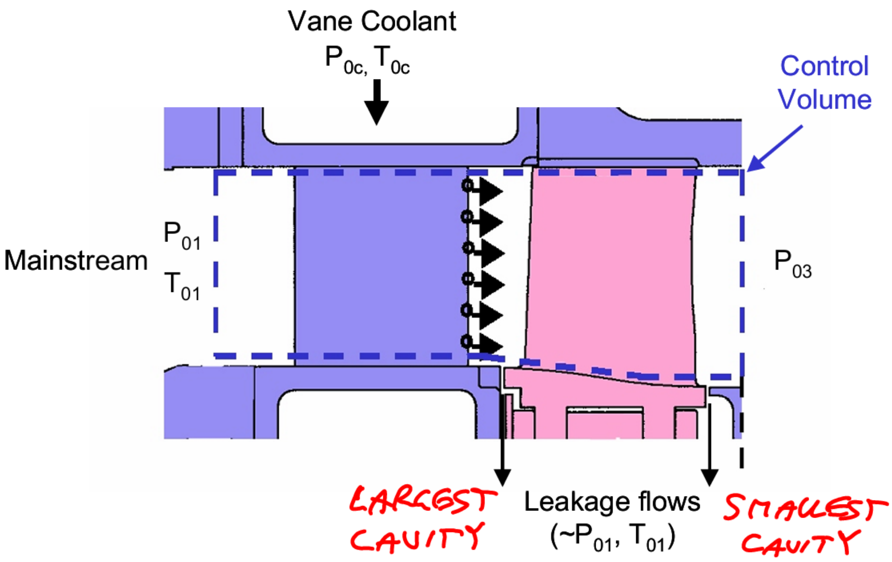

Figure 1.11: Control volume considered for the efficiency measurement

Not knowing the exact trajectory of the flow, especially at the inlet part of the volume the exact pressure ratio cannot be computed, so the following equation must be approximated (total pressure and mass flow quantities are mass flow averaged):

$$P_{is,med} = C_P \bar{T}_{01}(1 - (\frac{\bar{P}_{03}}{\bar{P}_{01}})^{\frac{\gamma-1}{\gamma}}) \tag{1.30}$$

The final equation for the efficiency of the turbine stage is:

$$\eta = \frac{P_{real} + P_{heat}}{P_{iso} + P_{heat}} = \frac{I\omega\frac{\delta\omega}{\delta t} + P_{loss}}{(\dot{m}_{in} - \dot{m}_{leak})C_P \bar{T}_{01}[1 - (\frac{\bar{P}_{03}}{\bar{P}_{01}})^{\frac{\gamma-1}{\gamma}}] + \dot{m}_c C_{pc} T_{0c}[1 - (\frac{\bar{P}_{03}}{P_{0c}})^{\frac{\gamma-1}{\gamma}}} \tag{1.31}$$

Test Conditions

The test conditions were the following in [4]:

- Inlet pressure $P_{01} = 1.62$ [bar]
- Inlet Temperature $T_{01} = 440$ [K]
- Pressure Ratio $\frac{P_{01}}{P_{03}} = 3$

In the following figure [1.12] are shown both the test consditions taken form the a turbine map and the results of the test:

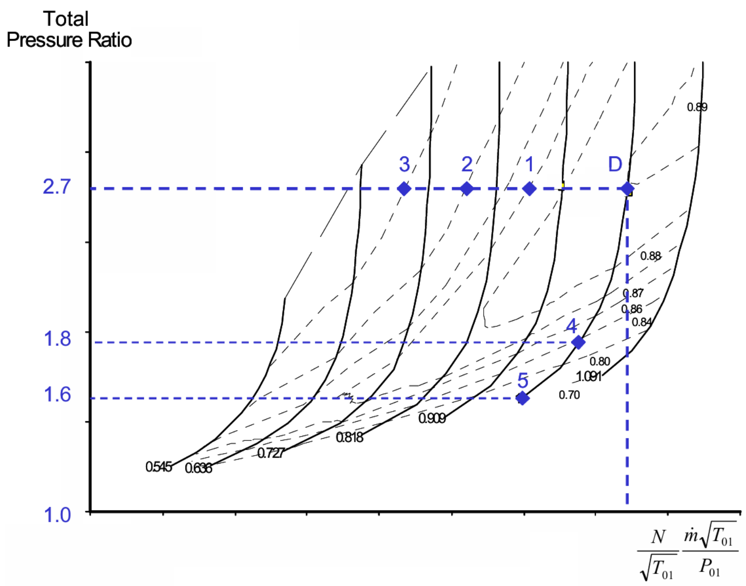

(a) *Turbine map and operating conditions; D is the design operating condition at 6500 rpm*

	Speed [RPM]	P_{01}/P_{03} [bar]	P_{01}/P_{s3}	M_2	α_{2r} [deg]	Incid [deg]	α_3 [deg]	dotm [kg/s]	Power [MW]	η (NISRE)	η (map)
D	6500	2.691	3.051	1.03	45.8	0.0	13.1	10.87	1.093	0.934	0.89
1	5720	2.691	3.133	1.07	53.1	7.3	24.3	10.89	1.075	0.915	0.87
2	5096	2.691	3.246	1.12	57.4	11.6	31.8	10.87	1.044	0.887	0.84
3	4550	2.691	3.382	1.17	60.3	14.5	36.9	10.86	1.000	0.846	0.80
4	6500	1.808	1.930	0.84	32.0	-13.8	-26.8	10.60	0.677	0.938	0.80
5	6500	1.591	1.700	0.75	19.9	-25.9	-39.5	10.30	0.520	0.933	

(b) *Results of the tested operating conditions*

Figure 1.12: General turbine operating conditions compared to the testing results in the "CT3" facility.

1.3.1 Measurement of Power, Mass Flow and Losses

Inertia

To measure the rotor inertia (in a mechanical way) it is considered the technique already treated in the previous sections [1.1 & 1.2]: the rotor is accelerated by a falling mass attached to the rotor itself by a steel wire.

The friction model in this case considers the energy loss form bearings friction etc as a function of the angular displacement and the velocity range (considered in the term "Fr").

$$\Delta E_{friction} = \int_a^b Fr\, dx \approx Fr(\theta_b - \theta_a) \tag{1.32}$$

As it was already covered in the previous articles [1.1, 1.2] the test is divided in two phases, phase A is the accelerating part [see 1.2.1 to have a more precise description], phase B [1.2.1]is the decelerating one.
If the same velocity ranges are selected the graph shown in figure [1.13] is mostly an accurate representation of the velocity trend during the test.

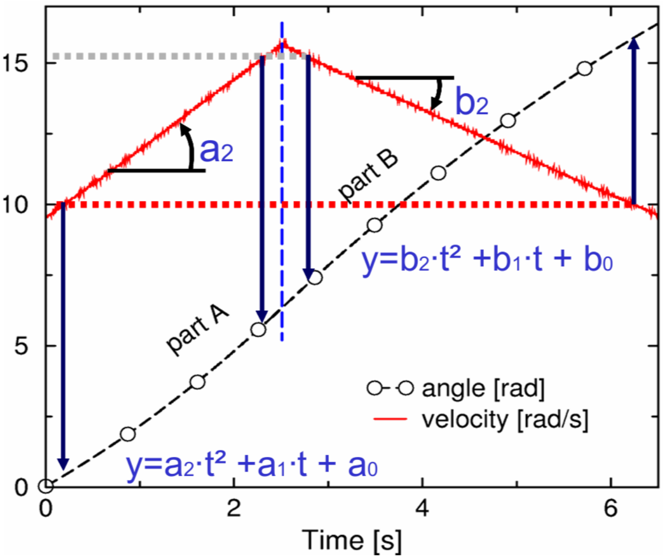

Figure 1.13: Velocity traces in the acceleration and deceleration phases (in red) and angular displacement measurements (in black) during the free falling mass test.

The already cited in section [1.1] conservation of energy equations for both phases are: Accelerating Phase Equations:

$$\Delta E_{potential} = \Delta E_{kinetic} + \Delta E_{friction} \tag{1.33}$$

$$Rmg(\theta_b - \theta_a) = (I_{disk} + I_{rotor} + mR^2 + I_p\frac{R^2}{r^2})\frac{(\omega_b^2 - \omega_a^2)}{2} + \bar{F}_r(\theta_b - \theta_a) \tag{1.34}$$

Decelerating Phase Equations:

$$0 = \Delta E_{kinetic} + \Delta E_{friction} \tag{1.35}$$

$$0 = (I_{disk} + I_{rotor} +)\frac{(\omega_c^2 - \omega_d^2)}{2} + \bar{F}_r(\theta_c - \theta_d) \tag{1.36}$$

After combining the previous equations the **rotor inertia** can be computed (assuming a quadratic evolution of the rotor displacement).
By using the values of accelerations in both phases a_2 and b_2 the final simplified equation for the rotor inertia measurement is [12]:

$$I_{rotor} = \frac{Rm(g - 2a_2R - \frac{2I_pRa_2}{mr^2})}{2(a_2 - b_2)} = 17.7483 \pm 0.47\% kgm^2 \tag{1.37}$$

The final result is due to calculations completed considering both the presence or the absence of calibrated disks and two falling masses of approximately five and ten kilograms.

[12]Symbols legend: pulley's inertia $I_p = 1.035 \cdot 10^{-3} kgm^2$; radius of the rotor where the cable is attached $R = 0.2869m$; pulley's radius $r = 0.07385m$; gravity acceleration $g = 9.8113m/s^2$

Rotational Speed and Acceleration

Thanks to an incremental encoder it is possible to measure the angular displacement of the rotor: with a 80MHz clock frequency periodmeter the accuracy in this measurement is increased (uncertainty of the measure is $\approx 10^{-5}$ if the rotational speed is evaluated every revolution or $\approx 10^{-3}$ if the rotational speed is evaluated every pulse.
After a careful consideration on evaluating the uncertainty for the acceleration measurement, it was chosen to measure the speed every two revolutions and the acceleration every 1.5 revolutions.
The acceleration is then obtained by using this derivative:

$$\frac{\delta\omega}{\delta t} = \frac{CP_{01}\eta C_P\sqrt{T_{01}}(1-\frac{P_{03}}{P_{01}})^{\frac{\gamma-1}{\gamma}}}{I\omega} \tag{1.38}$$

The acceleration is linked to:
- Inlet Total Pressure P_{01}
- Inlet Total Temperature T_{01}
- Exit Total Pressure P_{02}

Results during the test time [0.1 sec] are shown in figure [1.14]:

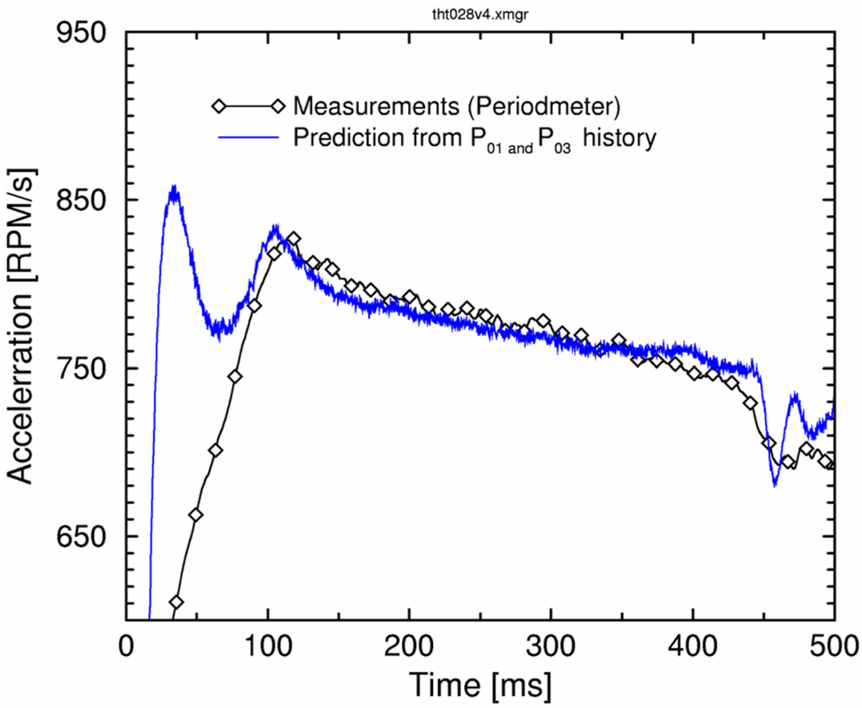

Figure 1.14: Acceleration-Time gaph, comparison between actual data measured and pressure preditcyion

In theory during this test the power should have been constant, as well as the total pressure, but in reality total pressure decreased a little so it caused a variation of the acceleration; however both the theoretical and the experimental model gave similar results.

Mechanical Losses Evaluation

The mechanical losses are mainly due to friction of the bearings, a smaller fraction of the losses are due to the rotor disk.

Frictional torque can be expressed following the Traupel formulation [13]:

$$T_{bearings} = C_{bearings} N^{n_{bearings}} \tag{1.39}$$
$$T_{windage} = \rho C_{windage} N^{n_{windage}} \tag{1.40}$$

The loss of power due to the ventilation effects is:

$$P_{ventilation}[kW] = \rho C_{ventilation} (\omega \frac{D_{ext}}{2})^{n_{ventilation}} \tag{1.41}$$
$$n_{ventilation} = 3 \tag{1.42}$$
$$C_{ventilation} = f(D_{ext}, H) \tag{1.43}$$

The loss of power due to the bearings depends on the angular velocity:

$$P_{bearings_{axial}}[W] = 2.293 \cdot 10^{-5} RPM^2 - 5.644 \cdot 10^{-3} RPM^2 + 3.9 \tag{1.44}$$

In the following figure [1.15] different losses are shown in the relative critical area:

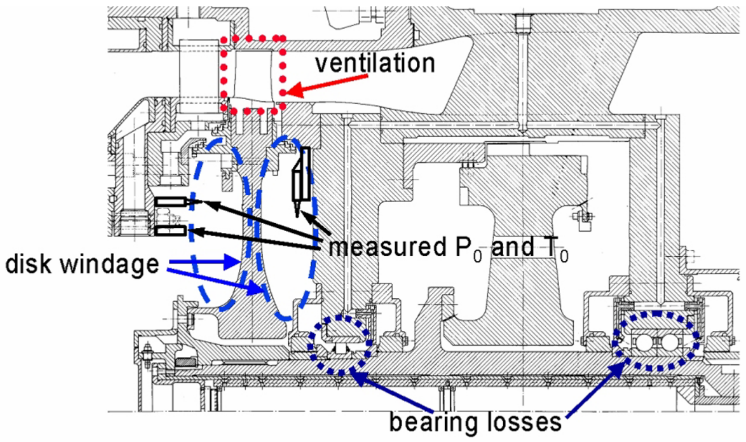

Figure 1.15: Different losses and their location in the turbine stage.

The windage losses evolution is completely opposite to the bearings ones: in this case windage losses increases with density; to distinguish between the two different losses deceleration tests were performed to see the pressure evolution, see figure [1.16].
To calculate all the coefficients for both the main losses an iterative procedure was required: it compared the rotational speed history predicted by the model with the measured one and the coefficients were adjusted to minimize the differences between the experimental data and the theoretical model.

[13] $C_{bearings}, C_{windage}, n_{bearings}, n_{windage}$ are the coefficients gathered from the deceleration test.
During the deceleration test, the kinetic energy of the rotor decreases not only due to the mechanical and windage losses but also due to blade ventilation losses, whom are due to the flow drag of the still air on the rotor airfoils.

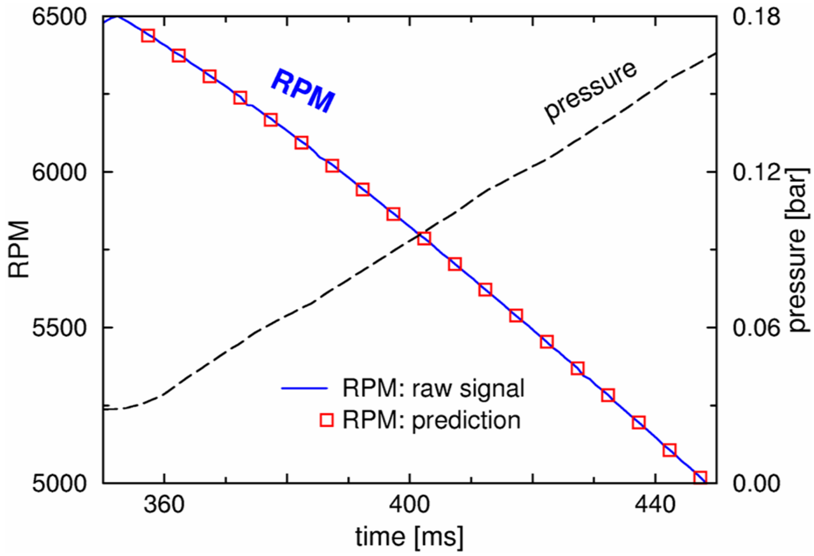

Figure 1.16: Deceleration test to see the evolution of pressure and rotational speed.

The result in overall power losses follows this experimental equation that includes both windage and bearing factors:

$$P_{\text{losses}}[\mathrm{W}] = 2.244 \times 10^{-7} \cdot \mathrm{RPM}^{2.3881} + 0.1369 \cdot \mathrm{RPM}^{1.30768} + 2.293 \times 10^{-5} \cdot \mathrm{RPM}^{2} - 5.644 \times 10^{-3} \cdot \mathrm{RPM} + 3.9 \approx 14.6 \text{ kW}$$

Axial load losses were considered in the final uncertainty calculations as a value of 10%.

1.3.2 Results

Efficiency

To collect the data a gaussian probability function is assumed with 95% of the measurements taken in consideration.

	Efficiency	Disp (20:1)	Disp [%]	nb tests	% on mean
D	0.9088	0.0046	0.51%	17	0.12%
1	0.8852	0.0044	0.50%	10	0.16%
2	0.8478	0.0030	0.35%	10	0.11%
3	0.8058	0.0021	0.27%	10	0.08%
4	0.9033	0.0031	0.34%	10	0.11%
5	0.9109	0.0072	0.79%	10	0.25%

Figure 1.17: Efficiency values measured at different operating conditions: "D" (on design condition) shows a result of $\eta \approx 90\%$ efficiency which is really high, this result is due to the state of art tools used and this result was also confirmed by then simulating the operating turbine stage with 3D Navier-Stokes CFD tools.

In the following figures [1.18] the results were compared considering three measurements:

- Turbine Map Data (only taken for reference)
- Actual Measured Values

- NISRE (Non-Isentropic-Simple-Radial-Equilibrium) simulation

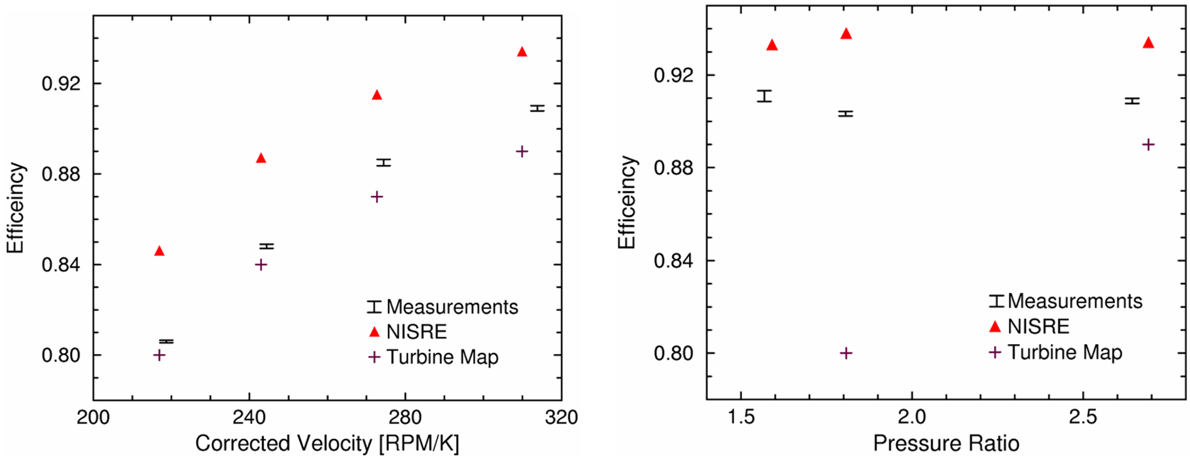

(a) *Efficiency results compared to the angular velocity variation and the three methods considered*

(b) *Efficiency results compared to the pressure ratio variation*

Figure 1.18: Measured level of efficiency, turbine map reference and NISRE simulation: both the actual measurements results and the simulation results trend appear to be similar, so the experimantal campaign was considered successful.

Uncertainty Analysis

After the test campaign the uncertainty evaluation was performed for this experimental project: due to the large number of measurements it was decided to estimate the derivatives numerically by varying each x_i by its uncertainty Δx_i. In substance finite differences where chosen like this:

$$\frac{\partial \eta}{\partial x_i} = \frac{\Delta \eta}{\Delta x_i} \tag{1.45}$$

$$\Delta \eta \approx \sqrt{\sum_{i=1}^{N} \Delta \eta_i^2} \tag{1.46}$$

The process consists in calculating first the nominal value of the efficiency using all the measured values; then, each of these values is varied successively by its uncertainty and a new value of efficiency is computed every time.
The difference between each of these values of efficiency and the nominal value is computed and the squared differences are added; finally, the square root provides the uncertainty of the nominal value of efficiency.
The sensitivity is also derived as the ratio between the percentage of variation of a value and the corresponding percentage change on the efficiency; in the end the contributions are divided in a systematic error and a random error.
The systematic error[14] results in a 1.2% on the efficiency, hence it is not a very accurate result.
The random error main contributors are P_{03} and P_{01}, for an overall inaccuracy of $0.7-1.3\%$ depending mainly on the pressure ratio value during the test[15].

[14]The sysematic error main contributors are inlet pressure P_{01} temperature T_{01} and the γ parameter due to the accuracy limits of the probes, also the mass flow and inertia have great contributions to this value

[15]Lower accuracy was observed for the lowest pressure ratios.

				Random			Systematic		
Quantity	**Unit**	**Value**	**Sensitivity**	**Uncertainty**	**% param.**	**% eff.**	**Uncertainty**	**% param.**	**% eff.**
Exit M_{ass} F_{low}	[kg/s]	10.458	-0.978	0.0607	0.58%	-0.57%	0.0878	0.84%	-0.82%
Speed	[RPM]	6555.3	0.962	0.22	0.00%	0.00%	0	0.00%	0.00%
Acceleration	[RPM/s]	757.69	0.956	0.35	0.05%	0.04%	0	0.00%	0.00%
P_{01}	[bar]	1.5998	-3.508	0.001	0.06%	-0.22%	0.003	0.19%	-0.66%
T_{01}	[K]	429.3	-0.229	0.5	0.12%	-0.03%	5	1.16%	-0.27%
P_{03}	[bar]	0.6039	0.873	0.002	0.33%	0.29%	0.001	0.17%	0.14%
P_{0cool}	[bar]	1.496	-0.020	0.04	2.67%	-0.05%	0	0.00%	0.00%
T_{0cool}	[K]	292.7	-0.021	3	1.02%	-0.02%	0	0.00%	0.00%
Cool. $M_{ass}F_{low}$	[kg/s]	0.345	0.012	0.00734	2.13%	0.02%	0.00345	1.00%	0.01%
P_{loss}	[W]	14652	0.014	0	0.00%	0.00%	1465.2	10.00%	0.14%
g	0	1.3966	-2.075	0	0.00%	0.00%	0.0011	0.08%	-0.16%
c_p	[J/(kg.K)]	1010.7	-0.953	0	0.00%	0.00%	0.65	0.06%	-0.06%
Inertia	[kg.m2]	17.7483	0.956	0	0.00%	0.00%	0.0834	0.47%	0.45%
Value of efficiency		0.9088				0.00615			0.01095
						0.68%			1.21%

Figure 1.19: Uncertainty analysis result at on-design conditions.

To conclude the final results published in [4] of the testing campaign concluded on the "CT3" facility were:
Final value of the turbine's rotor stage efficiency:

$$\eta = 0.9088$$

Uncertainty analysis result: random error

$$err_r = \pm 0.68\%$$

Uncertainty analysis result: systematic error

$$err_s = \pm 1.21\%$$

1.4 Conclusions and significance of the literature review

These papers' reviews [8] [9] [4] have been included in this document (respectively in sections 1.1 ; 1.2 & 1.3) to give a meter of comparison between the results obtained in the previous experimental campaigns and the latest one (2024), which is in fact the real objective of this document itself.
Most importantly the mathematical methods introduced have been presented to the reader, we will refer in the following chapters to the formulation [1.8] as the "Yasa method" for Inertia measurement (from Paniagua & Yasa' work, [8] described in section [1.1]); same thing for the "Povey method" for Inertia measurement from Paniagua and Povey's work [9].
Using these two methods, adapted on the new setup, the 2024 experimental campaign on "CT3 Inertia Measurements" has been carried out, with the add-on of the alternative fitting firstly cited in section [1.2.1]: the new "exponential fitting" mathematical model (cited in the Povey article as a possible solution, put not pursued at that time) has been solved by Lorenzo Da Valle and applied for the first time in the 2024 campaign [detailed mathematical explanation in appendix A.3].
In brief the hypothesis of possibly finding a more accurate result by obtaining and using as an input a second smoother fitting of the theta vs time original data has been pursued.
In the following chapters [2], [3] it will be described in detail the object of this master's degree thesis: the new experimental setup's measurements of the inertia value of the new turbine stage currently mounted on the facility and its uncertainty will be proposed to the reader as well as all the process from preliminary design to the post processing routine to obtain the final results.

Chapter 2

New 2024 VKI's Experimental Setup Overview for Rotor's Inertia Measurements on the "CT3" facility

2.1 Introduction

In chapter [1] general information about the CT3 facility and the previous similar experiments are discussed: in this chapter it is shown the new experimental setup and methodologies used to calculate the rotor's inertia and its uncertainty.
The design of the new experimental setup has started following the first steps made by Yasa [1.1] as well as Povey [1.2]; the goal is to obtain the lowest error possible, ideally less then 0.1% on the inertia value; the uncertainty analysis calculated on the inertia value is based on the Taylor's theory [13] and it is shown more in detail in the Appendix [A].
To obtain this value two methods were used to calculate the inertia value:

- Yasa method (considering the friction torque as costant)
- Povey method (considering the friction torque variable linearly with the angular velocity value)

Different Acceleration - Deceleration tests have been conducted to demonstrate the effect of changing velocity ranges, masses, pulleys and wires and see if and how the inertia value and its uncertainty changes.
As it is suggested in the Povey [9] and Yasa [8] papers, as well as the test campaign conducted in 2023, the largest velocity ranges would lead to a more precise measurement as the inertia would have an asyntothic decreasing trend.

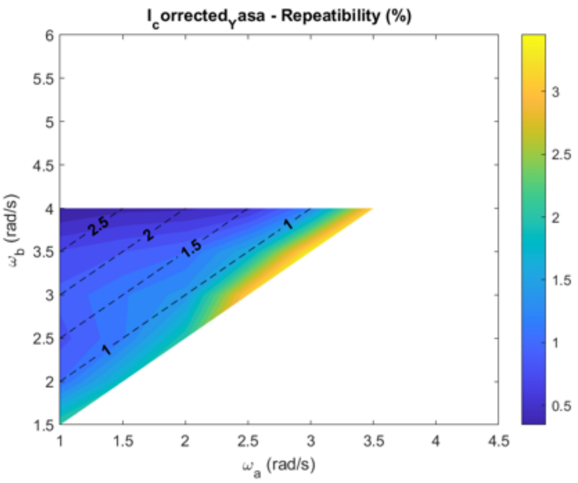

Figure 2.1: Output of the uncertainty measured on test n°6 taken as an example. As we can see looking at the legend on the left, the lowest uncertainty (or repeatibility percentage index) values have been observed on the left-high side of these contour plots.
In that area the values of ω_b are high and ω_a are low; in other words the uncertainty is in fact the lowest when the $\Delta\omega = \omega_b - \omega_a$ is maximum.

2.2 Encoder Selection

During the previous test campaign conducted by the PhD Candidate supervisor Lorenzo Da Valle in 2023, the encoder used to get the angular displacement data had a resolution of 10 bits and the measurements were deeply affected by the noise and friction due to the pulley system chosen; to increase the precision of the measurements it was assigned to increase the encoder's resolution to 16 bits and to design a new reliable setup.
The equation used to calculate the precision of the encoder is the following:

$$PPR = \frac{360°}{d\theta} \tag{2.1}$$

where PPR are the Pulses Per Revolution.
An encoder with a "x" number of bits resolution generates $2^{n° bits}$ pulses every revolution of the rotating component it is attached to.
In this project the the minimum pulses per revolution required are $2^{16} = 65536$ in order to obtain a reduction of the relative error to a value inferior than 0.5% on the evaluation of the Inertia on the rotor $I[\%] = \frac{\delta I}{I}$.
The product selected after a detailed evaluation with the project supervisors was an incremental encoder "DHM510" [2] (see image [2.3]); the 16 bits resolution lead to a $\delta\theta_{min} = 0.055°$ minimum angle displacement detected, the resolution requisite was satisfied within reasonable costs in the project's budget.
As it was conducted during the test campaign in 2023 the encoder selected had the requirement to give back as an output a TTL signal.
A TTL (Transistor-Transistor Logic) signal for incremental optical encoders is a digital signal used to transmit position information from the encoder to a receiving device.
There are a few key characteristics that are needed to describe a TTL signal for detecting the angular displacement of a rotating device.
the two logic voltage levels are:

1. Logic low (0): 0 to 0.8 volts
2. Logic high (1): 2.4 to 5 volts

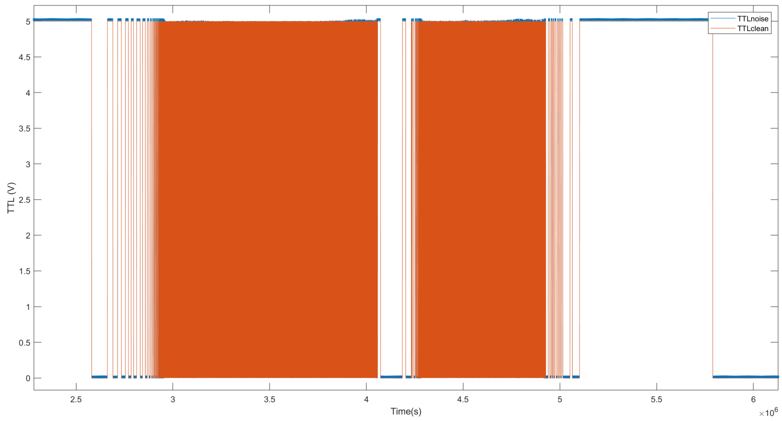

Figure 2.2: Example of a TTL signal from one of the preliminary tests made to test the new encoder on the new setup.
The blue signal is the raw signal including the noise detected by the encoder and the orange signal is the filtered data [switching exactly between 0 Volts and 5 Volts] after the first post-processing step.

The signal alternates between high and low states as the encoder shaft rotates and it creates a squared wave evolution of the signal between 0 volts and 5 volts during a certain time interval. Most incremental encoders use two main channels (A and B) and sometimes an additional index channel (Z) where channels A and B provide position and direction information while channel Z (Index) gives a reference point for one complete revolution.
For the optical type incremental encoder as the encoder shaft rotates, it interrupts light beams, generating pulses; the pulses are converted into TTL-level square waves and the receiving device counts these pulses to determine position; some encoder are also able to generate the speed output but in this case the speed values have been calculated during the post-processing phase and not directly by the DHM510 device[1].
By monitoring the phase relationship between channels A and B, the direction of rotation can be determined: in the case of the encoder DHM510 there was only one direction of rotation so it was not necessary to buy a "multi-turn" type of incremental encoder.
The advantages of using a TTL signal instead of an analog one are: fast switching, allowing for high-speed position feedback and noise immunity.
This encoder has been chosen for its compatibility with the Data Acquisition System already available in the Turboachinery laboratory of the Von Karman Institute: the "Genesis Tower" device that can read the TTL signal via a BNC cable connection.[2]

[1]This product was selected between a few other similar options from the store "Blintz Technics" based in Brussels (BE)
[2]More details about the data acquisition in chapter [3]

Figure 2.3: Encoder mounted on its base before being fixed on the final setup.
In detail the encoder sensor is fixed on the "9202" [6] mounting bracket, the black component is the 3D printed "C3 - Encoder Base".

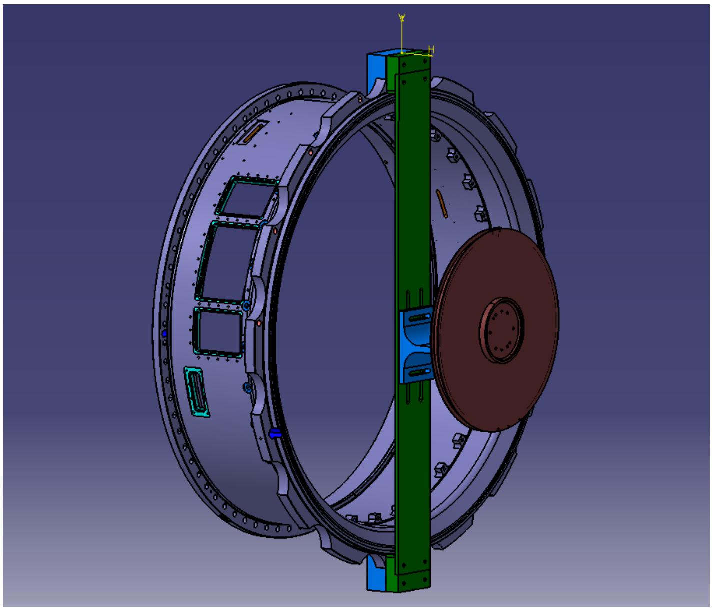

Figure 2.4: CAD model of the encoder support system for the 2024 "Inertia Measurements on CT3" experimental setup

2.3 Encoder's Support System Design

The first task of the project is to design a 3D model for a new support system for the encoder: the only requirements of this design were:

1. Stability for the encoder during the measurements.
2. Availability to easily mount and dismount the encoder support setup to be used even later for other projects on the CT3 facility.
3. Availability to mount the encoder accordingly to the rotor's axis.

On the software CATIA V5 a new assembly is created considering the statoric case of the CT3 as a stable support for the setup as well as a reference point.
After a few design reviews and modifications the final assembly (shown in figures [2.4] and [2.5]) is made of the following main components (table [2.1]). For the initial setup validation, a wooden slab has been used as a substitute for the aluminum slab (which was still in manufacturing), along with a scaled-down 3D-printed version of the traction disk.
These temporary components are used to verify the data acquisition process and immediate post-processing feedback system.

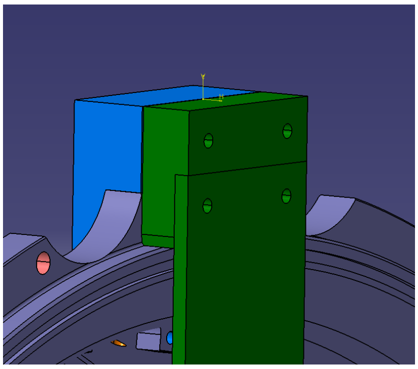

(a) *Case - Clamps Connection Detail*

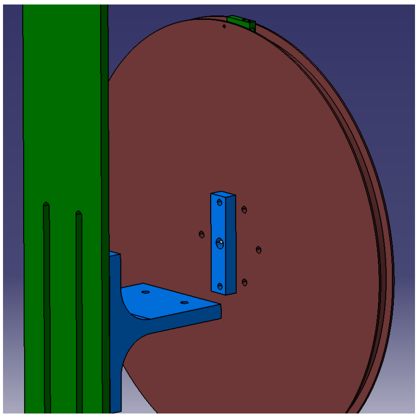

(b) *Torque Disk Detail*

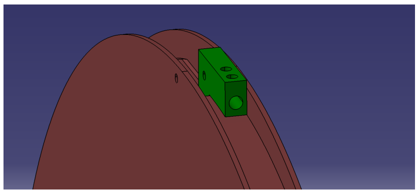

(c) *Torque Hook Detail*

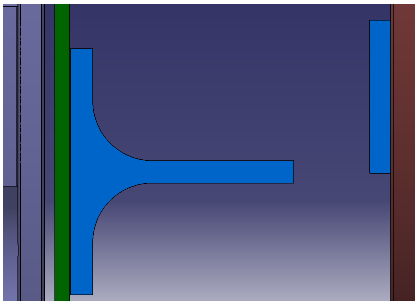

(d) *Encoder Base Detail*

Figure 2.5: CAD model details of the experimental setup

N°	**Part Name**	**Part Name (In Product)**	**Manifacture**
Product	Product 5.0 Design V2		
C 1	5.3 Clamp Curvature	Clamp Curvature V2.5	3D Printed
C 1.1	5.3 Clamp	Clamp V2.5	3D Printed
C 2.1 | C2.2	5.3 Product Arm	Clamp V2 |Slab V2.5	(Manif./3D Printed)
C 3	5.3 Base Encoder	Encoder Base V2.5	3D Printed
C 3.1	4.4 Support L	Support L V1	Purchased
C 4	5.3 Product Disk Rotor	Product Disk - Rotor V2.5	
C 4.1	5.3 Rotor Disk	Disk s=20mm V2.5	(Manif.)
C4.2	5.3 Hook V2.5	Hook V2.5	(Manif.)
C 4.3	Rotor Disk Interface	TUR1902-029 Bouchon Arbre.1	CT3 Facility
C 5	Statoric Case	TUR1902-011 Boitier Externe.1	CT3 Facility

Table 2.1: List of the components designed by the candidate using CATIA V5 for the new experimental setup.

$N°$	**Part Name**	**Requirements**
1	Incremental Encoder DHM510 Setup	16 bits resolution, TTL signal
2	CAD Experimental Parts (Table:[2.1])	Stability during the measurements
3	6x PVC covered steel wires	Non elastic wire for rotor-mass connection
4	Calibrated Mass (5kg) (Option B)	Creates the acceleration by free fall
5	Fixated Pulley System	Lowest friction possible, U shape
6	Precision Measuring Scale (Option A)	Precision of at least 1g
7	Main Screw Connections:	
7.1	Clamp-Arm Screw Connections	4+4x M8, lengh of at least 120mm and 25 mm
7.2	Arm-Encoder Base Connection	4x M8, length of at least 40mm
7.3	Encoder Base- L Support Connection	2x M6, length of at least 40mm
7.4	Rotor Encoder Connection	2x M5, length max of 40mm
7.5	Rotor Disk Connection	6x M6, length of at least 40mm

Table 2.2: List of purchased and available components for the new experimental setup

2.4 Single Components Requirements

2.4.1 C1.1 & C2.1 Clamps Design Requirements:

The clamps are designed to support the entire encoder's support structure by applying pressure to the external part of the statoric case.
The external casing ("boîtier")[3] has a "toothed" profile, which the clamps utilize to grip the teeth aligned along the vertical axis, as shown in figure [2.6]. The clamps are positioned on both the external and internal sides of each tooth and are secured to the case using two M8 screws, ensuring a stable and motionless encoder support setup. The two external clamps (C 2.1 components) also provide a stable connection to component C2.2 (the slab) through additional M8 screw-nut connections.
In the following images (figure 2.6) the clamps components CAD design are shown in detail:

[3]This was the name of the statoric case in the CAD CT3 facility's assembly the candidate had the opportunity to work on.

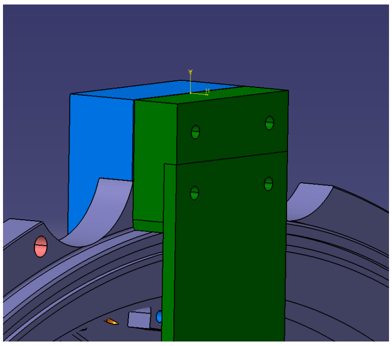

(a) *Case - Clamps Connection CAD Detail (Frontal View)*

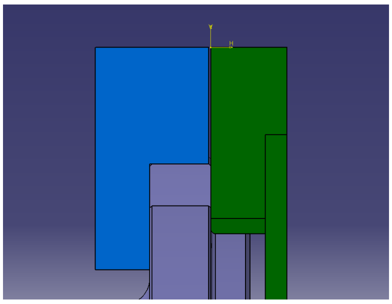

(b) *Case - Clamps Connection CAD Detail (Lateral View)*

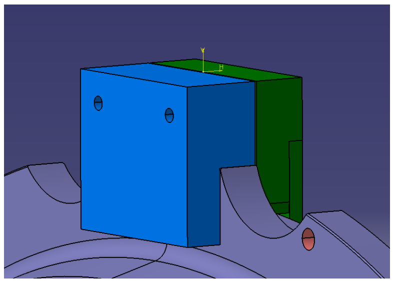

(c) *Case - Clamps Connection CAD Detail (Rear View)*

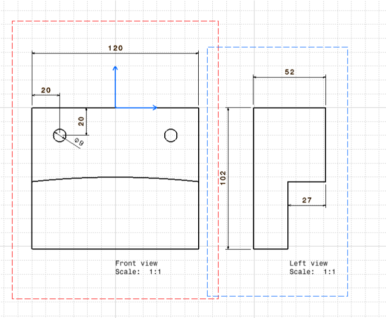

(d) *External Clamps Drawing [C1.1]]*

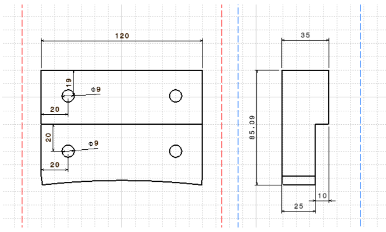

(e) *Internal Clamps Drawing [C2.1]*

Figure 2.6: CAD model details of the clamps C1 & C2.1 design.

As shown in image (b), the connection to the "boîtier" (the grey component, which is the stator casing) is ensured by applying pressure on both sides of the "tooth" shape using the blue and green components (C1 and C2.1, respectively).

To ensure that pressure is applied to the boîtier and not between the clamps, the components were designed to maintain a 1 mm gap between the clamps themselves.

The clamp components were also given a curvature to fit perfectly the shape they are designed to lay on, this add-on is included to increase the stability of the setup and improve precision during mounting operations.

2.4.2 C2.2 Slab Design Requirements

The slab component C2.2 has the key requirement to ensure a stable and modular connection with the "encoder base" component C3.
The slab is designed to connect to the two clamps C2.1 using four M8 screw-nut connections. This component must remain still and stable during testing to acquire data with minimal side effects, such as vibrations.
In the center of this slab, which was later manufactured by the VKI's internal workshop in aluminum, there are two large slots.
These slots enable the slab to be paired with component C3 in slightly different positions, allowing the encoder's axis to be fixed to the rotor's axis as precisely as possible.

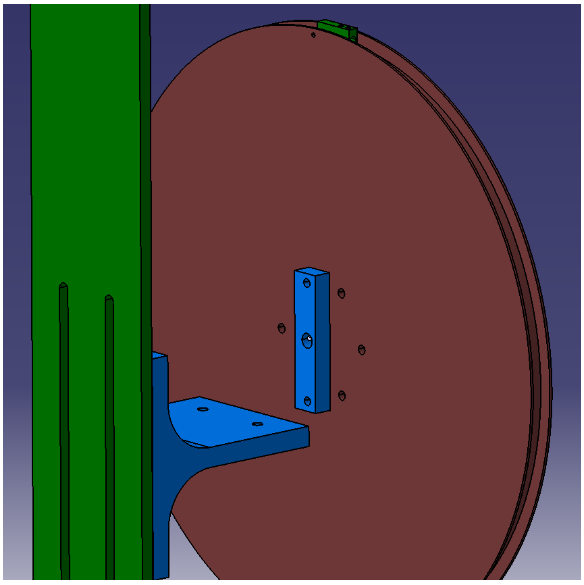

(a) *Slab Component Rear View*

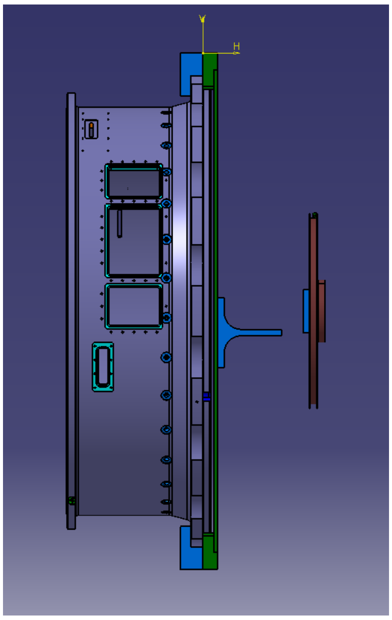

(b) *Lateral View of the slab and its connection*

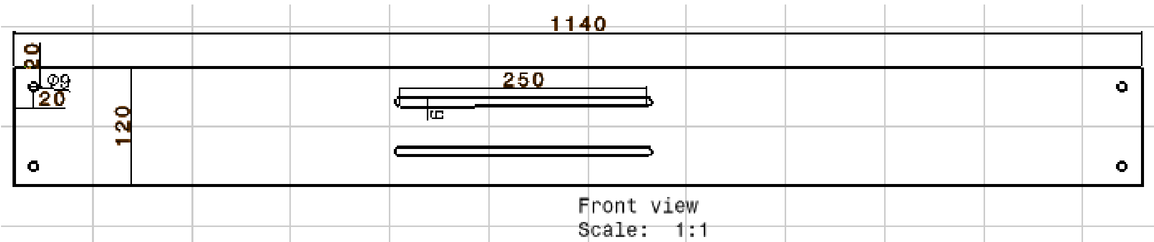

(c) *CAD Design of the Slab*

Figure 2.7: As shown in image (b), the connection to the boîtier" (the grey component, which is the stator casing) is ensured by applying pressure on both sides of the tooth" shape using the blue (C1) and green (C2.1) clamp components.
To ensure that the pressure is applied to the boîtier and not between the clamps, the components are designed to maintain a 1 mm gap between the clamps themselves. Additionally, the clamp components are given a curvature to fit perfectly the shape they are designed to lay on. This feature is included to increase the stability of the setup as well as improving precision during the mounting operations.

2.4.3 C3 Encoder Base Requirements

The encoder base component (C3) is strictly designed to hold the weight of the encoder device and maintain it in position on the same axis as the rotor's disk (component C4.1).
Similar to the slab C2.2, the encoder base has two slots designed on it to generate multiple coupling options on the x-y plane.[4]
The length of the base [20 cm] is chosen in order to move the point of contact between the encoder and the disk away from a vertical blue tube positioned on the right side of the facility. This conflict would have been a problem for the correct, unobstructed displacement of the wire during the tests.
It is a requirement to keep enough space between the rotor's disk C4.1 component's position along the facility's axis and the tube itself.
In brief, the base must be designed with a sufficient length to keep the encoder to the left of the projection of the tube over the facility's axis (for reference, see image 2.8 (d)). The length chosen for the C3 component creates more than sufficient space (on the left of the blue tube shown in the image [2.8(d)]) to safely operate the tests avoiding any possible contact between the moving wire and the tube[5].
In the same order of the encoder it has been included an "L" support system in which two M6 screw-nut connections can be used to fixate safely both the structural components on the [C3] component's base and the encoder itself will be perfectly vertical and stable; see the figure [2.9] for all the details.

2.4.4 C4.1 Rotor Disk Requirements

The rotor disk is designed to host the wires selected to conduct the experiments (see subsection [2.4.5] for more details) for at least five rounds.
The disk is designed after choosing a reference radius to generate the torque during the acceleration phase.
During the experimental campaign conducted by the candidate's supervisor Lorenzo Da Valle in 2023, the wire used was revolved around some M4 screws mounted on the rotor at a radius of approximately R=220 mm. The new requirement for the 2024 experimental project is to create a new "wire hosting" and torque pivot component as a cylinder with the following dimensions:

	External Radius	Guide Radius	Torque Radius	Width	Material	Weight
Symbol	R_e	R_g	R_t	s	Al	W
Value	$230mm$	$220mm$	$2215mm$	$20mm$	Aluminium	$8.33kg$

Table 2.3: C4 Disk Product Properties

A few designs have been processed and later checked with the VKI's supervisors, especially for the critical point of the disk (component C4.1): the connection between the disk itself and the wire possibly using a removable hook (component C4.2). In the previously cited experimental campaign, one of the systematic problems was generated by the wire readjusting itself on the rotor during the deceleration phase of the tests.
The operators needed to be careful during this phase to avoid generating tension on the wire,

[4] This option is chosen to avoid any problems in axis alignment between the encoder setup components and the rotating parts.

[5] Needless to say that a contact between these components would have had a huge impact on the uncertainty of the Inertia's measurements due to the wire vibrations caused by the hypothetical brief contacts with the tube, as well as increased friction effects that would invalidate the test's results

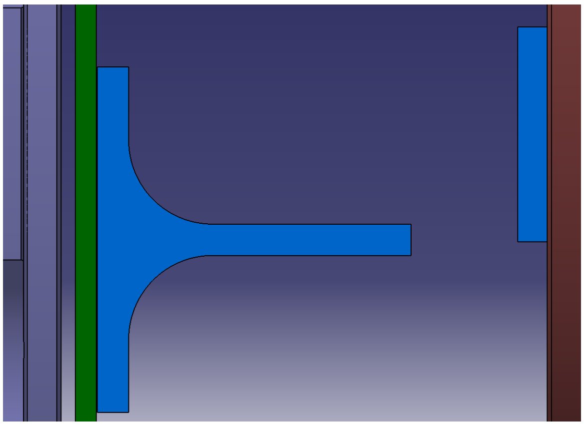

(a) *Encoder base component lateral view*

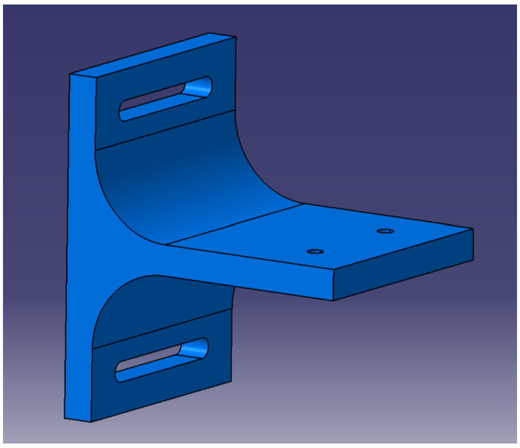

(b) *Overall view of the encoder base*

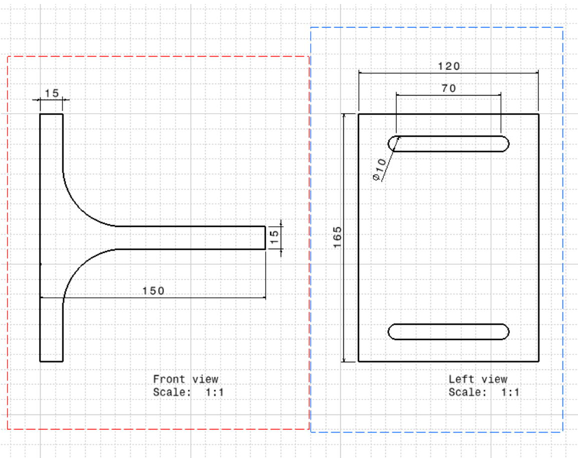

(c) *Technical Drawing of the C3 component*

(d) *Detail of the blue tube on the right side of the facility, from this perspective it is clear that the encoder base had to be designed accordingly to avoid any conflicts of the wire moving during the tests.*

Figure 2.8: CAD model details of the encoder base C3.

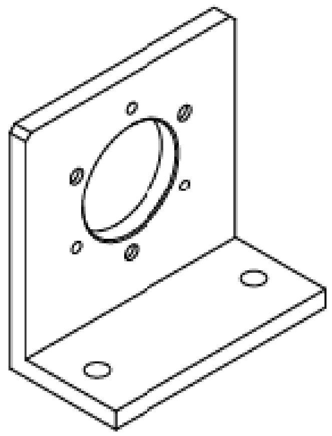

(a) *L shape structural component (serial number "9202") to fix the encoder on the base.*

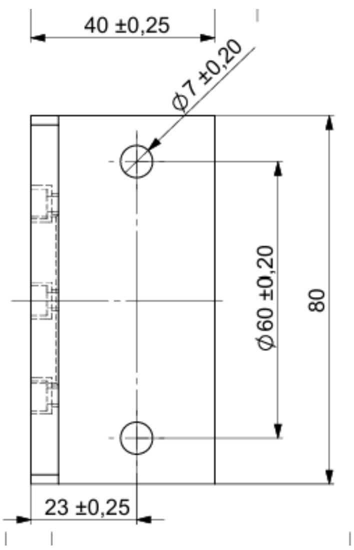

(b) *Detail of the holes (D=7mm) for the M6 screw connection between the "9202 L shape support" and the [C3] component.*

Figure 2.9: Preview and CAD model details of the "9202 L shape support" [6] used for the encoder fixing.

in order to protect the tests from useless noise and keep both the measurements and the equipment itself (i.e., the encoder, especially being fragile) as intact as possible.
To overcome this critical point it is pursued an option for a removable hook C4.2 able to detach automatically from the rotor at the start of the deceleration phase, avoiding all wire re-attachment conflicts.
This option is based on the shape of the hook, adapting itself to the guide's curvature and applying torque on the radial surface of the disk, as shown in image [2.11]. As an option A, the hook is designed to stay still and attached to the disk's surface, generating torque as long as sufficient tension is applied to it.
However, during the preliminary tests, it becomes clear that this option is not very stable.[6]
This option is then discarded as insufficient pressure can be applied to the hook during the acceleration phase, generating problems in concluding a valid test as well as taking a lot of time to readjust the hook on the disk between each test. A second option is chosen, which is much more reliable in terms of ensuring the tension and torque generation from the hook to the disk. However, the candidate has to deal with the problem of the wire re-adjusting itself over the disk.
The solution to this critical point is to adjust the wire accordingly on the disk in order to obtain a simple displacement and no re-adjustment during the deceleration phase.
This process is successfully done by fixing the hook in a stable position, secured by an M3 screw-nut connection.[7].

[6]The preliminary tests are conducted between August and October 2024 to see especially if the entire data acquisition setup is working properly and also to obtain the first partial results by testing the codes on MATLAB. These first tests are conducted on temporary 3D printed components like the C4.1 disk scaled to an external radius of $R_e = 10mm$ while the candidate is waiting for the conclusion of the manufacturing process of the final and correct aluminium parts C2.2 and C4.1.

[7]This add-on fixes the unstable de-attachment problem of the hook.

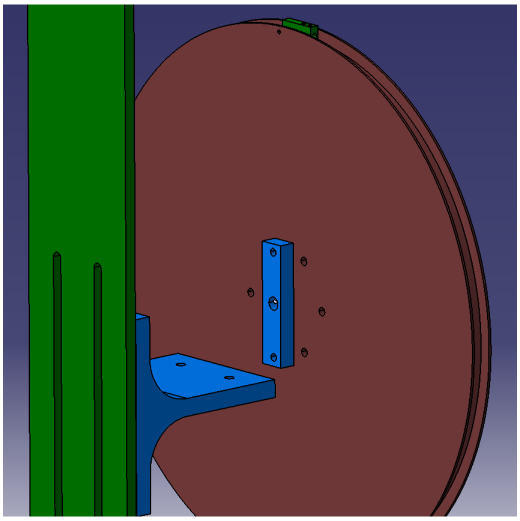

(a) *Torque disk component [4.1] overview*

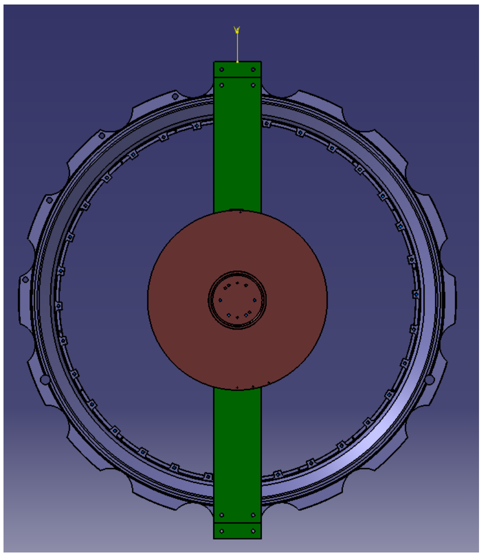

(b) *Frontal view of the setup, the rotor's disk is the brown large cylinder.*

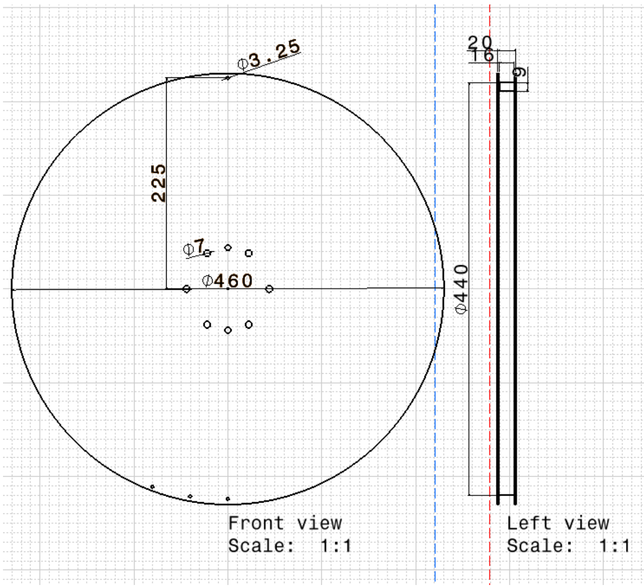

(c) *Torque disk component [4.1]technical drawing*

Figure 2.10: Torque Disk [C4.1]; connected with 6 M6 screws to the rotor itself, it ensures both the encoder connection and the correct torque input by the tensioned wire, as well as its correct displacement during the tests.

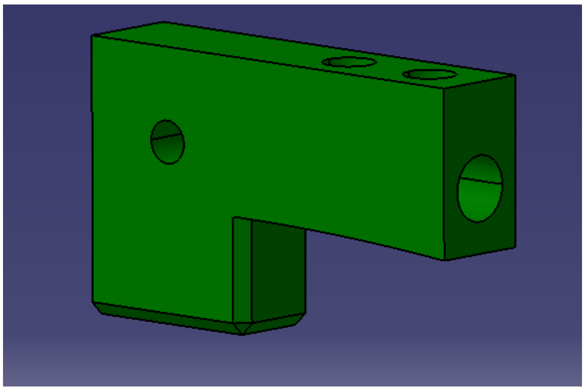

(a) *Overview of the final hook component [C4.2]*

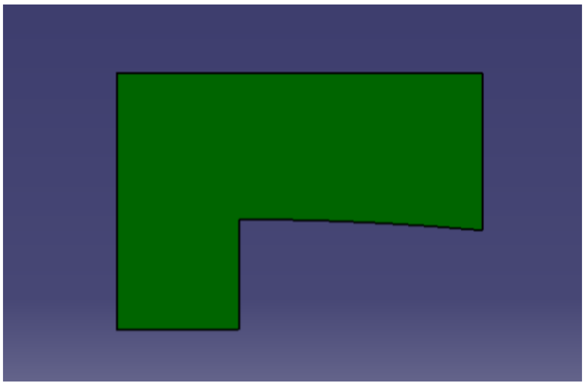

(b) *Lateral view of the hook*

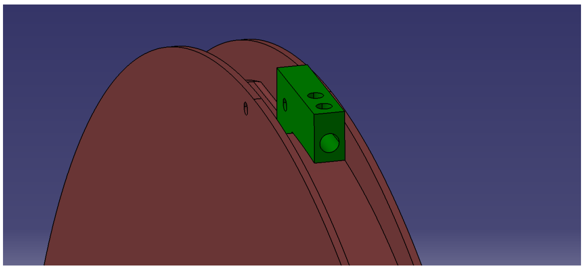

(c) *Hook mounting on the torque disk [C4.1]*

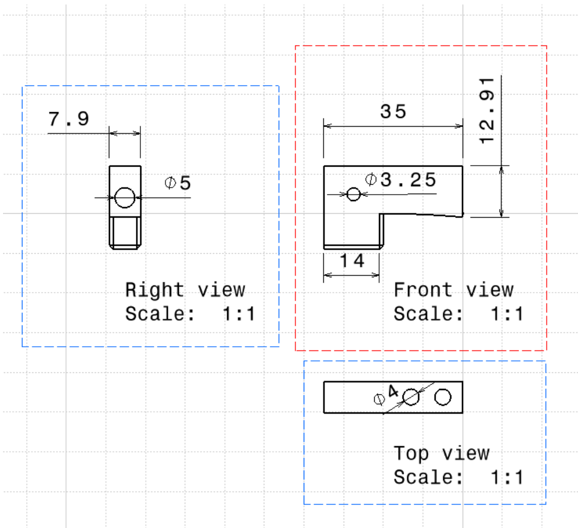

(d) *Hook technical drawing*

Figure 2.11: CAD model details of the final version chosen for the hook [4.2]

At the same time, extra rotations[8] of the wire over the disk's guide are given to avoid the problem of the wire re-attaching itself to the disk's guide, or worse, getting off the disk guide and generating conflicts on the encoder-disk connection.[9]
The last design chosen for the project is shown in the figure 2.10, including the "Hook" component [C 4.2].
This part is designed many times, as well as the [C4.1] disk, to be adjusted both in shape and dimensions, in particular for the last few test sessions the pivot part of the hook[10] has been removed in order to generate the torque exactly at the designed radius R=0.2215m.

2.4.5 Wire Requirements

The wires need to be chosen considering two requirements: sufficient flexibility to be curved, but also guaranteed "stiffness" under axial tension, in order to obtain valid tests without other variables caused by a more "elastic" cable.
Two wires are chosen and purchased from the website *"www.drahtseile24.de"*[12]: two different widths are chosen (D=3mm and D=4mm) and six wires in total have been purchased (2x D=4mm % 4x D=3mm).
Available in 3mm and 4mm diameters, this wire combines the strength of steel with the protective properties of PVC coating, making it suitable for both indoor and outdoor use.
At the core of the D=3mm product's design is its 7x7 structure, a configuration that significantly enhances its performance characteristics.
The term "7x7" refers to the wire's construction, consisting of seven strands, each made up of seven individual wires.
This arrangement provides an optimal balance between flexibility and strength, allowing the wire to maintain its integrity under various stress conditions, which is the main reason this product has been chosen.

(a) *Overview of the wire*

(b) *Detail of the 7x7 structure*

Figure 2.12

[8]Seven or eight extra rotations are given on the temporary 3D printed scaled disk used during the preliminary tests while on the final disk only five are needed

[9]The encoder, being arguably expensive and most importantly fragile has to be secured, so the candidate during the preliminary phase has designed and 3D printed some extra safety measures to protect the sensor from an undesired free-moving wire along the facility axis and out of its designed trajectory.

[10]The vertical "L shape" of the hook has been removed; the last version of the hook resembles an "I" shape keeping only the horizontal design shown in figure 2.11 including the curvature to perfectly fit on the disk C4.1

Bearing Type	Radial Load	Axial Load	Speed	Friction
Deep Groove Ball	High	Moderate	High	Low
Angular Contact Ball	High	High	High	Low
Cylindrical Roller	Very High	Low	High	Low
Tapered Roller	Very High	High	Moderate	Moderate
Needle Roller	High	Low	High	Low
Spherical Roller	Very High	Moderate	Moderate	Moderate

Table 2.4: Comparison of bearing types and their properties

The 7x7 structure increases the wire's flexibility compared to more rigid constructions, making it easier to work with in this project's application that requires bending or being curved.
Secondly, this configuration distributes tension more evenly across the wire's cross-section, enhancing its overall load-bearing capacity.
Lastly, the multiple strands provide redundancy, meaning that if one wire fails, the others can continue to bear the load, improving the product's safety and reliability.
The PVC coating adds another layer of functionality to the steel wire, it also provides protection against corrosion, extending the wire's lifespan in harsh environments and minimizing the damage caused by the friction between the components like the pulley or the disk in the present setup.

2.4.6 Pulley Requirements

The pulley is a key component of the selection and purchasing phase: the most important requirement is selecting a wheel that provides the least amount of friction possible during its use.
The second requirement is to avoid any relative displacement between the pulley's wheel and the wire during the operations; this second request is satisfied by selecting a fairly large pulley to maximize the contact surface between the wire and the pulley's guide.
In order to obtain the least amount of friction for the pulley, several options of bearings are taken into consideration.
Bearings are crucial components in mechanical systems, designed to reduce friction between moving parts and support loads; in pulley applications, the choice of bearing type significantly impacts system performance, efficiency, and longevity.
A brief comparison table is shown below to see how the "deep groove ball bearing" type is the best choice for this specific pulley application. Deep groove ball bearings are a type of ball bearing characterized by deep, uninterrupted raceway grooves, they are particularly well-suited for pulley applications due to their excellent performance under radial loads.
In this application, axial loads are very low as the wire tensioned from the rotor to the pulley is well-aligned, this is mainly due to the rigorous precision during the assembling phase, obtained with the help of the Turbomachinery's laboratory head technician Louis Duculot, who helped the candidate during his internship in several ways regarding laboratory work and provided technical expertise and precious suggestions during the assembling phase of the experimental setupas well as during the actual testing phase.
That being said, only the radial load can be considered in this specific case, although the mass attached to the wire is significant, it generates a significantly lower radial load compared to the maximum capacity of the product chosen. Deep groove ball bearings offer significantly lower friction compared to other bearing type due to the minimal contact area between the balls and

Figure 2.13: Deep groove ball bearing example.

(a) *Overview of the new pulley*

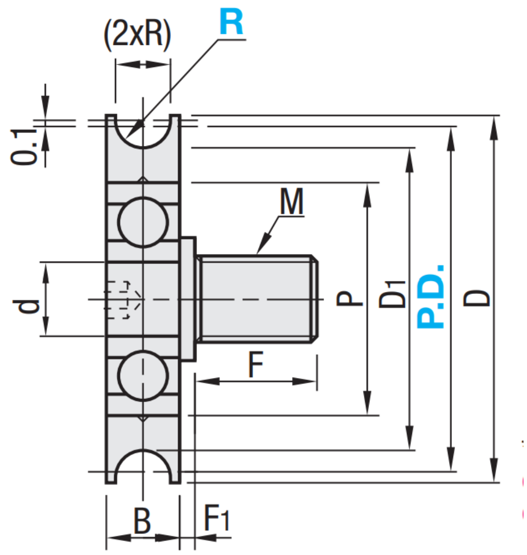

(b) *Technical drawing of the the pulley*

Figure 2.14: Misumi MBFNS100-3.1 pulley

the raceways, resulting in reduced rolling resistance.
While they can handle some axial loads, deep groove ball bearings excel at managing radial loads, which are predominant in pulley systems and makes an excellent match for our project's specific application.
These bearings typically require less maintenance than other types due to their sealed or shielded designs, which protect against contaminants and retain lubricant.

After a careful evaluation of many possible options, the final choice for the pulley is the "MISUMI MBFNS100-3.1"; this pulley incorporates deep groove ball bearings, leveraging all the advantages discussed above.
With a 100 mm outer diameter, this pulley also satisfies the second requirement[11]. This product satisfies both the principal requirements, and it also includes an M10 connection that is perfect for the setup already mounted on the ceiling of the VKI.
To connect the new pulley to the old setup, an M10 coupling is purchased from "RS Compo-

[11] maximizing the contact surface between the wire-pulley

(a) *Example of the M10 coupling to secure the new pulley to the old setup already of the VKI*

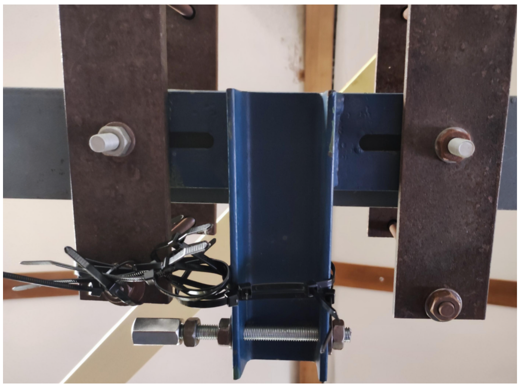

(b) *Old setup in the VKI with the coupling included*

Figure 2.15: M10 coupling concept to fix the pulley on the ceiling.

nents"[3] (see image 2.15).

2.4.7 Measuring scale requirements

The measuring scale is an important tool to determine, within a precision of 1g, how much weight is being put in the bucket to generate the necessary torque to accelerate the rotor.
The reason why a more precise measuring scale is not necessary is due to the specific weight of the uncertainty due to the mass (see appendix [A] for reference).
In brief, achieving a precision equal to or higher than 0.1g is pointless, as it would result in essentially the same uncertainty for single measurements on the overall inertia value.
An additional reason for not purchasing a more precise measuring scale is simply the cost increase - more than double the price of the actual chosen product. The purchased product is "Waagenet GRAM AC"[5], with a load capacity of 5kg and a precision of 1g, as it matches not only the technical requirements but is also a budget-friendly option.
A second option is considered during the preliminary design phase of the experimental setup: using calibrated weights instead of purchasing a measuring scale and using the material already present at the VKI.
This option is discarded due to high budget demands for the products as well as more limited options in terms of choosing the weights to conduct the tests with.

2.4.8 Bucket and weight

The last components are the actual weight and a bucket to contain it: the bucket is a simple metal product, wide and high enough, as well as sufficiently resistant to host a maximum weight of approximately 15 kg and preserve its shape and structural integrity during and after many tests (see the product for reference [7]).
Thanks to the location of the test, the material already present in the laboratory[12] is measured

[12] In the laboratory several large screws were available: M16 and M18 screws each weighing between 200g and 400g have been used in this project

(a) *The bucket used for generating the torque and its weight, M16 and M18 screws are used to generate the force necessary to move the rotor assembly.*

(b) *Measuring scale GRAM AC*

Figure 2.16

and put in the bucket to achieve different weights and conduct several tests to observe the differences in the results.
Given the high amount of screw types and overall number, any weight between 3 to 15 kg can be obtained, generating an easily accessible and precise weight variation for each testing session.

2.5 Final Experimental Setup

In the following images it is reported the overview and details of the final experimental setup. The final setup is more stable due to the right proportions of the disk not allowing the wire to get off the guides during the deceleration phase; as well as the accurate positioning of the encoder axis is now possible all over the plane created by the slab surface.

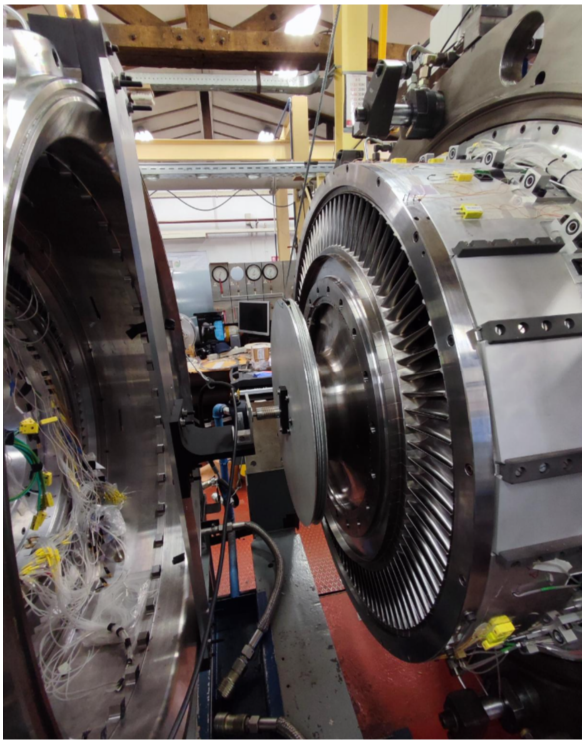

(a) *Overview of the new experimental setup*

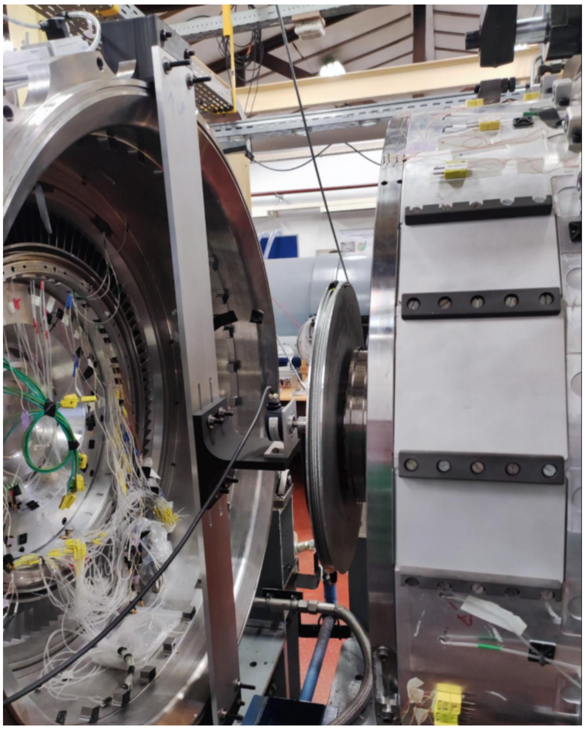

(b) *Overview of the new experimental setup*

Figure 2.17: Overview of the final experimental setup, new aluminum torque disk and slab are used.

(a) *Overview of the final aluminium disk.*

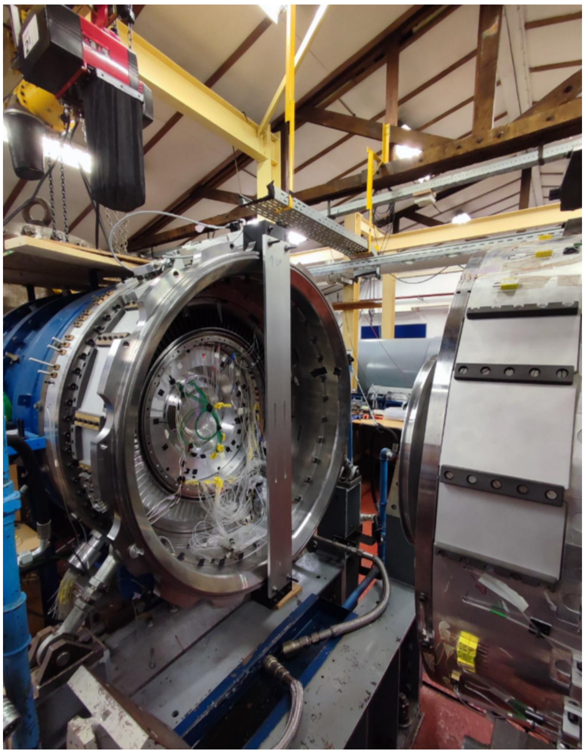

(b) *Overview of the final aluminum slab*

Figure 2.18: Overview of the final experimental setup, new aluminum torque disk and slab are used.

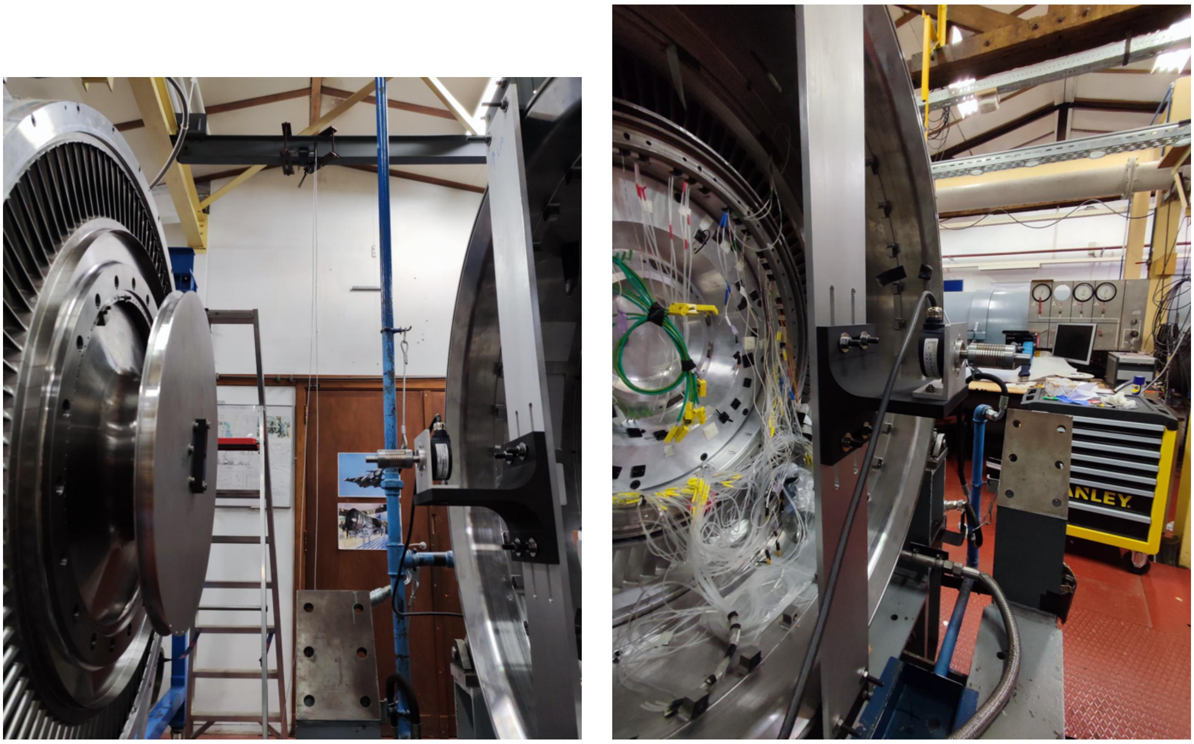

(a) *Overview of the new experimental setup before fixing the encoder to the disk assembly.*

(b) *Detail of the encoder mounted on its base, with emphasis on the flexible coupling. This component is key as the minor eccentricity on the real setup is nullified by it, allowing the testing sessions to proceed without any issues.*

Figure 2.19: Detail of the encoder base connection

2.6 3D Pritinting Process Details

To obtain the components necessary to complete the experimental setup it was used the printer "Prusa MK4"[11] by Joseph Prusa shwn in the figure [2.20].
The Prusa MK4 3D printer is the latest 2024 iteration from Prusa Research, a company that has established itself as one of the most trusted and innovative names in the field of desktop 3D printing; this version offers a building volume of 250x210x220mm, allowing users to print small detailed models and also large components.

(a) (b)

Figure 2.20: Images of the "Prusa MK4" 3D printer available in the Turbomachinery Department Laboratory facility at the Von Karman Institute

One of the most significant pros of this product is its modular design: the Prusa brand is well known to add extra components or upgrade the 3D printer setup very easily[13].
This printer, due to its stable frame can handle high-speed printing while mantaining a high degree of precision and low risk of inaccuracier or general vibrations that could compromise the final product; there are two printing speeds available: "Stealth Mode", slower but more silent and "Speed Mode" which is a little bit noisy but fast and effective at the same time.
For all the components printed for this project it was always used the "Speed Mode" as it was the most efficient and time-saving option.
By using the software "Prusa Slicer"[10] it is possible to change many options and filament properties to customize every printing session depending on the final product requirements: the Prusa "MK4" allows the sure even to change the nozzle [14], it can also change the "infill" parameter [15].
This parameter determines how much of the interior part of the component is filled with material and it is defined by a percentage: increasing this infil percentage for example o 50% means obtaining a solid object (a structural component is an option in this case), on the other hand decreasing this value will generate a lighter object with less internal support.

[13] As an add on the version used in the VKI was included with the tool "Multi-Material-Unit", able to change color or type of filament during the printing process if allowed to.

[14] Options available: diameter 0.4mm, or 0.2mm to enlarge or reduce the filament's size while printing, this feature can increase or reduce the precision for bigger or smaller pieces, depending on the tolerance required for example to obtain finely detailed objects.

[15] The definition of the infill in the context 3D printing is the internal structure of a printed object. It is the material used to fill the interior of a 3D print, sitting between the outer walls (perimeters) of the model. Infill provides structural support, enhances the strength and durability of the object, and affects its weight and material usage.

Another important parameter is the "pattern" [16]; during the internship all of the components where structural so they required a strong pattern and a high infill percentage; the options chosen for all of them were the "cubic" pattern and the infil percantage of "30%", this value was chosen to have a high enough structural resistance as well as not utilizing too much material Due to its high versatility many shapes ould be created with high precision as well as different materials could be used.
In this case the material chosen was "ecoPLA-Black" from the supplier "3D Jack"[1], this particular material is obtained from renewable resources as corn starch or sugarcane; with a density of approximately $1.24\frac{g}{cm^3}$ it can generate objects with high tensile strength and hardness.
Its use is suited for structural components but at the same time under an excessive stress it is prone to cracking or snapping under bending stress; it is clear that using this rigid material will generate 3D printed objects with extremely low flexibility properties.
Compared to other filament's materials used by 3D printers like PETG, ABS or others, the PLA is one of the easiest options to deal with: the filament results in smooth print with low probability of defects during the process; it is also very unlikely for this material to warp [17].

[16]The pattern of the infill is simply the shape chosen for the inner structural part of the 3D printed objects; choosing one pattern instead of another is due to obtaining different levels of strength or simply printing speed.

[17]In 3D printing this term is used when layers of extruded filament on the 3D printer build plate cool too quickly and shrink.
This causes the plastic material to contract and pull away from the build plate, resulting in warping (or curling, as it is sometimes known).

Chapter 3

Data Acquisition and Post Processing Logic Overview

In this chapter it is shown how the experiments are conducted, what hardware and software can detect the data form the encoder and finally how this signal is post-processed to get the results.

3.1 Data Acquisition Setup Overview

The data acquisition hardware is positioned on the let side of the statoric case as shown in figure [3.1].
From the right to the left we can see the PC on witch there is installed the software "Perception" available to read the and translate the data gathered from the encoder to a TTL signal, the Genesis Data Acquisition System connected to the encoder is connected both to the PC via an Ethernet cable to translate the data to the software "Perception" and the encoder, this device collects the angular data from the moving rotor and sends it back to the "Genesis Tower". During the first part of the intership the candidate has selected an encoder capable to be coupled with the "Genesis Tower" by a BNC cable connection[1]; after this selection the whole setup has been mounted near the CT3 facility and all the hardware devices have been connected to the electricity.
Between August and the first half of October preliminary tests have been conducted by the candidate using a temporary setup: this necessity has generated due to the times required to manufacture two of the final setup components as already cited before; however the point of the preliminary tests is to check the correct operativeness of all the hardware and software devices. Thanks to this period of experiencing the real conditions of the experimental setup a few modifications have been applied, such as the add-on of the extra guides for the pulley: these guides have been designed on CATIA V5 and later printed and fixed on the pulley to prevent the wire form falling outside especially during the deceleration phases of the tests, when vibrations and the lack of tension for the wire have generated more uncertainty.

[1]BNC (Bayonet Neill-Concelman) is a type of RF connector commonly used in low-power signal and video applications. It features a quick-connect/disconnect bayonet mechanism and is known for its robust connection. In data acquisition systems like Genesis, BNC connectors are often used to transmit analog signals from sensors such as encoders. The coaxial design of BNC cables helps maintain signal integrity by shielding against electromagnetic interference, making them suitable for precise measurements in industrial and scientific applications.

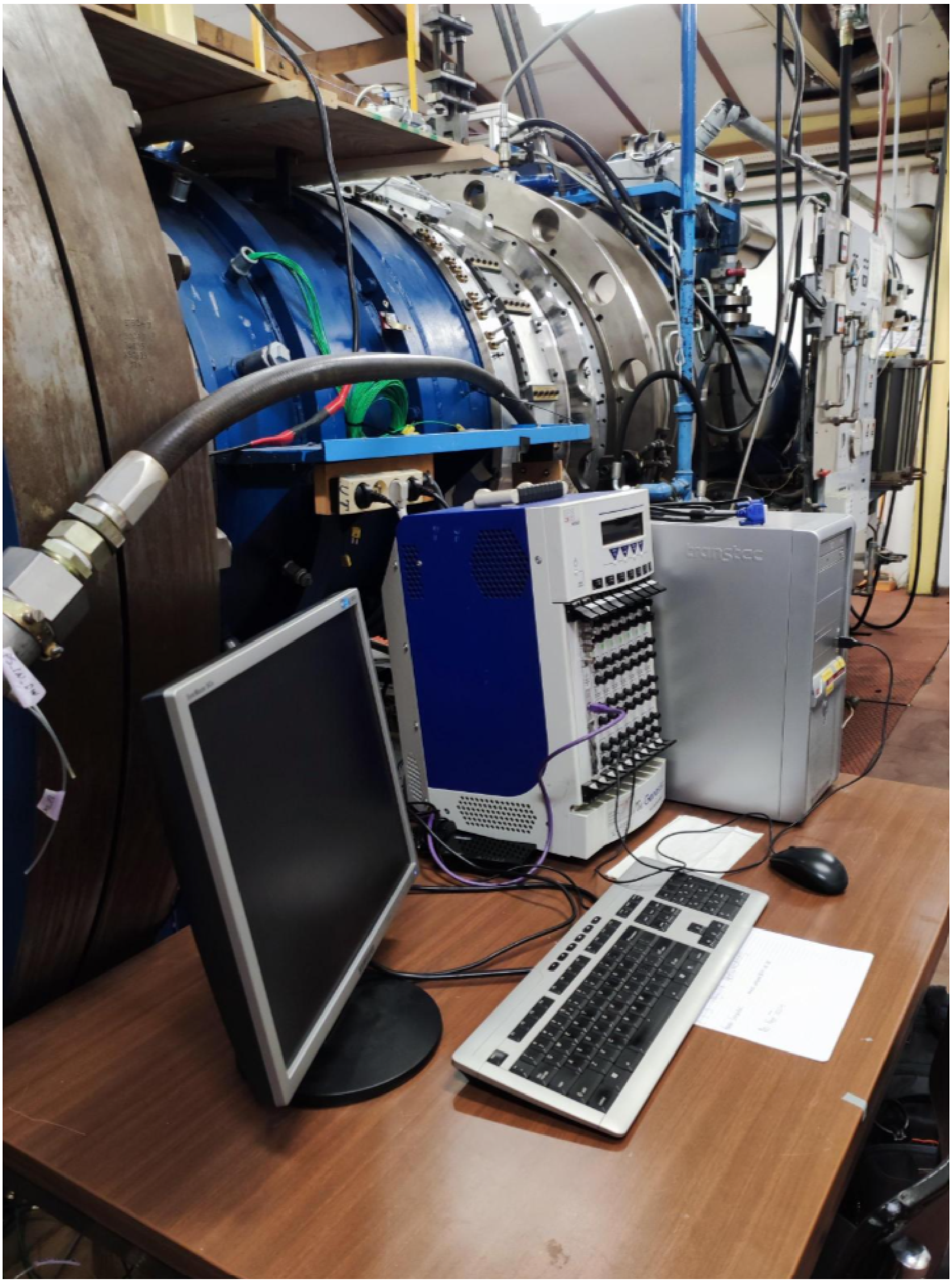

Figure 3.1: Detail of the data acquisition setup and the CT3 facility in the background. From the left to the right: Pc monitor, Genesis Tower, PC "Tuttec13".

3.2 Testing Session Procedure

In this section it is reported the checklist procedure concluded before and during every test.

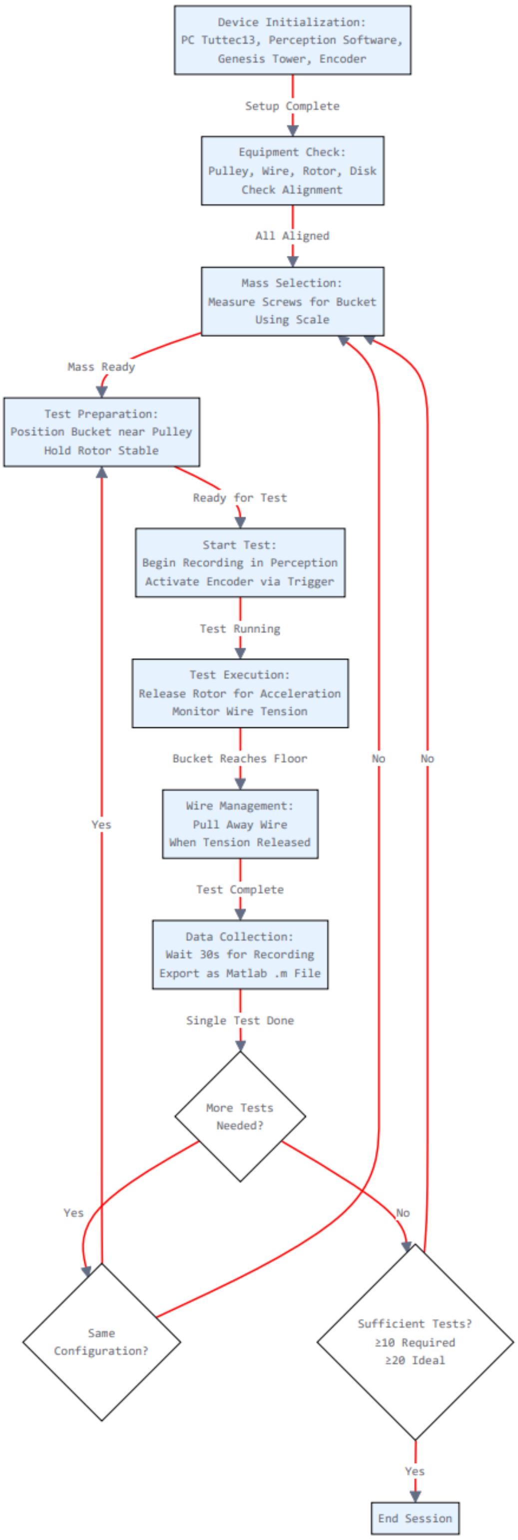

Figure 3.2: Test session procedure schematic flow chart.

1. The first step is switching on all the devices and check if they are working correctly. This includes the log-in to the PC ”Tuttec13” present in the VKI Turbomachinery labo-

ratory, opening the software "Perception" with the saved workbench ready for the test, and switching on the "Genesis Tower" and the encoder.

2. The second step is to check if the pulley, the wire, the rotor and the disk are presenting some misalignment or any other issue like the wire being slightly outside form the pulley guide.
3. The third step is to choose the mass to put in the bucket in order to begin the testing session; to reduce any uncertainty due to selection of the mass, the measurements of the screws put in the bucket are conducted frequently by using the measuring scale "Waagenet GRAM AC"[5].
4. After carefully checking all this checklist the testing session can begin: by pulling the rotor manually the bucket is put into the engage position as close as possible to the pulley, then someone has to keep the rotor still to hold the bucket in the most stable position achievable.
5. The test begins when the recording has started on the software perception and the encoder has been activated by the "Trigger"[2] button, only after this procedure the rotor is set free by the tester and allowed to be accelerated by the mass pulled down by the gravity force.
   During this phase the wire is tensioned so there are never issues of unwanted vibrations or oscillations of the wire, on the other end when the bucket has reached the floor the candidate has to be reactive and pull away the wire that is still moving due to the rotor but it is not under tension anymore[3].

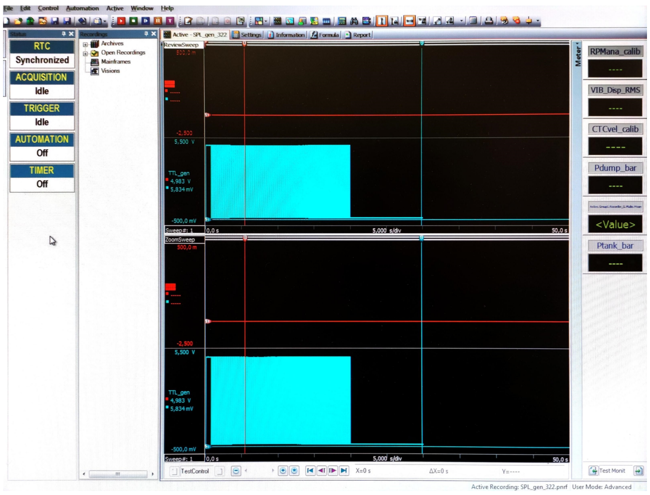

Figure 3.3: Screenshot of the preview of the software "Perception" after a data acquisition from the encoder

6. When the deceleration phase ends the candidate waits for the recording to be automati-

[2]The procedure starts by activating the encoder, by clicking on the red button "Play" on the high-left side of the command window in the image [3.3, then the purple trigger button "T" is clicked, its status will show "Armed" (instead of "idle") and the encoder will actively start recording the rotor's angular displacement for thirty seconds.

[3]Choosing to manually "pull away" the wire during this deceleration nphase would generate un-repeatibility conditions in every test, this is why this procedure is key to achieve uniform experimental conditions test after test.
For example the un-tensioned wire could fall from the pulley due to vibrations, another frequent example would be the un-wanted torsion of the un-tensioned wire on itself, possibly diturbing the correct acquisition of the encoder's data due to vibrations and extra friction on the setup caused by the wire chaotic trajectory.
As it can be easily imagined by the reader these events must be avoided to obtain good quality measurements for each session.

cally concluded thirty seconds after clicking on the "Trigger" button.
When the system is ready, on the software perception's display it is shown this raw TTL signal (see figure [3.3]). the data is then exported to be saved on the PC as a Matlab ".m" file and copied on a pen-drive in order to be ready for the post-processing phase.

7. A single test ends with the previous step; without changing any variable multiple test can be repeated by beginning from step n° 4.
8. To generate sufficient data for each testing session a number of at least ten tests have to be completed; for better statistical results concluding twenty different tests for each session is ideal.

3.2.1 Wire Torsion Issue

A considerable number of tests has been discarded and the procedure has been repeated more times in order to address this issue: the wires used, despite meeting all the preliminary requirements cited in section [2.4.5], have often been observed with small initial bumps on some points of their surface (even before use) and more importantly after a few tests (from 15 to 30 depending on the mass chosen and initial condition of the wire itself) bumps were generated on the wire during the decelerating phase of the tests.
After a careful evaluation these defects are mainly caused by the contact of the wire with edges due to the hook shape and the placement of the wire on the disk. (see image 3.4).

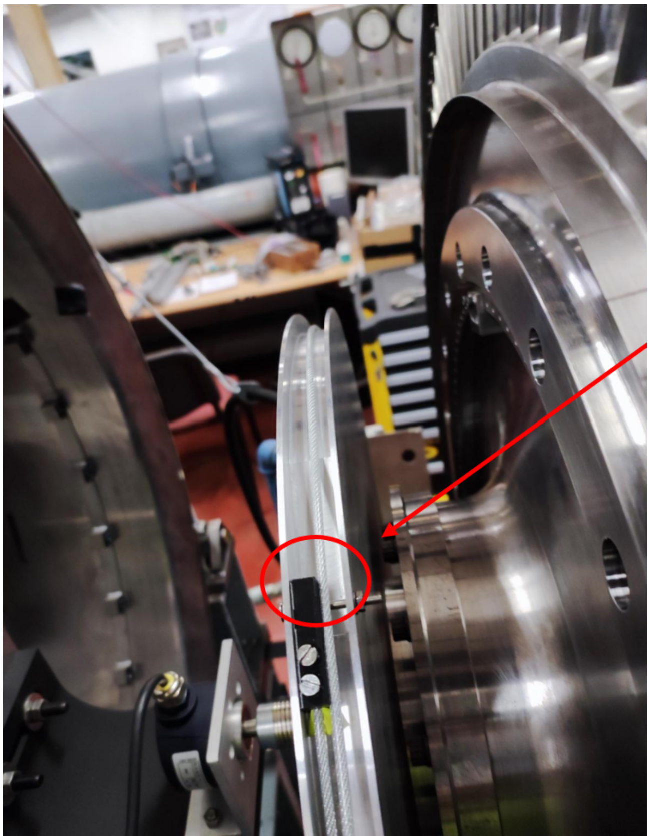

Figure 3.4: Detail of the hook area where bumps are generated; another generating cause of these bumps is the wire rotating itself around the disk in non-linear shapes, then being under tension the deformations on the wire's structure are generated use after use.

These bumps (especially the ones generated after the setup's use), as shown in image [3.5 (a)] significantly disturbed the deceleration phase by generating a torsional of the portion of

the wire connected from the bucket to the pulley, as well as the portion of the wire between the disk and the pulley (this last event has been observed far less frequently).
As it is clear in image [3.5 (b)] this events have been particularly annoying to deal with during the campaign, the candidate has tried every procedure in order to contain the possible uncertainty arising from the torsion events, especially saving the encoder's integrity every time the wire came out of the disk's guide due to these consequences.

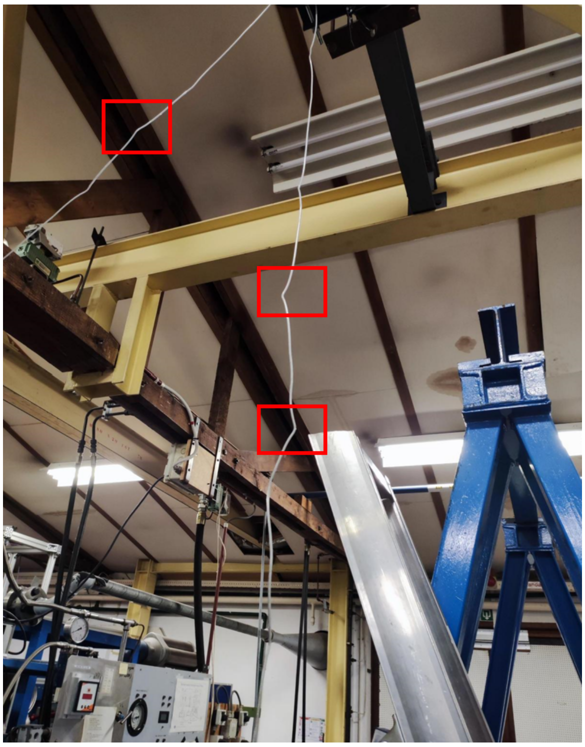

(a) *Visual example of the "bumps", visibly defects of the wire after using them.*

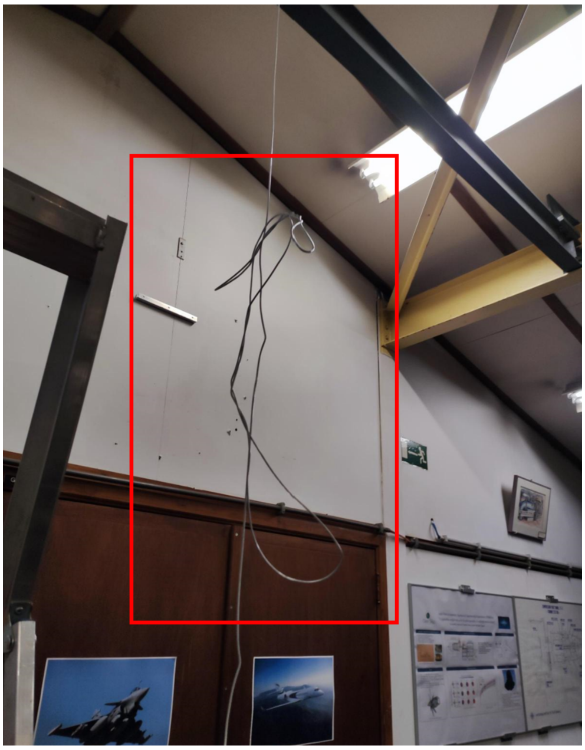

(b) *Example of the "torsion issue", these were the conditions of a wire after finishing a test session: after the bucket hits the floor the tension of the wire ceases to exist and the torsion effect generates this shape.*

Figure 3.5: Even if the wire being not tensioned anymore would not cause theoretically any issue on the data detected by the encoder, the wire torsioning itself and its vibrations could have consequences on the wire allocated on the disk's guide, causing its own mobility out of the guide and interfering with the encoder (risking also to damage the sensor itself).

In summary many tests have been discarded during the laboratory campaign and several "borderline" tests have been discarded in the post processing phase after evaluating the effect of torsion being too significant on the collected data.
The discarded measurements would have had a significant negative impact on the data collected and consequently on the post-processing statistics results, resulting in higher uncertainty compared to the already previously cited studies [8] & [9].

3.3 Post Processing Procedure

The data collected during each test session undergoes a post-processing procedure in MATLAB using a custom code, developed by the candidate.
To illustrate the process logic, both a flow chart (see image [3.6]) and a description of the main processing steps are provided below.

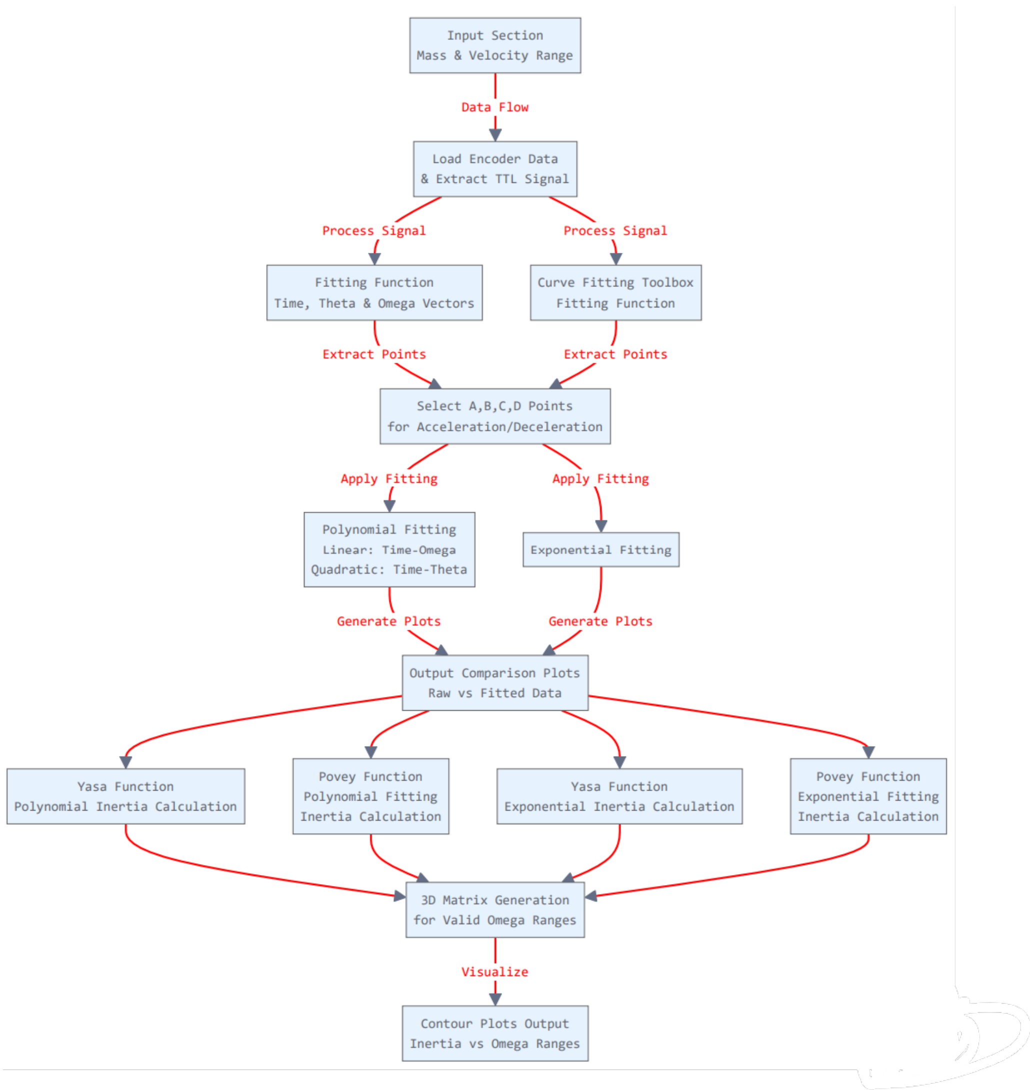

Figure 3.6: Flow chart of the coding routine on Matlab used for the first part of data processing.

a) The coding routine starts in the Main Code with a different input section for every test: the main parameters that can be changed after each test are the mass of the bucket and, due to that, the maximum velocity range detected.
b) The data gathered by the encoder is then loaded to the main script and the TTL signal is extrapolated from the *.m* file.
c) The TTL vector (including number between approximately 0 and 5) is processed and filtered to correct any error in the early stage.
This part of the code simply detects if the signal is over or under the value 2.5V, if it is over the code overwrites the raw value with 5V. Same applies for 0V in the other case.
d) This is the moment where the first function is used: the *"fitting fun"* reads the TTL signal, generates the raw time and theta vector, by using the gradient method calculates

the raw omega vector.
In the input section it is selected a range of angular velocity, for example [1 ; 3] ($\frac{rad}{s}$): the *"fitting fun"* extrapolates from the omega vector the closest points from A,B,C,D and selects them as the extremes of the acceleration and deceleration ranges.

e) After selecting the extremes of the two phases two polynomial fittings are used to generate two vectors both from omega and theta: a linear fitting is applied to the time-omega plots, a quadratic fitting is applied to the time-theta plots.

f) These vectors, as well as the time vector are put into the output plots showing the comparison between the raw signals and the fittings are visually clear; in the figure below [3.8] an example.

g) In parallel a second fitting is performed using the "Curve Fitting Toolbox" function in Matlab: this method provides a realistic fitting of the theta original signal as well as the omega signal by calculating manually the derivative (more details in the appendix [A.3]). Following the same logic of the parabolic and linear fitting cited before new "exponential fitting" vectors are extrapolated for the variables "time" "theta" and "omega".

h) The second function is now called: the *"Function Yasa"*.
It calculates the Inertia of each test by using Yasa's method and equation [A.3];as a secondary output it also calculates the uncertainty for each test and displays the result in a final table as shown in the appendix [A.1.1].
Both the input provided by the parabolic / linear fitting and the exponential fitting are used to obtain results generating two values of "yasa's method" inertia.

i) The third function called is the *"Function Povey"*, a non linear system solving function generating a similar but more accurate value of Inertia compared to the Yasa result, see the appendix [A.2] for reference.
As already cited for the Yasa method two values of inertia are obtained after processing the inputs of the two fittings selected.

j) For each test this process is automatized and generates a 3D matrix to obtain results for every valid omega range; for example the output in figure [3.7] shows the value of the inertia (Povey method) for every possible and valid combination of the superior and inferior omega extremes.

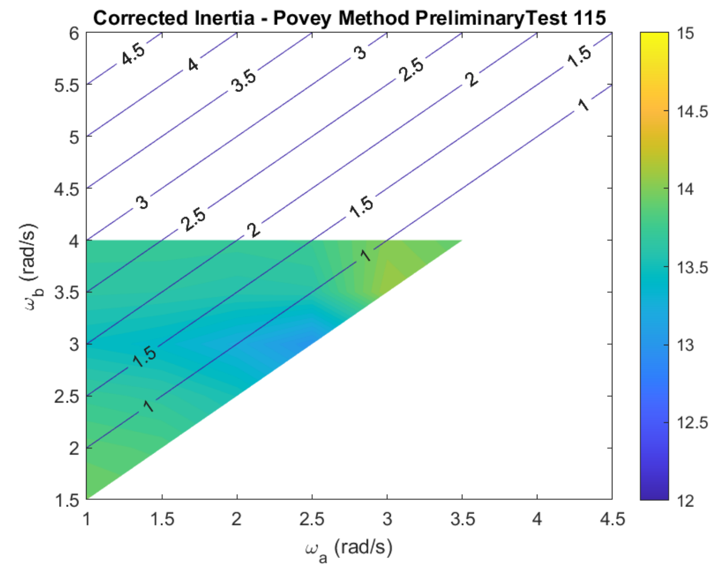

Figure 3.7: Example of the output of the processing of a single test, in this figure the output in the contour plot is the "Corrected Inertia Value" from one single test conducted; as we can see for different combinations of both ω_a and ω_b the value of the inertia tends to be a constant especially for higher combinations of "delta omega" (the increasing-value diagonal iso-lines represent the difference between ω_b and ω_a)

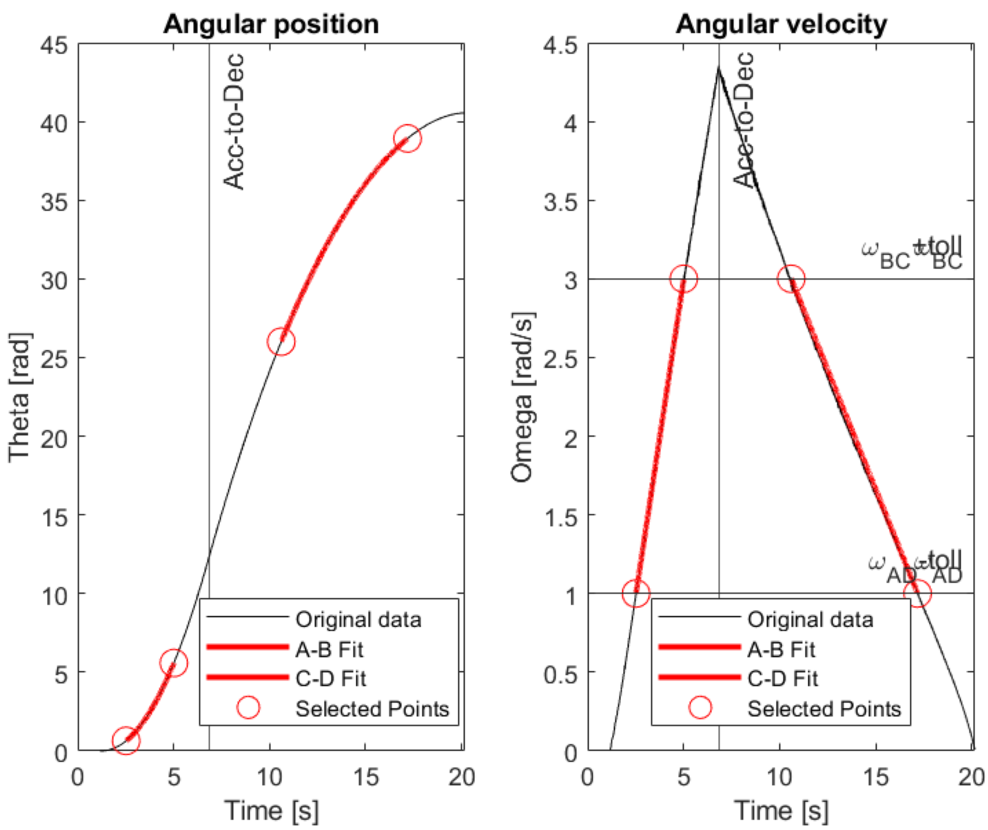

Figure 3.8: Example of the output of the parabolic / linear "fitting function", on the left the time-theta plot as well as the time-omega plot on the right.

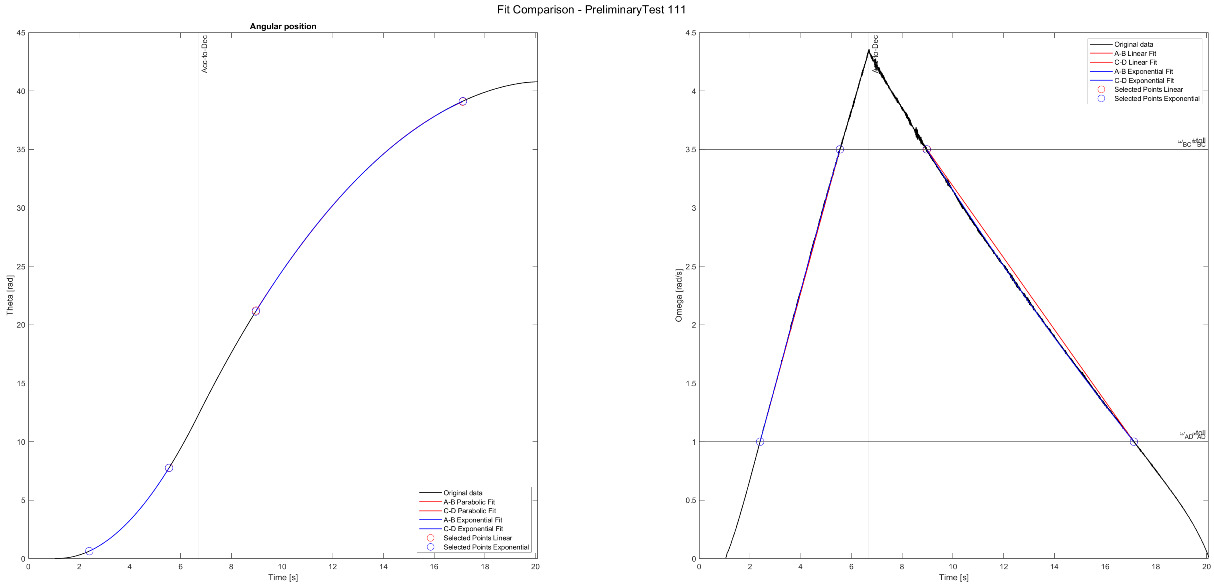

Figure 3.9: Example of the output of the "exponential fitting function" in blue compared to the "parabolic / linear fitting" in red, on the left the time-theta plot as well as the time-omega plot on the right.
It is clear that the exponential fitting closely matches the original signals, generating an accuracy improvement especially looking at the omega deceleration phase.

After saving all the results for each single test of every test session another coding routine (*"Processing Results"*) has been generated to print and plot the statistical final results: the key variables of interest are:

1. Corrected Inertia Yasa
2. Corrected Inertia Povey
3. Corrected Inertia Yasa (Exponential Fitting)
4. Corrected Inertia Povey (Exponential Fitting)

For each of these variables the following statistics have been analyzed and plotted as contour plots (for each combination of ω_b and ω_a in a test session):

a) Mean Value
b) Standard Deviation (σ)
c) 95% Confidence Interval ($\sigma \cdot 1.96$)
d) Repeatibility Percentage ($\frac{\sigma \cdot 1.96}{MeanValue} \cdot 100$) [or uncertainty [%]]

The best results considered are shown in this report in chapter n° [4]: for each test session the combinations of ω_b and ω_a with the lowest repeatibility percentage index and a inertia's mean value close to the CAD reference ($\approx 13.5 kgm^2$) are selected.
To visualize the results the following plots have been generated for every test session:

1. Contour plots of all the statistic values mentioned above [3.3]; these plots are a key output for the project results' analysis because one of the main goals of is to confirm that by increasing the "delta omega" the repeatibility index (or the uncertainty error) on the measured vales tends to be the lowest.
   Linked to this topic, it is expected to see uniform measured values for the region with higher "delta omega", implying the good accuracy of the methodology used to calculate the inertia of the rotor mechanically.
2. Inertia distribution of the highest combination of "delta omega", showing the uniformity (or in some cases lack of it) over the tests; by plotting these results it is possible to

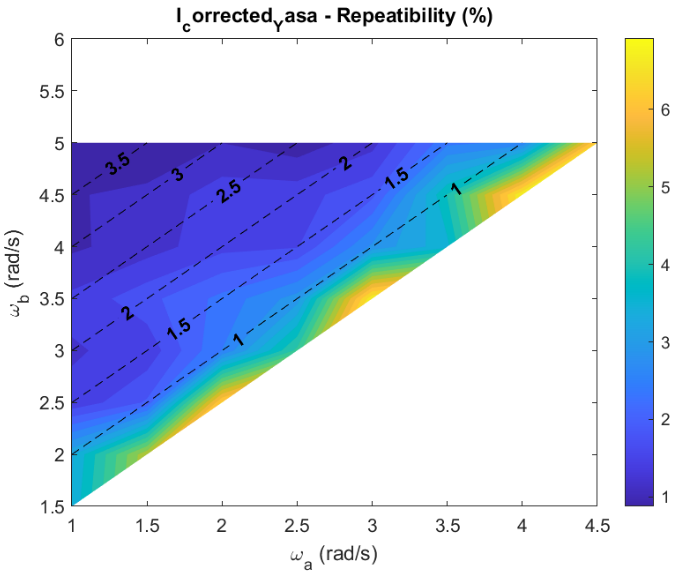

Figure 3.10: Example of the first output of the post-processing of a complete test session, in this figure the output in the contour plot is the "Corrected Inertia's Repeatibilty Index" from the test session n°9; as we can see for different combinations of both ω_a and ω_b the value of the uncertainty tends to decrease towards higher combinations of "delta omega" (the increasing-value diagonal iso-lines represent the difference between ω_b and ω_a) as well being approximately a constant in the same part of the contour plot.

select the best test sessions and compare the results both seeing the distribution over the mean experimental value processed as well as comparing it to the CAD reference value ($13.5kgm^2$).

3. Normal distribution of the inertia values (for all the methods Yasa and Povey) for the same combinations of "delta omega" mentioned above; by plotting these density probability function it can be clear if the inertia values are too affected by random errors.
   If the peaks curves are high it generally indicates that the experimental measurements are more tightly clustered and have lower uncertainty and the data follows a consistent distribution pattern.
   The desired output would be a tall peak near the reference value of the Inertia ($13.5kgm^2$), showing the measurements of each test are mostly uniform and confirming the accuracy of the method chosen.

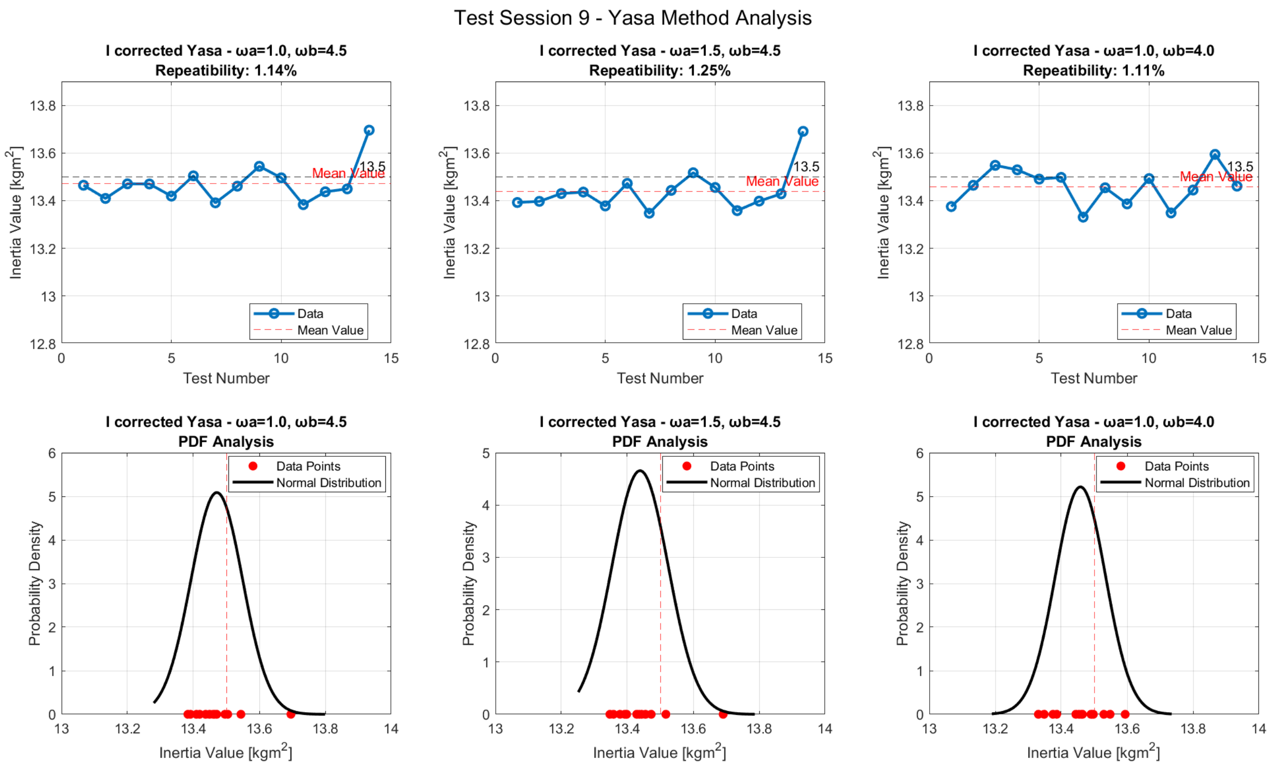

Figure 3.11: Example of the second and third outputs of the post-processing of a complete test session, in this figure the output plot is the "Corrected Inertia's Distribution" from the test session n°9; three omega ranges are selected looking for the lowest repeatibility index measured and the results of each single test is shown in the plot.
In the lower plots it is visualized the normal distribution (classic Bell curve) of the same measurements, ideally for good accuracy this curve should have a high peak and narrow edges. In this example 14 tests have been considered valid out of 20 and the uncertainty is high ($\approx 1.11\%$) for the best omega range combination, resulting in fact in low peaks and wide edges.

Chapter 4

Results

In this chapter the results of the experimental campaign are presented, as mentioned in the previous chapter [3] the analysis of the Inertia values measured has been carried out mainly by obtaining significant plots and valuable statistical data in order to give clear information to the reader.
In the figures below [4.1] & [4.2] for example the contour plot results of the inertia measured and the repeatability index percentage n its value for the test session n°6: this session considers seventeen valid measurements using a mass in the bucket of 7.095 kg.
These tests, as we can also see in the figures [4.3] & [4.4], present a uniform pattern of results over different measurements, resulting in a high peaks of the normal distribution curve, and most importantly in extremely low uncertainty results considering the "repeatiblity percentage"[1].

4.1 Test n°6 & n°8

The following data presented can be considered the best output of the 2024 experimental campaign: first it is presented the detailed separeted results of test sessions n°6, which provided the highest accuracy measured as well as mean inertia value closest to the preliminary target. In the section [4.2] a combined analysis of the previously cited test sessions is presented.

[1]Keep in mind this index is calculated considering a 95% accuracy interval so basically multiplying the standard deviation to the coefficient 1.96, then dividing this number to the mean value of the inertia measurements:

$$Uncertainty[\%](orRepeatibility[\%]) = \frac{1.96std}{I_{mean}} \cdot 100 = \frac{1.96\sqrt{\frac{\sum(I_{measured}-I_{mean})^2}{N-1}}}{I_{mean}} \cdot 100$$

4.1.1 Test n°6 results

For this session a mass of 7.095 [kg] has been used to accelerate the rotor, taking the maximum angular velocity detected for each test around 4.2 rad/s.
A we can see from these contour plots of a single test extracted from the session n°6 [4.1] & [4.2], Yasa's method tends to span results on a larger interval rather then the Povey's method, (this is observed using both the fittings): consequently this translates in lower global repaetibility index.
In the cited contour plots the lowest accuracy measured has been observed for the lowest "delta omega range", which represents the values near the first colored diagonal part of the plots, where the $\Delta\omega$ range is between 0.5 and 1 rad/s.

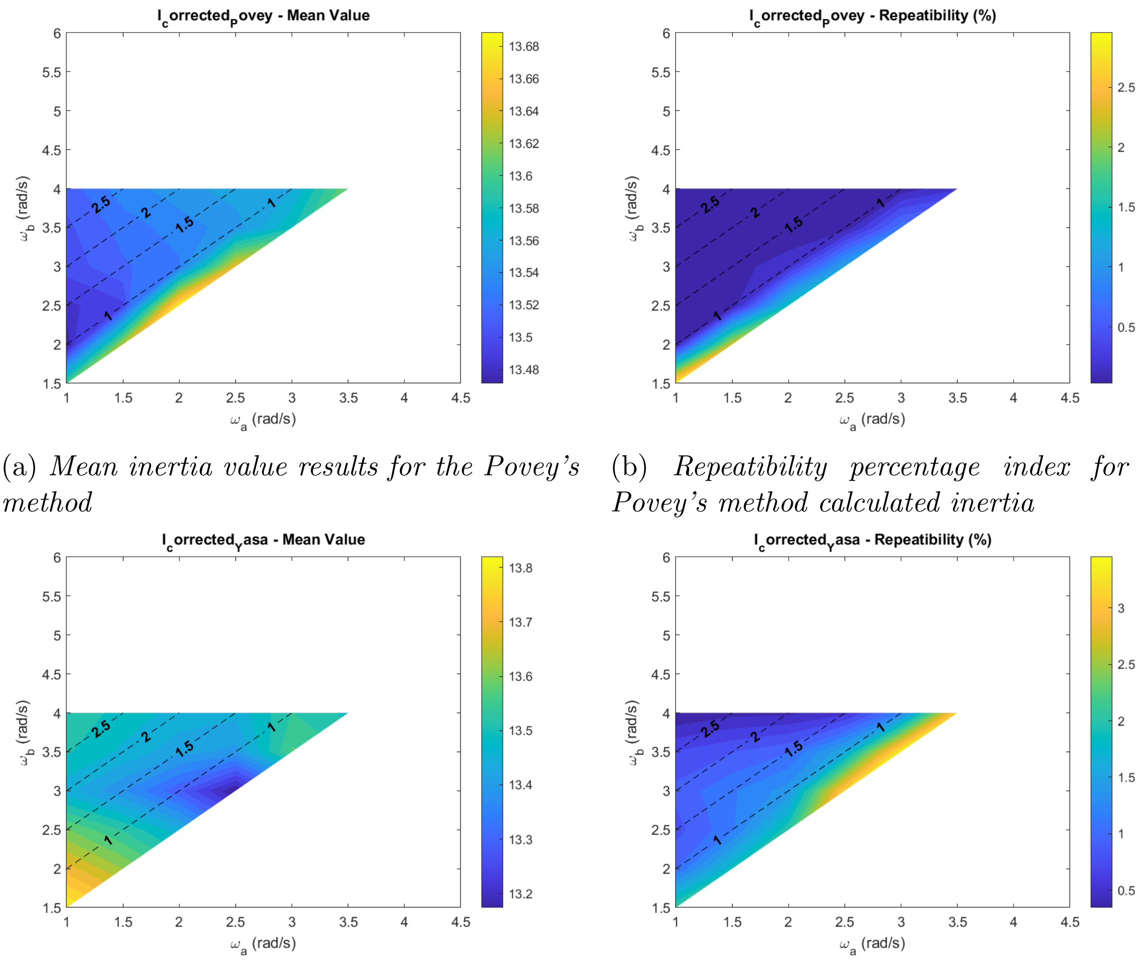

(a) *Mean inertia value results for the Povey's method*

(b) *Repeatibility percentage index for the Povey's method calculated inertia*

(c) *Mean inertia value results for the Povey's method*

(d) *Repeatibility percentage index for the Povey's method calculated inertia*

Figure 4.1: Test 6 "Linear-Quadratic Fitting" Contour Plots Output: on the x-axis the inferior limit ω_a, on the y-axis the superior limit ω_b; the diagonal dotted lines represent the "delta omega" range region.
The value of interest is shown with a scale of colors; to give more context the "repeatibility" contour plots the desired output is obtained by showing a uniform blue area, meaning a low percentage value, on the top left corner of the valid measurements.

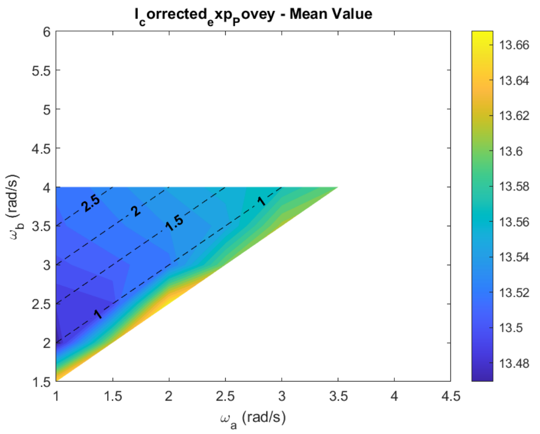

(a) *Mean inertia value results for the Povey's method*

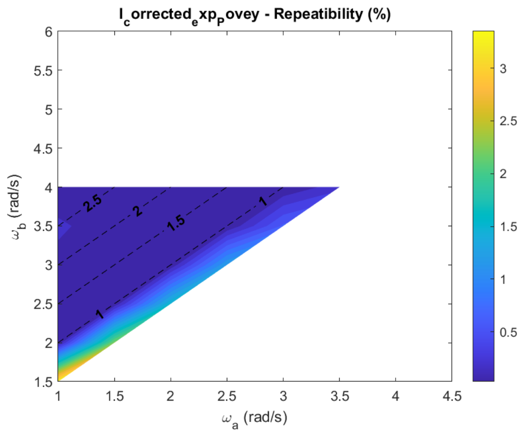

(b) *Repeatibility percentage index for the Povey's method calculated inertia*

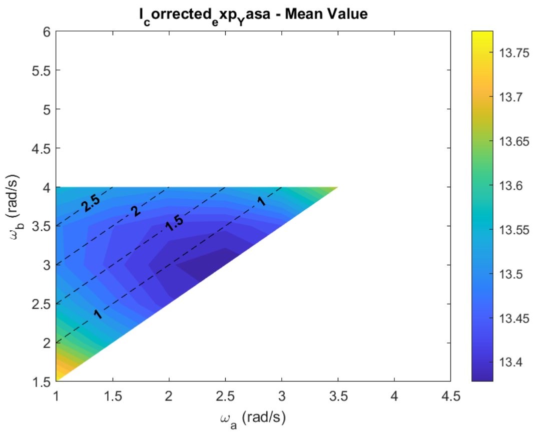

(c) *Mean inertia value results for the Povey's method*

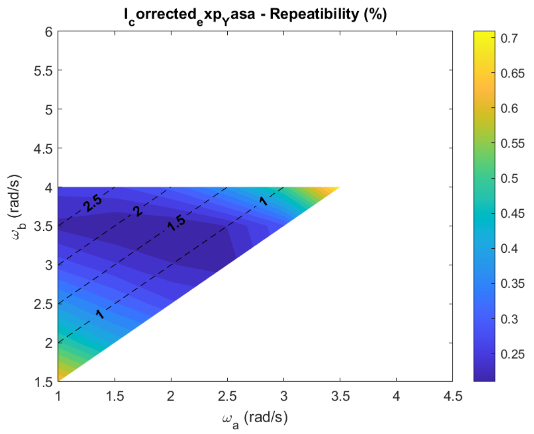

(d) *Repeatibility percentage index for the Povey's method calculated inertia*

Figure 4.2: Test 6 "Exponential Fitting" Contour Plots Output: on the x-axis the inferior limit ω_a, on the y-axis the superior limit ω_b; the diagonal dotted lines represent the "delta omega" range region.

Now considering the highest $\Delta\omega$ range for all the methods (for this test session we are considering data gathered when $\omega_b = 4$ & $\omega_a = 1$), the results for every test have been displayed statistically in the following figures: [4.3] & [4.4].
When the results are uniform the uncertainty is low and it becomes clear seeing the "PDF" (probability density function) plots, where a normal distribution of the data for the selected method is visualized.

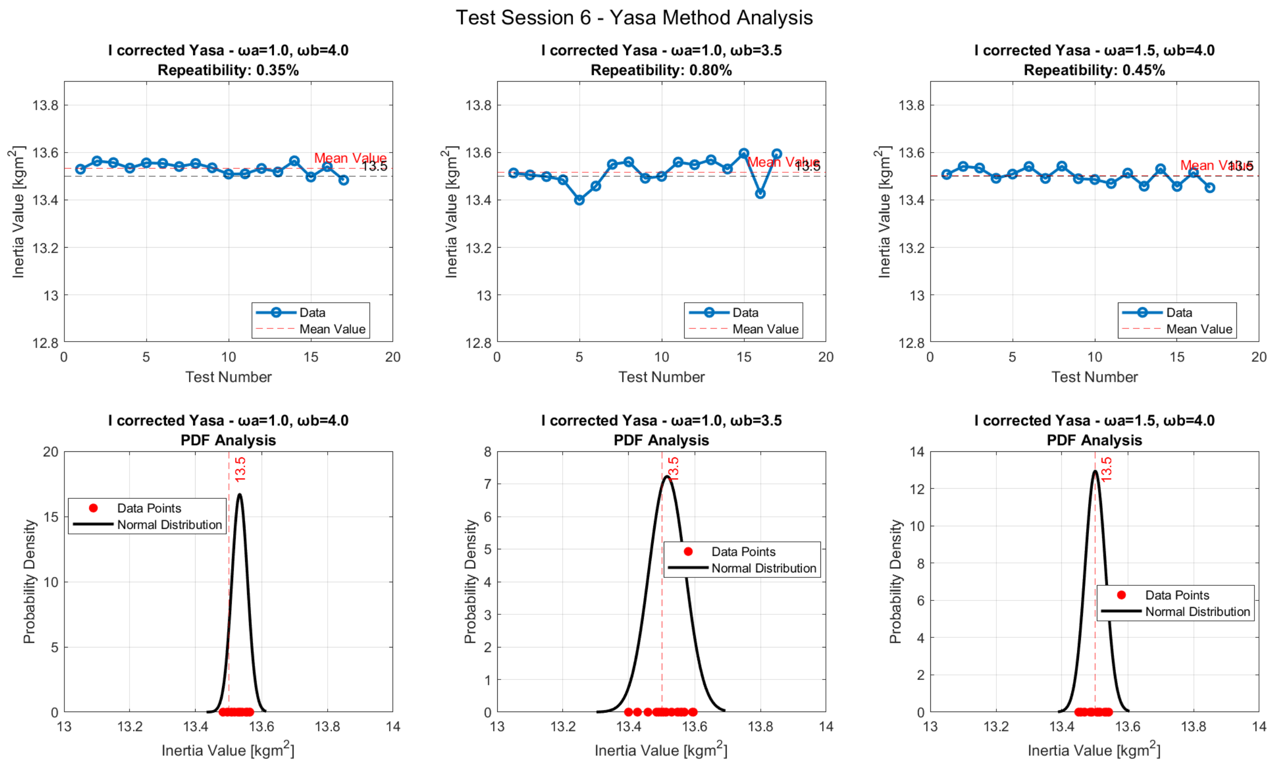

(a) *Yasa method*

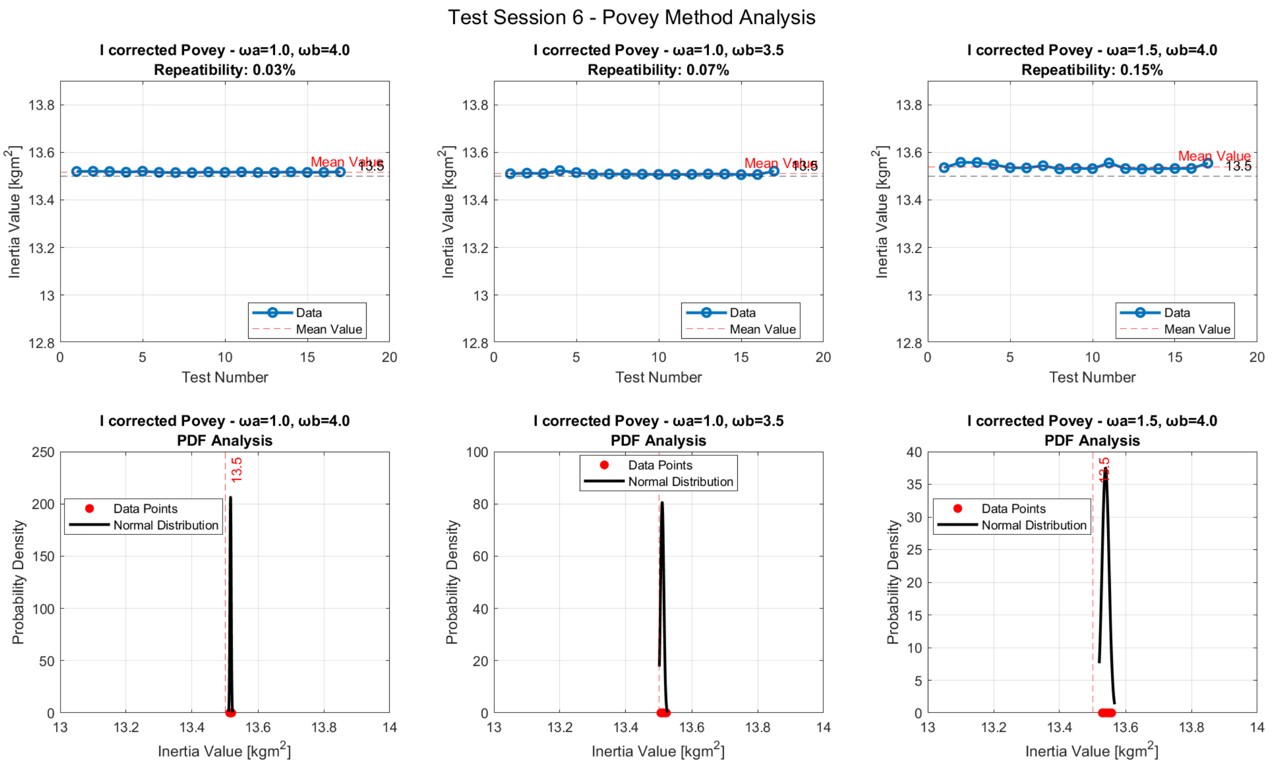

(b) *Povey method*

Figure 4.3: Test 6 inertia distribution across 17 out of 20 valid measurements: comparison between the Yasa and Povey methods using the linear / parabolic fitting data.
Yasa's method gives back a good accuracy result, with 0.35% however Povey method generates an excellent result for every omega range selected, providing results lower or equal to 0.15%

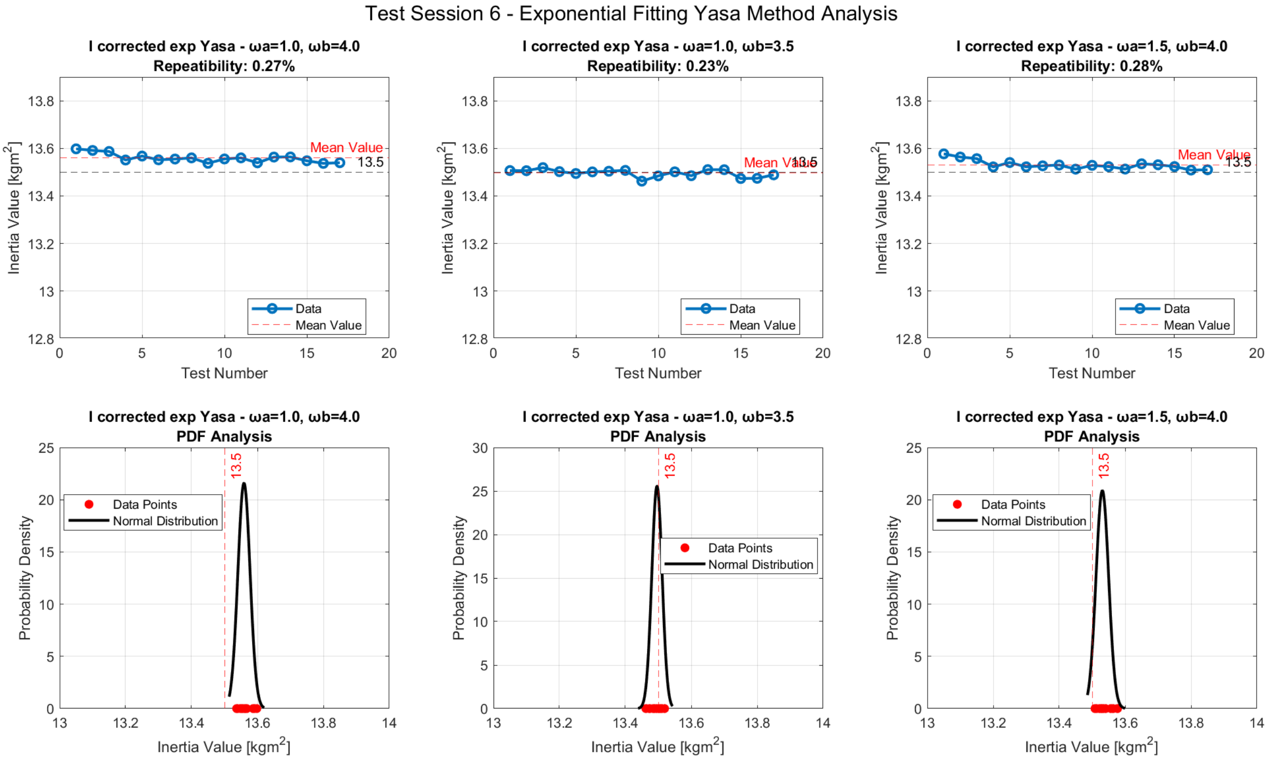

(a) *Exponential fitting yasa method*

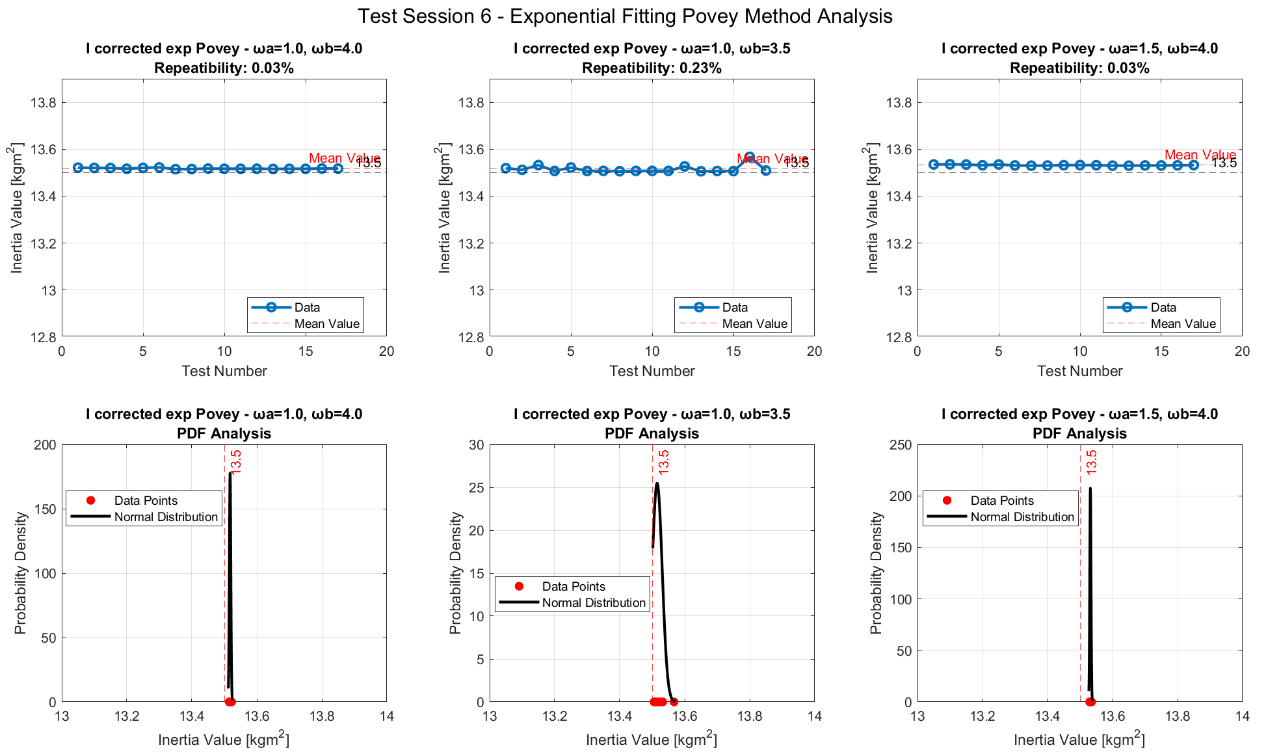

(b) *Exponential fitting Povey method*

Figure 4.4: Test 6 inertia distribution across 17 out of 20 valid measurements: comparison between the Yasa and Povey methods using the exponential fitting data. The exponential fitting data gives back a far more accurate results considering the Yasa method (see image 4.3(a) for reference); Povey method gives back again an excellent result, 0.03% for the highest delta omega range selected and also good results in low uncertainty for the other ranges selected.

4.1.2 Test n°8 results

Other valuable results have been achieved within the test session n°8: using a mass of approximately 6 [kg] the final results are similar to the previous test session analyzed [4.1.1], the uncertainty measured is higher but still a valuable finding.
The same contour plots and statistical visualization of the measurement have been selected and shown in this document in order to display the similarities and the differences the test session n°6.

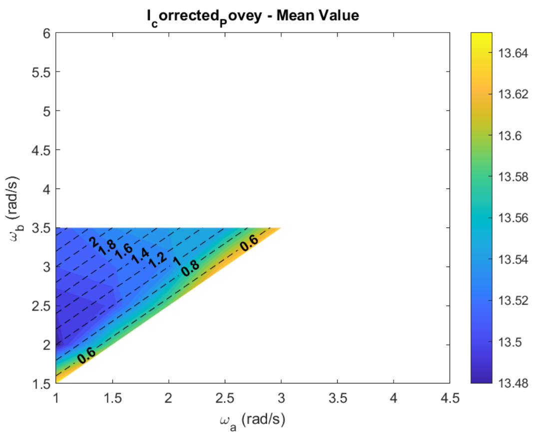

(a) *Mean inertia value results for the Povey's method*

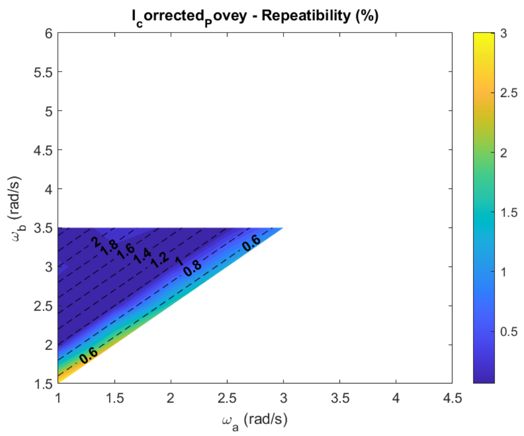

(b) *Repeatibility percentage index for the Povey's method calculated inertia*

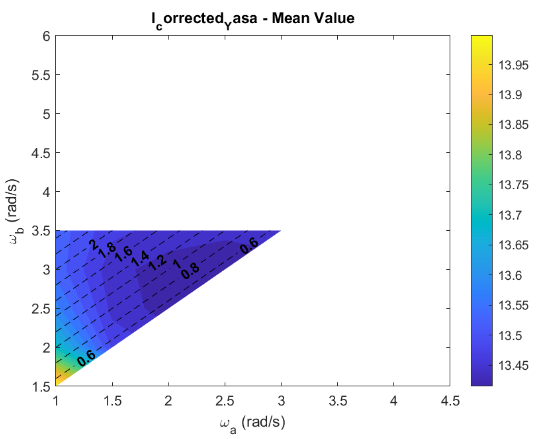

(c) *Mean inertia value results for the Povey's method*

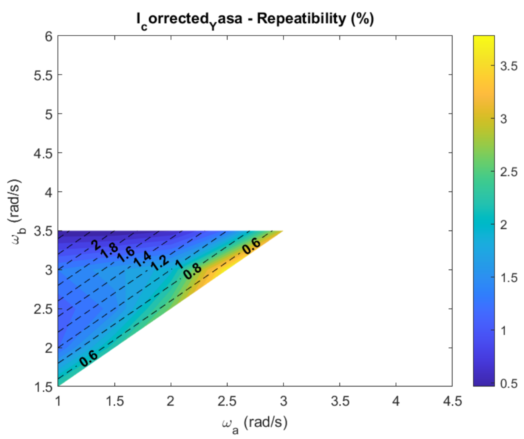

(d) *Repeatibility percentage index for the Povey's method calculated inertia*

Figure 4.5: Test 8 "Linear-Quadratic Fitting" Contour Plots Output: on the x-axis the inferior limit ω_a, on the y-axis the superior limit ω_b; the diagonal dotted lines represent the "delta omega" range region.
Similar to the test n°6 output [4.1] the Povey method gives back a more uniform result regarding the inertia value, and a far lower uncertainty percentage and more uniform result compared to the Yasa's method.

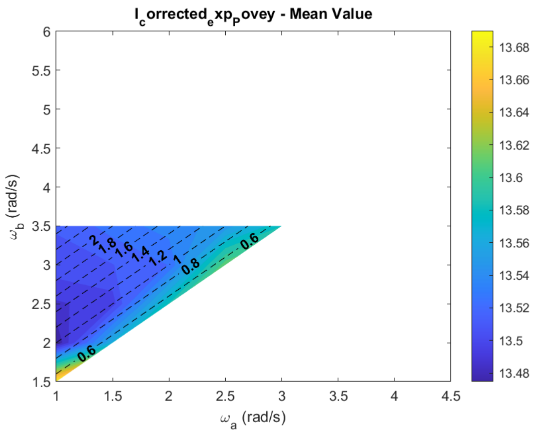

(a) *Mean inertia value results for the Povey's method*

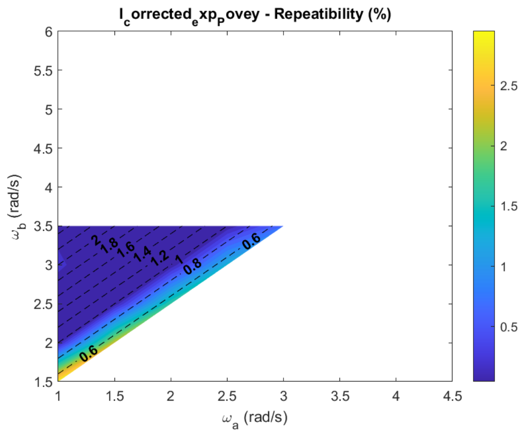

(b) *Repeatibility percentage index for the Povey's method calculated inertia*

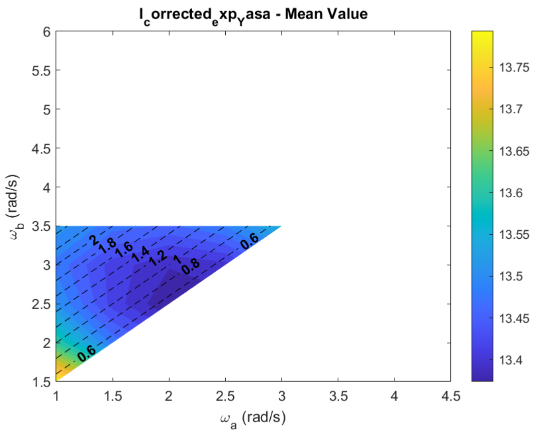

(c) *Mean inertia value results for the Povey's method*

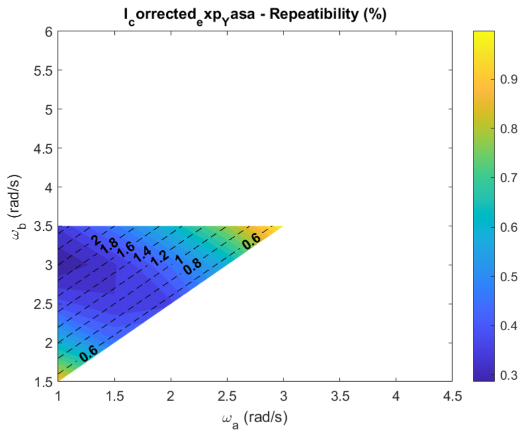

(d) *Repeatibility percentage index for the Povey's method calculated inertia*

Figure 4.6: Test 8 "Exponential Fitting" Contour Plots Output: on the x-axis the inferior limit ω_a, on the y-axis the superior limit ω_b; the diagonal dotted lines represent the "delta omega" range region.

Compared to the Yasa's result shown in the previous figure [4.5 (c) & (d)] this fitting method provides a more uniform and accurate inertia estimation, as it has been observed also on test session n°6 the exponential fitting data has reduced the uncertainty of the measurements.

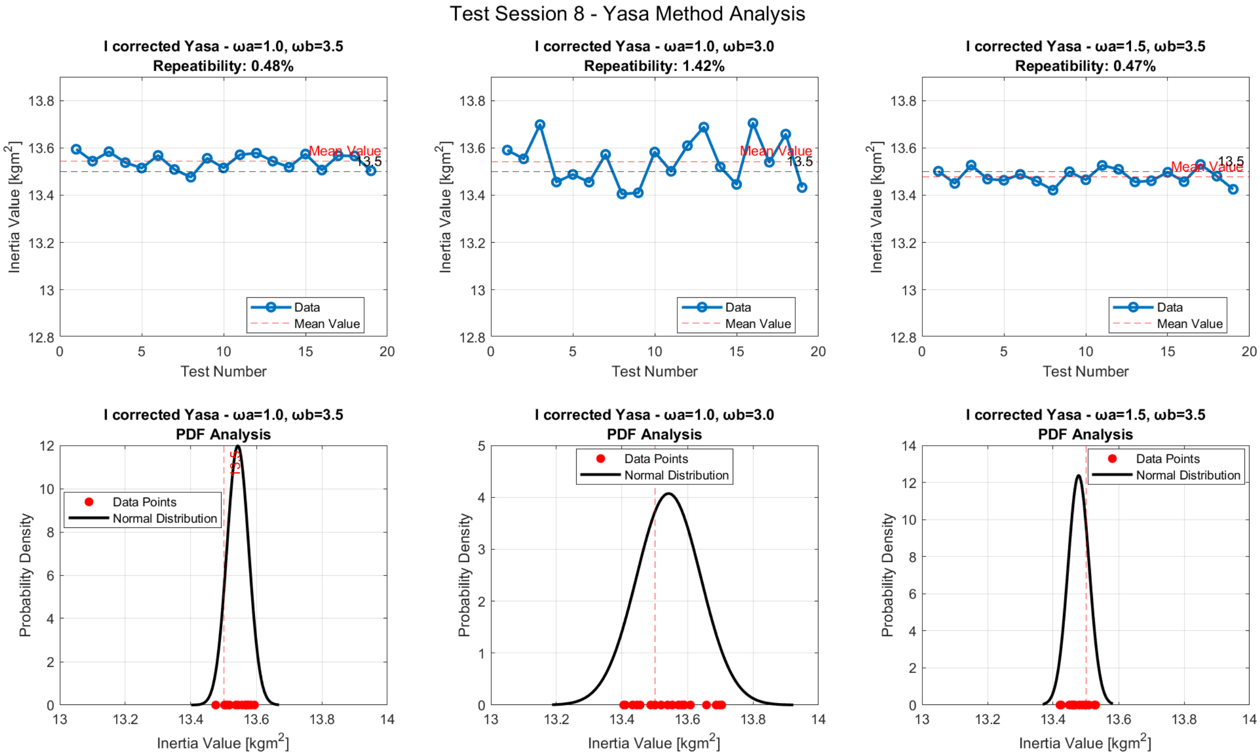

(a) *Yasa method*

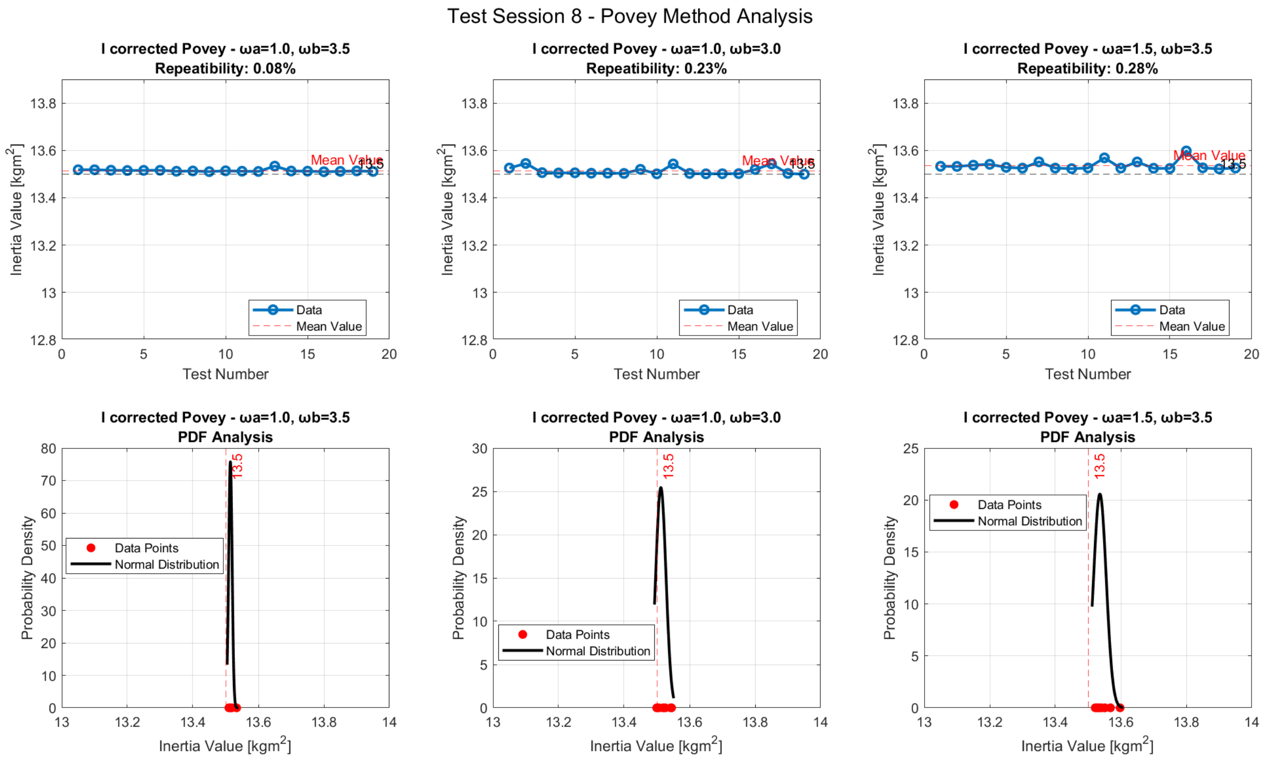

(b) *Povey method*

Figure 4.7: Test 8 inertia distribution across 19 valid measurements: comparison between the Yasa and Povey methods using the linear / parabolic fitting data.

Comparing the distibution of the measurements selecting three of the highest delta omega ranges it is clear that the Yasa method is heavily conditioned by the range chosen, while the Povey method gives back similar results regardless of the omega interval chosen.

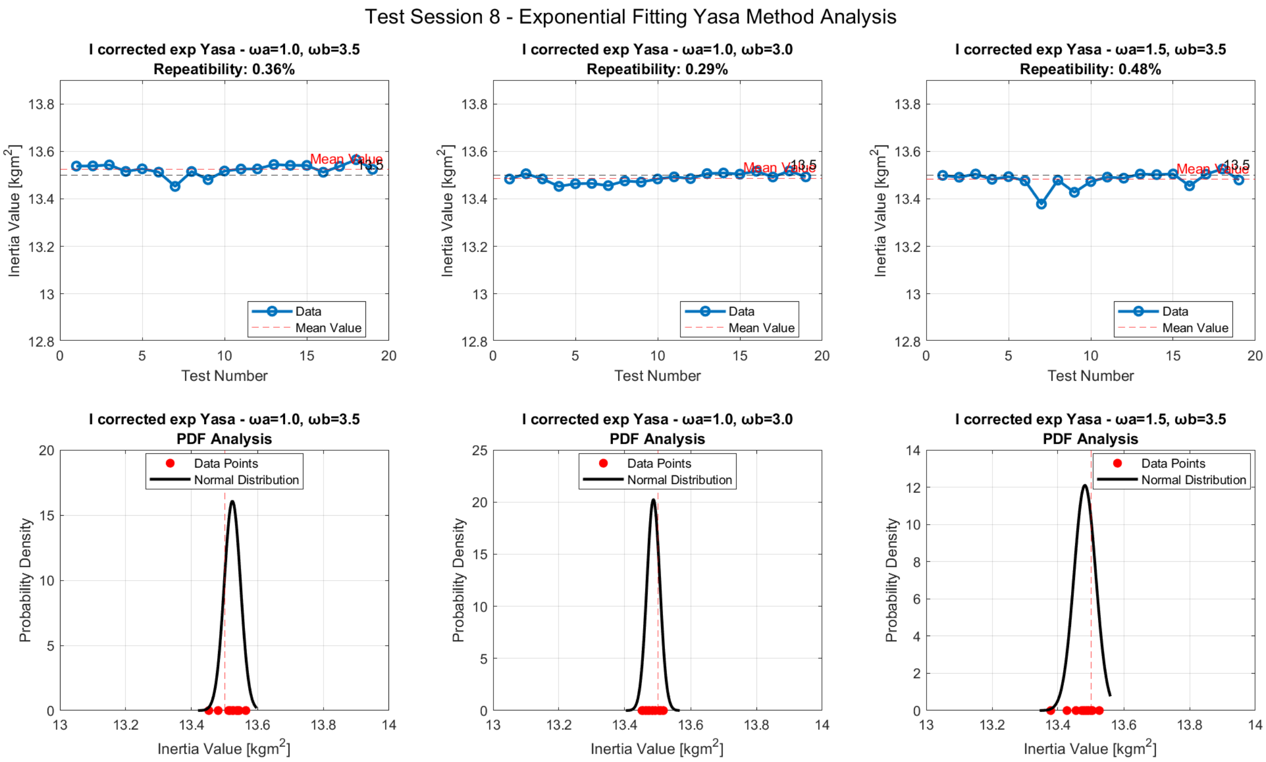

(a) *Exponential fitting yasa method*

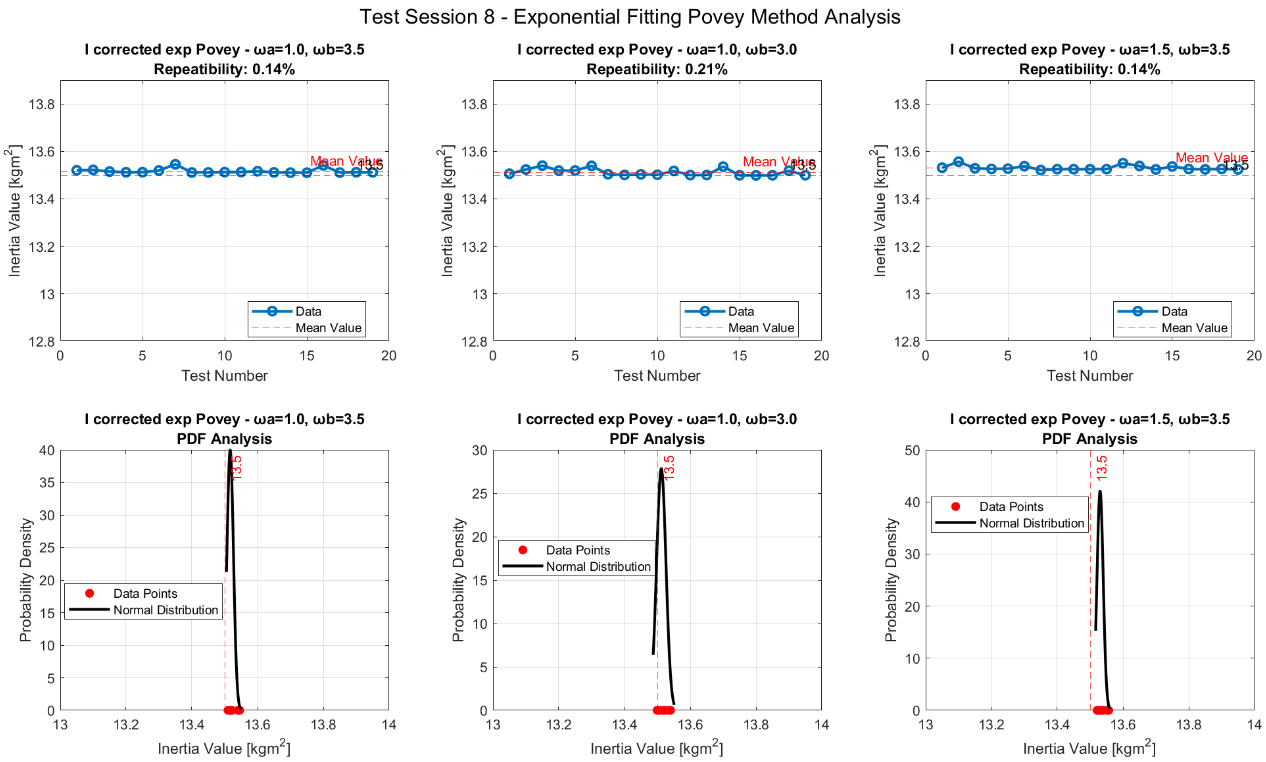

(b) *Exponential fitting Povey method*

Figure 4.8: Test 8 inertia distribution across 19 valid measurements: comparison between the Yasa and Povey methods using the exponential fitting data.

The exponential fitting, as it has been observed in the test session n°6 analysis provides more accurate and uniform inertia measurement results, especially comparing the Yasa method's results between the two fittings (see image (a) and compare it to [4.7 (a)]).

4.2 Combined results tests n°6 & n°8

In the previous papers analyzed [8] & [9] only 11 measurements of one test conducted with a mass of approximately five kilograms were conducted: to give more context Povey method gave back a final result five times more accurate than the Yasa method after processing the exact same test session, see table [4.9] for reference.

RESULTS at 2.3×π		$\bar{x}$	*1.96*σ* [%]
New method	*I*	17.7322	*0.099*
Rotor only	*c1*	3.1583	*2.24*
(11 tests)	*c2*	0.6642	*4.38*
New method	*I*	17.7352	*0.089*
Rotor & 0.001 kg.m^2	*c1*	3.1148	*2.16*
(11 tests)	*c2*	0.6772	*4.22*
New method	*I*	19.7468	*0.076*
Rotor & 2.006 kg.m^2	*c1*	3.1110	*2.84*
(11 tests)	*c2*	0.7801	*5.01*
Constant friction Rotor only	I_{rotor}	17.739	0.500
Constant friction Rotor & 2.006 kg×m^2	I_{rotor}	19.604	0.282

Figure 4.9: The results table shows the final output of the Povey method's post processing (first row) compared to the Yasa's one (last two rows of the table)

In order to amplify the significance of the new 2024 experimental campaign it is shown to the reader the combined analysis of two different test sessions (n°6 & n°8): the results have been filtered two times (choosing the measurements included in the intervals $\pm 2\sigma$ & $\pm 3\sigma$ [2]). This filtering is used only to exclude measurements outside of reasonable intervals and avoid considering out f range data in the statistical analysis.

[2]Reference to the symbol σ used for the standard deviation.

Inertia Value (Method)	2σ filter	
	Highest $\Delta\omega$ Combinations	Statistics
I Yasa	Test 6: ω_a=1.0, ω_b=4.0 Test 8: ω_a=1.0, ω_b=3.5 Points: 34	Mean: 13.5423 kg/m^2 σ: 0.0261 kg/m^2 1.96σ[%]: 0.38%
I Povey	Test 6: ω_a=1.0, ω_b=4.0 Test 8: ω_a=1.0, ω_b=3.5 Points: 35	Mean: 13.5152 kg/m^2 σ: 0.0029 kg/m^2 1.96σ[%]: 0.04%
I Exp Yasa	Test 6: ω_a=1.0, ω_b=4.0 Test 8: ω_a=1.0, ω_b=3.5 Points: 34	Mean: 13.5415 kg/m^2 σ: 0.0224 kg/m^2 1.96σ[%]: 0.32%
I Exp Povey	Test 6: ω_a=1.0, ω_b=4.0 Test 8: ω_a=1.0, ω_b=3.5 Points: 33	Mean: 13.5155 kg/m^2 σ: 0.0035 kg/m^2 1.96σ[%]: 0.05%
Metric	3σ filter	
	Highest $\Delta\omega$ Combinations	Statistics
I Yasa	Test 6: ω_a=1.0, ω_b=4.0 Test 8: ω_a=1.0, ω_b=3.5 Points: 36	Mean: 13.5388 kg/m^2 σ: 0.0292 kg/m^2 1.96σ[%]: 0.42%
I Povey	Test 6: ω_a=1.0, ω_b=4.0 Test 8: ω_a=1.0, ω_b=3.5 Points: 35	Mean: 13.5152 kg/m^2 σ: 0.0029 kg/m^2 1.96σ[%]: 0.04%
I Exp Yasa	Test 6: ω_a=1.0, ω_b=4.0 Test 8: ω_a=1.0, ω_b=3.5 Points: 36	Mean: 13.5406 kg/m^2 σ: 0.0281 kg/m^2 1.96σ[%]: 0.41%
I Exp Povey	Test 6: ω_a=1.0, ω_b=4.0 Test 8: ω_a=1.0, ω_b=3.5 Points: 36	Mean: 13.5172 kg/m^2 σ: 0.0073 kg/m^2 1.96σ[%]: 0.11%

Table 4.1: Highest delta omega range data analysis results 2σ & 3σ filtered: this means that the results outside the interval of 2 or 3 times the standard deviation value have not been considered in the analysis in order to filter out of pocket measurements.
The omega ranges are displayed, as well as the n° of points (measurements completed), inertia's mean value, standard deviation and uncertainty percentage results.
A total of combined 36 valid tests have been considered for this post-processing analysis.

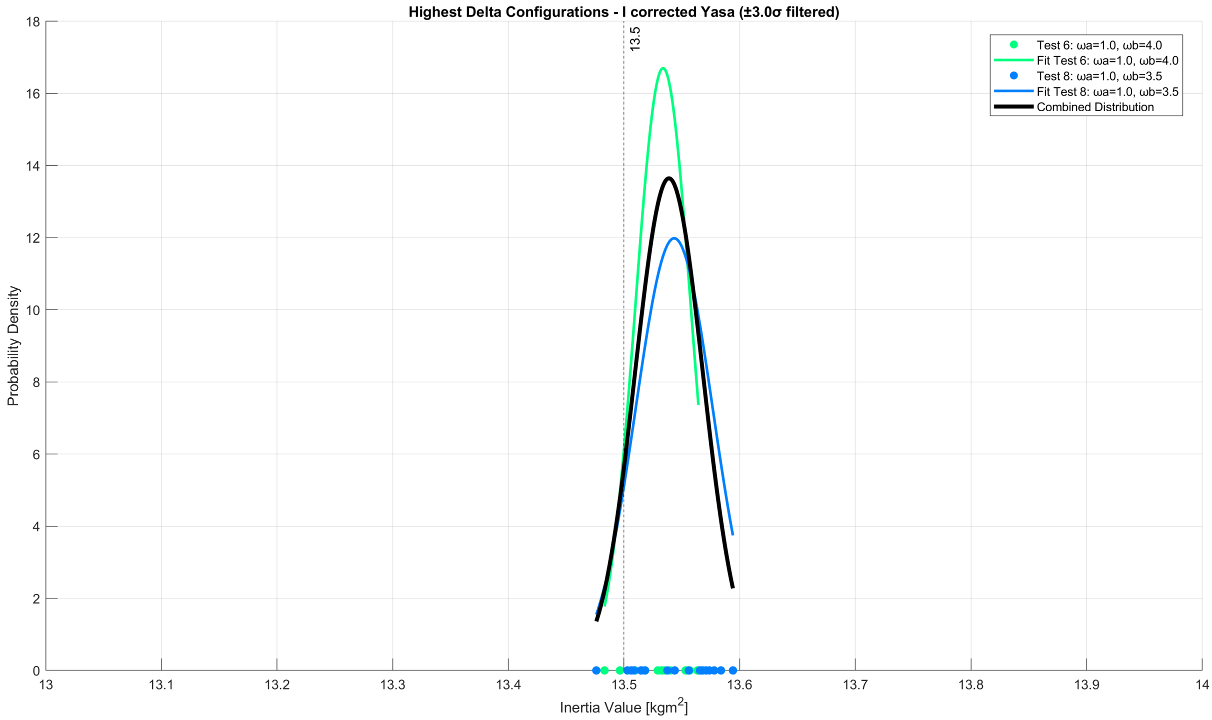

(a) *Yasa method*

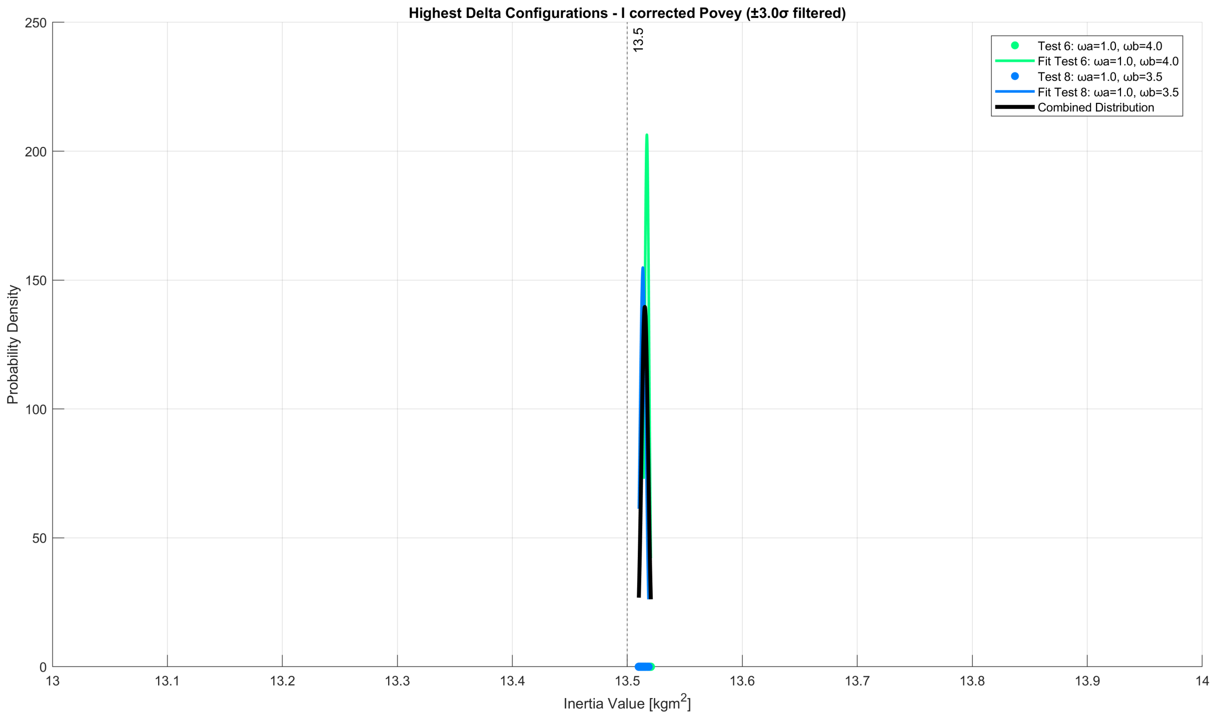

(b) *Povey method*

Figure 4.10: Test 6 8 combined inertia distribution across 36 valid measurements: comparison between the Yasa and Povey methods using the linear / parabolic fitting data.
As we can tell from these plots the accuracy given by Povey's method is ten times higher than the Yasa's method: the peaks of the normal distribution curves for each test and for the combined one (black one) reaches value far higher than 100 for Povey's analysis, while Yasa's method leads to peaks inferior then 20.
The peaks' value is only a visualized and clear meter of comparison of the uncertainty distribution over the two methods; a higher peak means the results are distributed on a small interval, this is clear looking at the distribution of the blue and green points fro the tests sessions n°6 & 8 on the x-axis.

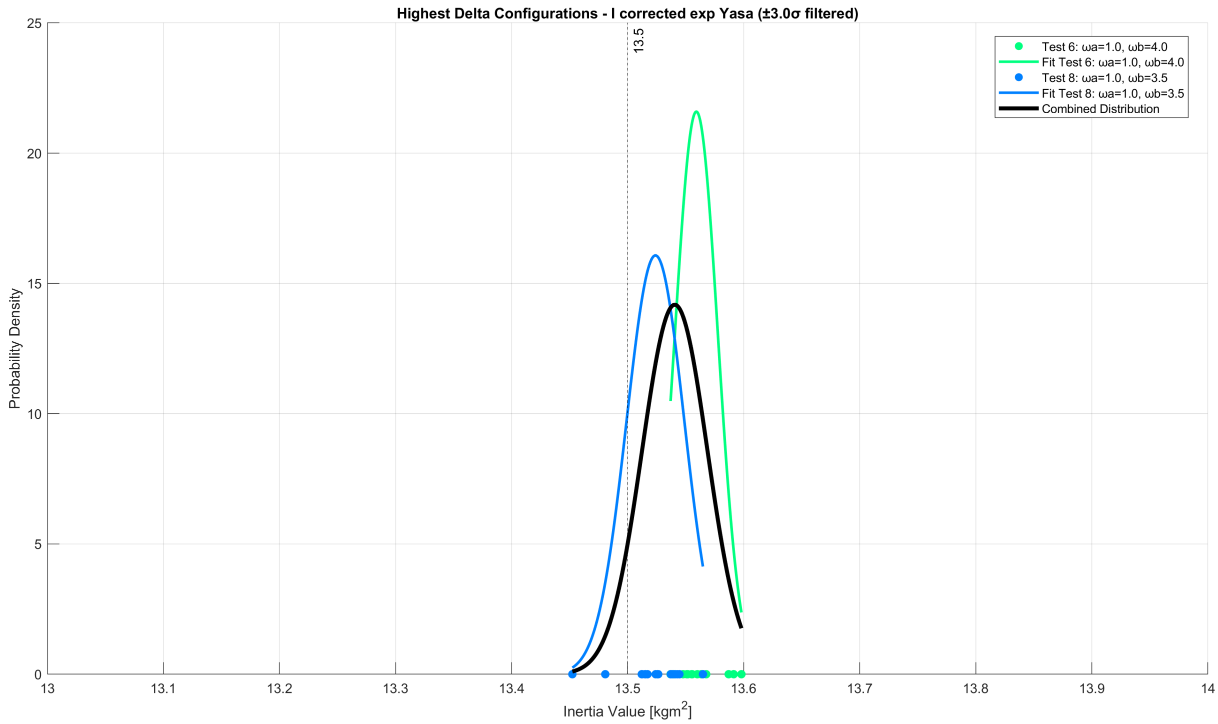

(a) *Exponential fitting Yasa method*

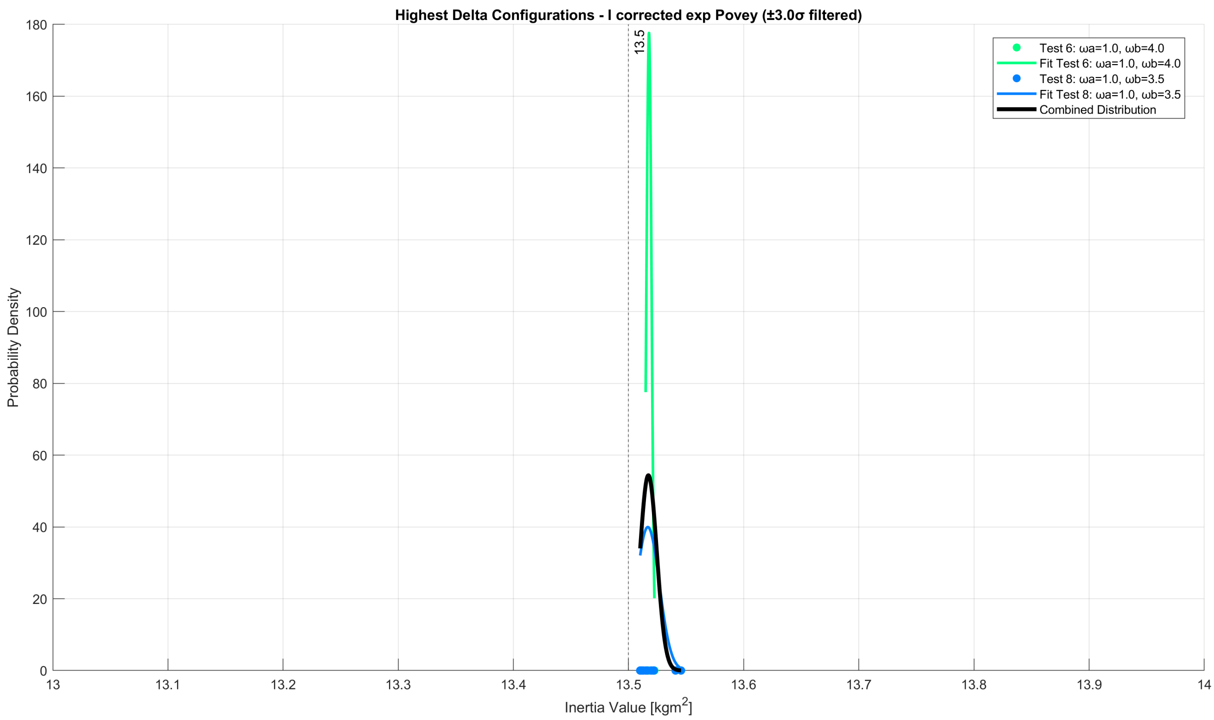

(b) *Exponential fitting Povey method*

Figure 4.11: Test 8 inertia distribution across 36 valid measurements: comparison between the Yasa and Povey methods using the exponential fitting data.
Looking at the these results the "exponential fitting" method gives back an output including a few outliers measurements that increase the uncertainty both for Yasa and for Povey method; the test n°8, being less accurate than test n°6 increases the error as we notice the outlier points at the extremes of the considered intervals are part of the "blue" data.

Chapter 5

Conclusions

After completing all the post processing routines on Matlab in the following table [5.1] the best results of each test session are shown to the reader: the exponential fitting has been applied only to the best two test sessions as the procedure to generate the new fittings by using the "Curve Fitting Toolbox" in Matlab required more time than expected.
Looking at all the test sessions the Yasa's repeatibility results can vary from 0.35% to 1.51%: this is especially due to non-uniform testing conditions and of course by the method's precision. As mentioned previously the most challenging factor in order to achieve uniform testing conditions has been the torsion of the wire, unfortunate event that has frequently been observed during the deceleration phase of many measurements.
A considerable amount of measurements have been discarded during the testing campaign, as well as many others have been filtered during the post processing phase to select the best data to fit in the final analysis.
In the following table [5.1] the highest delta omega range results are presented: this choice has been made because it is the most reliable result regarding the inertia's mean value and for almost every case it represents the highest accuracy value (or repeatibility percentage) obtained between all of the delta omega combinations.

In the table [5.3] the final output of the experimental campaign: comparing these results with the previous studies conducted by Yasa, Paniagua and Povey the following achievements have been observed.
Povey method has been improved by at least by 67%, sligthtly worse results using the exponential fitting to perform the analysis; the Yasa method has been enhanced significantly for both the fitting options.
Using the new fitting especially the Yasa method's accuracy is improved by 22.8%; the new exponential fitting has the potential to give back more accurate results, possibly confirming the Povey's initial hypothesis and validating Da Valle's mathematical solution.

Test Session n°	**Mass**	**Delta Omega Range**	**Repeatability [%]**				**Inertia Mean Value [kgm^2]**			
			Yasa	Povey	Exp Yasa	Exp Povey	Yasa	Povey	Exp Yasa	Exp Povey
1	4.97	[1 ; 3]	1.13	0.16			13.5648	13.4920		
2	7.614	[1 ; 3.5]	0.67	0.27			13.3199	13.5025		
3	4.158	[1 ; 2.5]	0.99	0.30			13.4944	13.5185		
4	5.976	[1 ; 3.5]	0.87	0.05			13.5134	13.5028		
5	6.101	[1 ; 3.5]	0.54	0.68			13.5814	13.5182		
6	7.095	[1 ; 4]	0.35	0.03	0.27	0.03	13.5338	13.5170	13.5592	13.5177
7	5.019	[1 ; 3]	0.84	0.13			13.5015	13.4879		
8	6.002	[1 ; 3.5]	0.48	0.08	0.36	0.14	13.5434	13.5146	13.5240	13.5167
9	9.025	[1 ; 5]	0.88	0.06			13.4149	13.5161		
10	10.662	[1 ; 5]	0.91	0.15			13.3721	13.5121		
11	5.010	[1 ; 3]	0.77	0.13			13.4075	13.4944		
12	7.459	[1 ; 4]	1.06	0.21			13.4855	13.5044		
13	3.970	[1 ; 2.5]	1.32	0.24			12.5775	13.4804		
14	5.980	[1 ; 3.5]	0.98	1.34			13.4547	13.5068		
15	7.552	[1 ; 4.5]	1.28	0.16			13.4558	13.4866		
16	9.086	[1 ; 5]	1.51	0.05			13.3904	13.4912		
17	9.984	[1 ; 5]	0.51	0.12			13.1054	13.4914		

Table 5.1: Highest delta omega range data analysis results for each test session.
Test sessions n°6 & 8 have been highlighted.

Final Results Test session n° 6, $\Delta\omega = [1;4]$, 17 valid measurements Mass: 7.095 [kg]			
Method	Parameter	Value	Uncertainty [%]
Yasa method	Inertia [kgm^2]	13.5338	0.35
Povey method	Inertia [kgm^2]	13.5170	0.03
	c_1	1.9834	2.11
	c_2	1.0116	0.33
Yasa method (Exponential Fitting)	Inertia [kgm^2]	13.5592	0.27
Povey method (Exponential Fitting)	Inertia [kgm^2]	13.5177	0.03
	c_1	1.9786	2.19
	c_2	1.0113	0.25

Table 5.2: Comparison of different methods for inertia measurements conducted on test n°6.

	Uncertainty [%] (previous papers)	**Uncertainty [%] (2024 campaign results)**	**Reduction of uncertainty value [%]**
Yasa method	0.5	0.35	30.8
Povey method	0.099	0.03	71.1
Exp. (Yasa)		0.27	46.58
Exp. (Povey)		0.03	67.1

Table 5.3: Comparison between experimental campaign results; test session n°6 considered as reference.

5.1 Comments and future applications

The alternative exponential fitting has the potential to enhance the accuracy of the measurements, especially remarking the Yasa method (accuracy increased by approximately 22-25% looking at values obtained from tests n°6 & 8) but still needs a further study.
In the table [5.2] the best results obtained from the highest delta omega range selected on test session n°6 are highlighted for the reader: the difference in uncertainty between the fittings (quadratic/linear & exponential) is remarkable if the Yasa method is considered, while the Povey method actually provides a slightly worse result (see table [5.3]) in accuracy but a closer mean value detected.
In conclusion the 2024 campaign has confirmed the accuracy regarding Yasa's methodology and also slightly improved the Povey's method numerical solution; the first evaluations after having implemented the "exponential fitting" approximation are positive; the routine can be still enhanced for a better estimation of the raw data (especially improving the fitting of the data in the beginning and ending of each measurement, when angular velocity are the lowest or the highest).
Improving this part of the post processing code might hypothetically enhance the inertia measurement's repeatibility compared to the standard Yasa's quadratic / linear fitting.
One of the biggest issues cited in this report has been the wires' status, conditions and behavior during the testing campaign (issue mentioned in the section [3.2.1]): despite the wires purchased from the company "Drahtseile24" [12] have matched the initial requirements cited in section [2.4.5], they often presented initial defects (slight bumps) due to the pressure applied in specific points of the wires in the delivering package.
The real main issue reported has been the generation of other similar bumps,often observed while using the wires on the setup: these new defects led to the torsion problem during in the deceleration phases of each test and it is the main reason many measurements have been discarded and repeated over time.
To avoid the generation of these bumps, if the 2024 setup will be used again, the author suggests to modify the "Hook" component a so that it unnecessary edges could be avoided: the hook-disk assembly worked decently in the 2024, however for a potential enhanced setup, avoiding the edges by generating a new geometry of the hook and perhaps putting the hook itself in the free space manufactured on the disk's surface could be beneficial[1].

[1] For example putting a new hook in the space already present below the disk's external guide (look at image [2.11] to visualize the context) could avoid putting pressure on the wire accomodating itself on the hook's edges and also on the screw used for the connection with the disk, which both are causes of the "bumps" generation and so of the avoidable wire's torsion defect.

Appendices

Appendix A

A.1 Uncertainty Analysis on Yasa Measurements

To generate the output of the experiment using the same methodology proposed by Yasa in the paper [8] it was written a new updated code
Using the Taylor's "Error Analysis theory" [13] a comparable output is obtained to the "Yasa" method: this analysis has been conducted to estimate the uncertainty of single measurements due to the new components and setup chosen.
This method is based on a formula to calculate the uncertainty of any equation with multiple variables.
Given as an a example a simple generic equation in only two variables like:

$$q = \frac{x + 2z}{z^2 + 2zx} \tag{A.1}$$

the uncertainty on the value "q" is given by the sqare root of the sum of product of the partial derivates multiplied by each variable uncertainty (measured or extimated) elevated to the second power:

$$\delta q = \sqrt{(\frac{\mathrm{d}q}{\mathrm{d}x}\delta x)^2 + (\frac{\mathrm{d}q}{\mathrm{d}z}\delta z)^2} \tag{A.2}$$

A.1.1 Yasa's method

In Yasa's paper [8] as already mentioned in the section [1.1] the rotor Inertia's uncertainty was calculated considering the following equation and variables:

$$I_{rotor_{Yasa}} = \frac{mR(2g - (R + I_p \frac{R}{mr^2})(\frac{\omega_b^2 - \omega_a^2}{\theta_b - \theta_a})}{(\frac{\omega_b^2 - \omega_a^2}{\theta_b - \theta_a}) - (\frac{\omega_d^2 - \omega_c^2}{\theta_d - \theta_c})} \tag{A.3}$$

The relative error evaluation was given by this formulation:

$$\frac{\Delta I}{I} = \sqrt{0.97(\frac{\Delta R}{R})^2 + (\frac{\Delta m}{m})^2 + 1.3 \cdot 10^{-6}(\frac{\Delta r}{r})^2 + 0.41(\frac{\Delta a_2}{a_2})^2 + 0.14(\frac{\Delta b_2}{b_2})^2 + 3.1 \cdot 10^{-7}(\frac{\Delta I_p}{I_p})^2} \tag{A.4}$$

The constants before each relative error $(\frac{\Delta x_i}{x_i})^2$ are obtained by the following equation:

$$(\frac{\mathrm{d}I}{\mathrm{d}x}\frac{x_i}{I})^2 \tag{A.5}$$

For a further explanation, for the variable "R" the constant 0.97 is obtained from $(\frac{\mathrm{d}I}{\mathrm{d}R}\frac{R}{I})^2$, so a normalization is done for each term by multiplying the variable and than dividing for the inertia's value obtained from the [A.3].

Uncertainty Analysis Results for the project

Applying the formulations mentioned above the new uncertainty estimate has been conducted using the new setup's input data; in the table [A.1] two versions have been carried out by solving the derivatives slightly differently, however the result is basically the same as it can be observed in the final output shown in table [A.2].
The variables contributing to the single measurement's uncertainty are:

- Mass put into the bucket "m", generating the torque on the rotor during the acceleration phase, this is one of the "heaviest" variable in the uncertainty evaluation.
  The uncertainty given by the mass is due to measuring scale used: its precision [1g] has been selected after evaluating the overall percentage weight on the whole error formulation.
  After a preliminary evaluation of the mass's uncertainty the choice between a precision of [1g] and [0.1g] or higher accuracy options, the uncertainty due to this parameter would not have a positive impact by selecting the highest precision; so the measuring scale "Waagenet GRAM AC" [5], with a precision of [1g] has been selected.
- Radius of the disk used to generate the torque on the rotor "R": this is the second "heaviest" term in the error evaluation[1].
- Inertia of the pulley "I_p", given the small dimentions and the low friction of the bearings type chosen, this is the lowest source for uncertainty on the global formulation (even though its relative uncertainty is the highest).
- Radius of the pulley used "r", again high relative uncertainty but low impact in the global uncertainty analysis.
- Acceleration and deceleration terms a & b (or $omega_{AB}$ & $omega_{CD}$), these terms are linked to the mass as a higher force generates higher accelerations and angular displacements of the rotor.

Term	Rel unc [%]	Sens v1	Contr v1 [%]	Sens v2	Contr v2 [%]	Sens Yasa	Contr Yasa [%]
'm'	0.0100	1.0006	9.9354e-07	1.0028	9.9796e-07	1.0133	1.0190e-06
'R'	0.0899	0.9885	7.9019e-05	0.9891	7.9115e-05	1.0011	8.1047e-05
'I_p'	4.2500	-5.5268e-04	5.5174e-08	-5.5268e-04	5.5174e-08	-5.5973e-04	5.6590e-08
'r'	1	0.0011	1.2218e-08	0.0011	1.2218e-08	0.0011	1.2532e-08
'omega_AB'	0.0123	-0.6154	5.7088e-07	-0.6154	5.7088e-07	-0.6232	5.8553e-07
'omega_CD'	-0.0109	-0.3962	1.8770e-07	-0.3962	1.8770e-07	-0.4012	1.9251e-07

Figure A.1: Example of the uncertainty analysis contributes on test number 89. The first column represents the relative uncertainty calculated on the inputs selected; the columns "Sens", or sensitivity are the "specific weights" of each variable on the uncertainty (see the value of the partial derivative term cited previously as A.5)
A higher "sens" value means that variable has a considerable impact on the whole uncertainty evaluation.
The columns "Contr [%]" are the final product of each single term's "relative uncertainty" multiplied by the "Sensitivity"

[1]Looking at the third or fifth columns of the table A.1 the highest values of the "Sensitivity", so the highest partial derivative contribute to the uncertianty preliminary analysys relies on the first two rows: the terms mass and disk's radius.

Tot rel err Deltal/I v1 [%]	Tot rel err Deltal/I v2 [%]	Tot rel err Yasa [%]	Rel Tot Err V1 [%]	Rel Tot Err V2 [%]
0.0899	0.0900	0.0911	0.0126	0.0120

Figure A.2: Final output of the uncertainty analysis, example on test number 89.
The result of the uncertainty analysis on single measurements (with the new setup), using the formulation [A.4] with updated constant values is slightly lower than the Yasa's paper [8] reference value.
After this preliminary evaluation the experiment has been conducted being sure of the results being comparable to the previous studies; even though the rotor object of the measurements as well as the entire experimental setup would be very different between the cases.

A.2 Povey Method code overview using the function "fsolve" in Matlab

It was not necessary to implement the whole algorithm from zero, to get similar results for the new experimental setup following the Povey's method: the old code used the function "fminsearch" in Matlab to optimize the solution of two non linear equations (1.16 and 1.19) in the three variables $[c_1; c_2; I]$ by reducing the error between the velocity trace obtained from the optimization and the raw measurements.

In this code, it is implemented an optimization process using MATLAB's "fsolve", specifically employing the algorithm "Levemberg-Marquard".
This algorithm is a method used to solve both constrained and unconstrained optimization problems; in this case the only consraint would be having the two friction parameters $c_1 \geq 0$ and $c_2 \geq 0$ to avoid physical inconsistance in the model[2] and a Inertia value in a fair interval chosen after a first Yasa's method evaluation.
To give an overview of the new code implemented by the candidate:

1. Objective Function: definition an objective function that calculates the error based on Povey's non-linear equations and the difference between the rotor's moment of inertia and a given value (I_{Yasa})).
   The equations used are the "ω_b [1.16] and ω_d [1.19] laws"
$$\omega_b = \frac{mgR - c_1}{c_2} - [(\frac{mgR - c_1}{c_2} - \omega_a)e^{\frac{-c_2(t_b - t_a)}{I + mr^2}}] \tag{A.6}$$
$$\omega_d = \frac{-c_1}{c_2} - [(\frac{c_1}{c_2}\omega_c)e^{\frac{-c_2(t_d - t_c)}{I}}] \tag{A.7}$$
2. Optimization Variables: The algorithm optimizes three parameters: $c_1; c_2; I_{rotor}$.
3. By using the function in Matlab "fsolve" the local minimum of the objective function is found after selecting optimized initial points for the three variables [3]
4. As shown in the flow chart A.3 a pre-optimization on variabes $c_1 \& c_2$ is conducted on a quite wide interval near the Yasa's method inertia evaluation, trying different combination of these three variables to find the minimum error after calling the function "fsolve".[4]; using the optimized parameters $c_1 \& c_2$ and an intelligent inertia estimation close to the

[2]Frictional torque value must be positive in the formulation $T_F = c_1 + c_2\omega$
[3]Initial constraints are $c_1 \geq 0 c_2 \geq 0$, as well as a initial value of Inertia close to the Yasa evaluation in order to find the correct local minimum value for the inertia variable.
[4]Fsolve algorithm included in the matlab function called: "function Povey v14"

yasa's value (13.8 $[kgm^2]$), the function "fsolve" is called and the final output for the three variables is obtained.

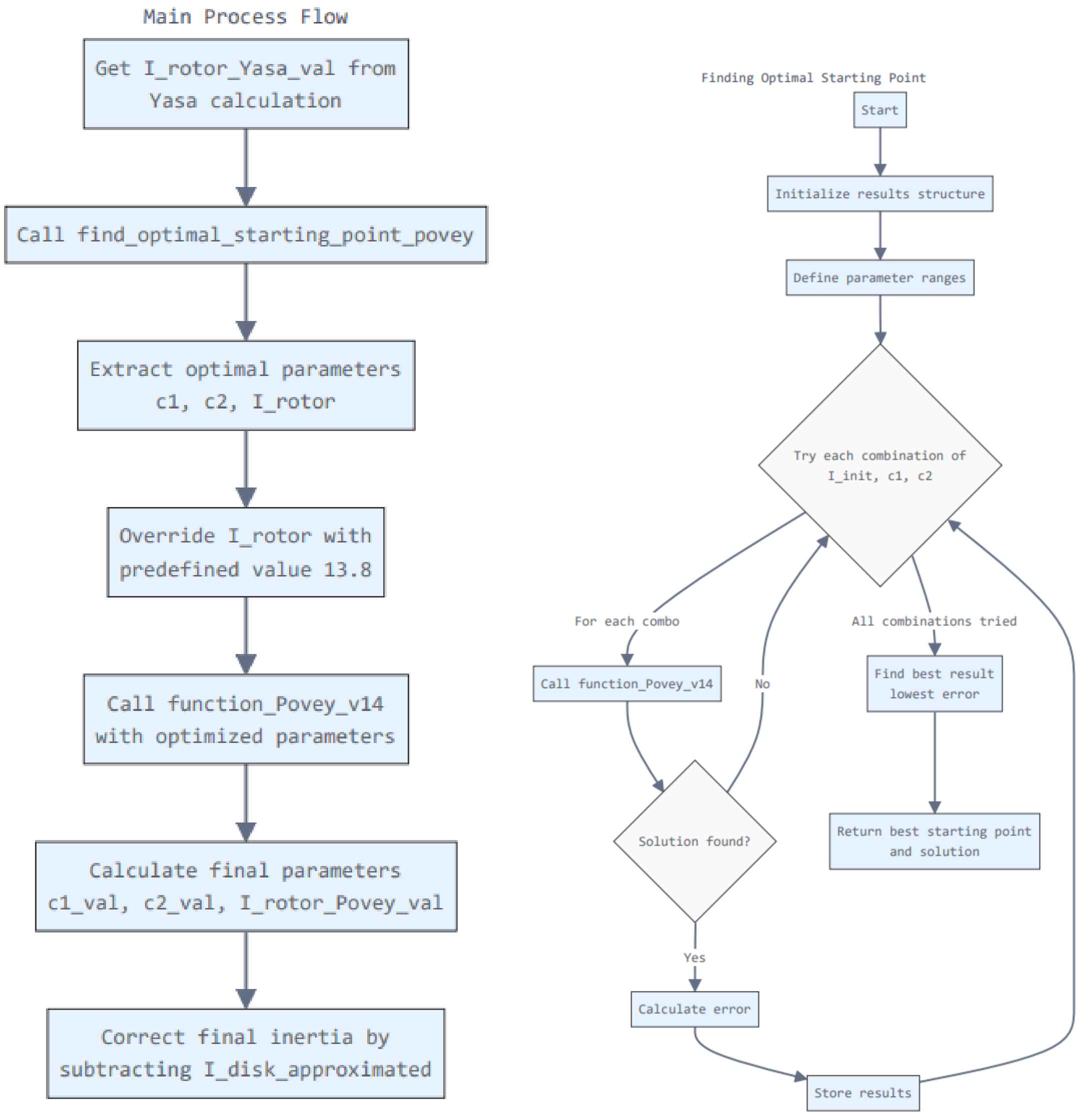

(a) *Povey function logic* (b) *Pre-optimization routined*

Figure A.3: Flow charts of the Povey's coding routine logic (a) and the pre-optimization function detail (b). The correction of the processed inertia value is due to determine the rotor's inertia without the extra components used for the new 2024 experimental campaign, a constant value ($I_{disk_{approximated}} \approx 0.206[kg^2]$, mainly due to the aluminium disk's inertia added to generate the torque) is subtracted to replicate the testing conditions of the rotor during the previous "SPLEEN" campaign[14].

This approach allows the user to find optimal values for the three required parameters that best satisfy the given equations [1.16] and [1.19] as well as respecting the constraints , potentially leading to a more accurate model of the system studied.

A.3 Exponential Fitting code overview using "Curve Fitting Toolbox" in Matlab

An alternative method to the parabolic/linear fitting cited and used in the study [8] has been proposed to the candidate by his supervisor PhD Candidate Lorenzo Da Valle: assuming the frictional torque as an exponential function of the angular velocity, the study conducted by Povey and Paniagua in 2012 [9] proposed this solution as a possible route to improve this experiment's data analysis.

$$\left(I_R + \left(\frac{R_R}{R_P}\right)^2 I_P + mR_R^2\right)\ddot{\alpha} = -R_R mg + \underline{\frac{R_R}{R_P}M_{F,P} + M_{F,R}} \tag{A.8}$$

In fact looking at the inertia equation formulation above [5], the friction moment term (underlined on the right side of the equation, to which we can also refer to as T_F) can be expressed as:

1. A constant value (Yasa hypothesis).
2. A function of rotation velocity, resulting in a second-order non-homogeneous differential equation (Povey hypothesis).
3. A exponential function of the angular velocity ($T_F = a\omega^b$); this hypothesis has been introduced in the Povey's paper [9] but not completely pursued until this 2024 campaign.

According to the preliminary evaluation, the original data detected by the encoder (both the time vs theta & time vs omega) could be approximated after solving a complex system of differential equations: the goal of this fitting would be obtaining smooth curves[6] that could closely match both acceleration and deceleration phases of the tests (theta and omega vectors over time), potentially enhancing the uncertainty analysis results.

A.3.1 Mathematical model behind the "exponential fitting solution"

The equation [A.8]'s solution can be reduced to a second-order linear differential equation:

$$a_2\ddot{\alpha} + a_1\dot{\alpha} = k \tag{A.9}$$

The general solution for $\alpha(t)$ takes the form:

$$\alpha(t) = u_1 e^{-bt} + u_2 t e^{-bt} + k_1 t + k_2 \tag{A.10}$$

where:

- u_1, u_2 are constants determined by initial conditions
- b is the damping coefficient
- k_1, k_2 are integration constants

This last formulation has lead to the following approximations of theta and omega (derivative of θ solution) over time:

$$\theta(t) = ae^{-bt} + cte^{-bt} + k_1 t + k_2 \tag{A.11}$$

$$\omega(t) = -bae^{-bt} + ce^{-bt} - bcte^{-bt} + k_1 \tag{A.12}$$

A function "exponential fitting" has been generated in Matlab, calling the Curve Fitting

[5] R=rotor; P=Pulley; F=Friction R_x=Rotor or pulley's radius ; M_F, x= Rotor or pulley's friction torque

[6] Obtaining a smooth input vector could hypothetically reduce the uncertainty caused by the "defects" of the raw detected signal like small bumps.

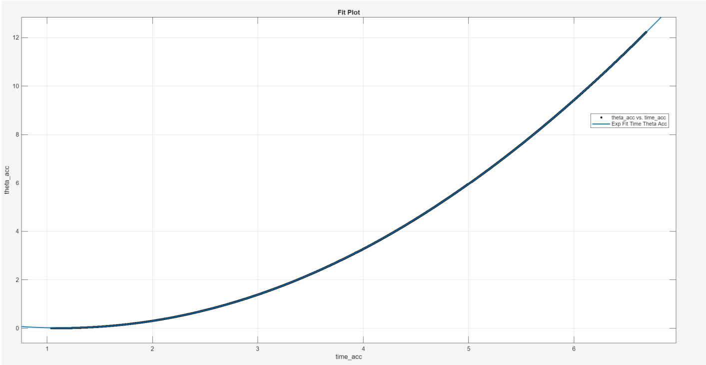

Figure A.4: Detail of the output of the curve fitting toolbox applied to the theta vs time in the acceleration phase, the data in blue represents the "exponential fitting" using the equation [A.11]; the coefficients mentioned above are found by using the method "Non Linear Least Squares" with the goal to find the best combination of values in order to match as closely as possible the original raw data detected.

Toolbox to find the best coefficients

$$a; b; c; k_1; k_2$$

to closely match the original theta signal (both for the acceleration and deceleration phase) using the equation [A.11], then using those coefficients the omega vector has been detected putting those same coefficients in the equation [A.12].

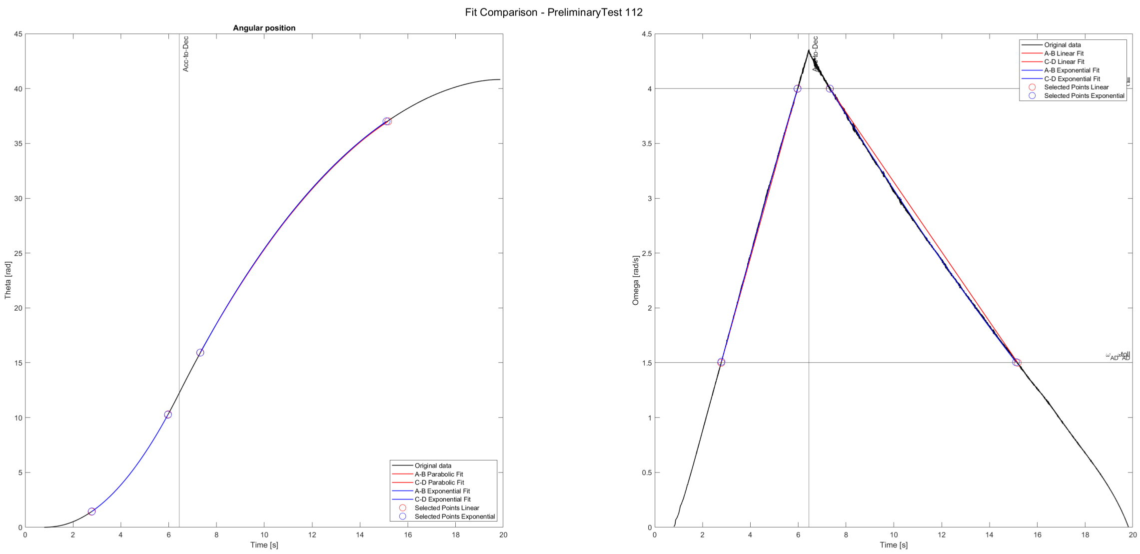

Figure A.5: Final output of the new exponential fitting data (in blue) compared to the original raw data (black) and the parabolic / linear fitting (in red).
Key differences are the quality of the omega deceleration fitting data, that manages to follow the original data more accurately than the

These "exponential fitting" vectors obtained after unsing the Toolbox are then used as an alternative input data for the previously cited functions "Yasa" & "Povey", collecting a final result to be compared with the first fitting method (quadratic / linear).

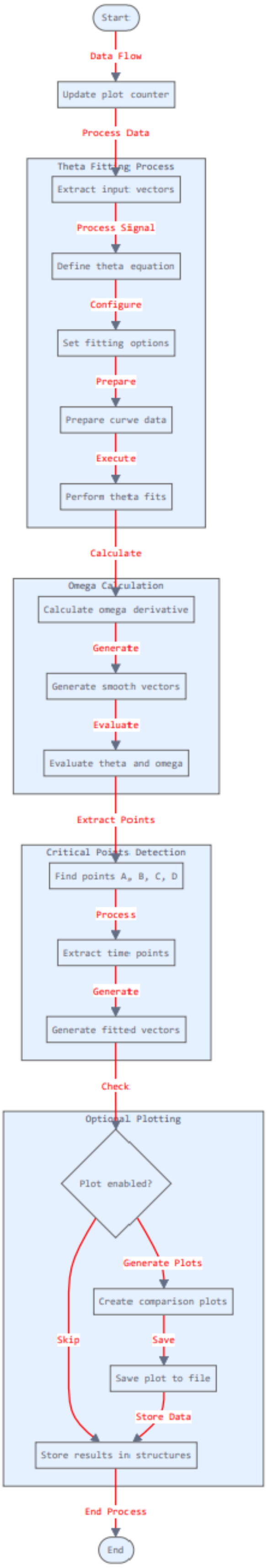

Figure A.6: Curve fitting Toolbox logic overview. For each test the curve fitter is called on the first iteration, first the theta vs time vectors are generated, based on the raw signal detected by the encoder; then the omega vectors are obtained from the direct derivative.
This part of the code generates the whole new "fitting vectors" to be later analyzed in smaller portions by choosing different $\Delta\omega$ ranges (see the figure A.7).

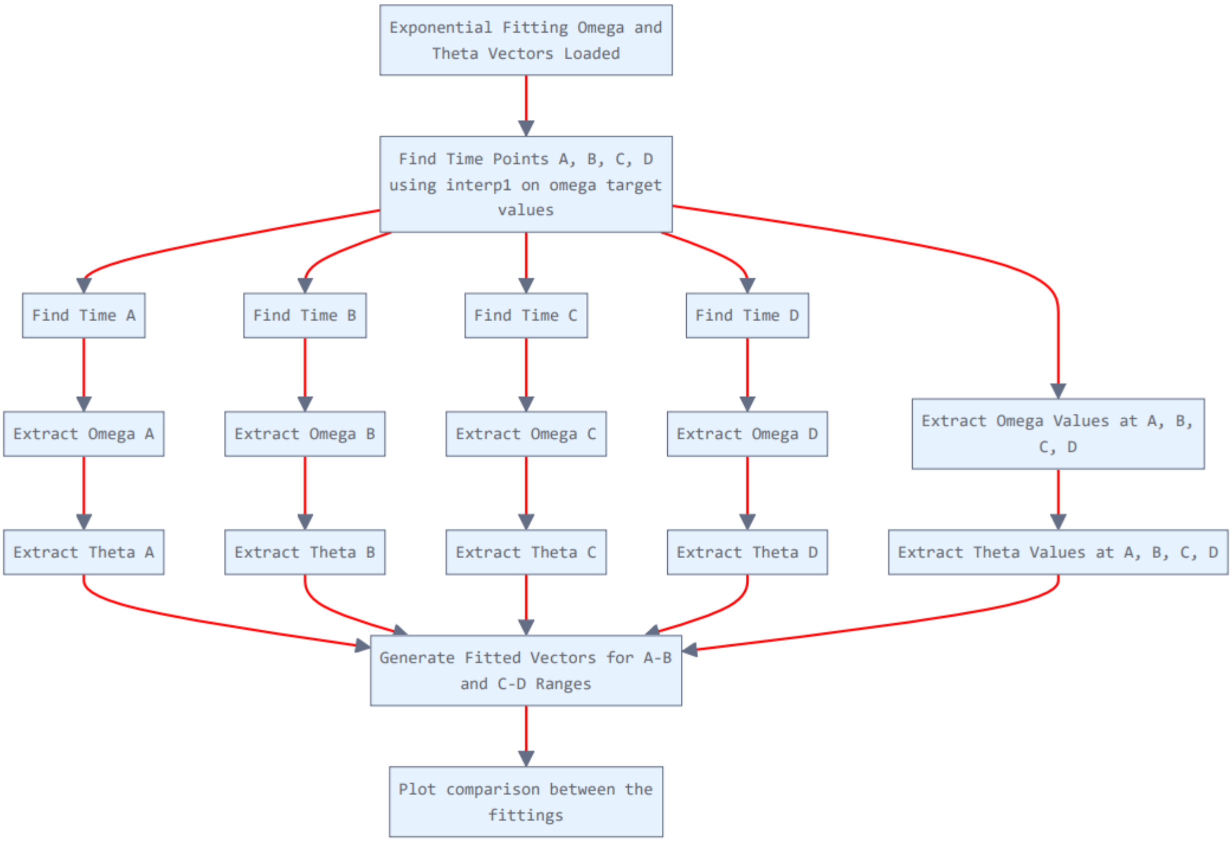

Figure A.7: Logic behind the selection of $\Delta\omega$ ranges in the exponential fitting method: first the input of the desired ω interval is selected, then by using the function "interp1" in Matlab the closest time interval corresponding to the omega inputs are found.
After finding the correct time values for acceleration (A, B) and deceleration (C, D) phases, the omega and theta values are extracted from the "exponential fitting vectors" found using the Curve Fitting Toolbox (resulting from the routine described in A.6)

Bibliography

[1] 3D Jake. *ecoPLA Black Filament*. 2024. URL: https://www.3djake.com/3djake/ecopla-black.

[2] BEI Sensors SAS. *DHM5 Incremental Encoders, DHM5 Range, 100°C*. Technical Datasheet DHM5-_en. Version 171013. Espace Européen de l'Entreprise, 9 rue de Copenhague, F 67013 Strasbourg Cedex, 2013.

[3] RS Components. *M10-M10 Coupliong, 30mm, Stainless Steel*. https://it.rs-online.com/web/p/dadi-di-collegamento/0825281.

[4] R Dénos et al. "Determination of the efficiency of a cooled HP turbine in a blow-down facility". In: *ASME Paper, GT2006-90460* (2006).

[5] *Gram AC, Waagenet Europe*. https://eu.waagenet.de/gram-ac/.

[6] IDEACOD. *Équerre codeur Ø58*. Technical Drawing 9202. Drawing code: 9202, Material: 6060. Eckbolsheim, France: BEI IDEACOD, 2003.

[7] *Mayuela - Metal Bucket - Water Bucket, Garden, Multipurpose - Stainless Steel - 4 Litres : Amazon.Com.Be: Home & Kitchen*. https://www.amazon.com.be/-/en/dp/B01N4S603W?psc=1&ref=ppx_pop_dt_b_product_details.

[8] Guillermo Paniagua and Tolga Yasa. "Accurate turbine inertia measurement". In: *Experimental mechanics* 47 (2007), pp. 693–700.

[9] Thomas Povey and Guillermo Paniagua. "Method to improve precision of rotating inertia and friction measurements in turbomachinery applications". In: *Mechanical systems and signal processing* 30 (2012), pp. 323–329.

[10] *PrusaSlicer — Original Prusa 3D Printers Directly from Josef Prusa*. https://www.prusa3d.com/page/prusaslicer_424/.

[11] Prusa Research. *Original Prusa MK4*. https://www.prusa3d.com/product/original-prusa-mk4-3d-printer/. 2023.

[12] *Stainless Steel Cable PVC Coated per Meter*. https://www.steelropes24.com/stainless-steel-cable-pvc-coated-per-meter.

[13] John Robert Taylor. "An introduction to error analysis: the study of uncertainties in physical measurements, second edition". In: (1980), pp. 43–79.

[14] Antonino Federico Maria Torre et al. "Adaptation of von Karman Institute for Fluid Dynamics' Isentropic Compression Tube Facility for High-Speed Low-Pressure Turbines Testing". In: *Journal of Turbomachinery* 146.041008 (Dec. 2023).